



Peter J. Raboin and
Clifford C. Shang, Center Leaders



The Computational Engineering Center is a vital and growing component of the Engineering Directorate of Lawrence Livermore National Laboratory (LLNL). This new center is the result of combining the Computational Electronics and Electromagnetics Thrust Area with the Computational Mechanics Thrust Area.

The combined entity fuses the computational expertise of two organizations and represents a consolidation of capabilities and activities. The number of engineering analysts at LLNL has grown this past year, as has the demand for sophisticated scientific numerical simulations. The purpose of the Computational Engineering Center is to anticipate and provide for the future analytic needs of the Engineering Directorate at LLNL.

Activities and code development work in LLNL's Accelerated Strategic Computing Initiative (ASCI) began this year with new efforts to parallelize implicit finite element methods. This long range effort will bring the advantages of scaleable computing on massively parallel supercomputers to the entire suite of computational mechanics codes (NIKE, TOPAZ, and DYNA) for important programmatic applications.

Interactions with the Department of Defense (DoD) High-Performance Computing and Modernization Program and the Defense Special Weapons Agency are of special importance as they support our ParaDyn project in its development of new parallel capabilities for DYNA3D. Working with DoD customers has been invaluable in driving this technology in directions mutually beneficial to the Department of Energy.

The research and development activities within the computational electronics and electromagnetics area have yielded a set of simulation and design codes that have contributed to three LLNL "R&D 100" awards in the past two years: theory and design support for high-gradient insulator development, and antenna synthesis for microwave-based bridge deck inspection, were 1997 and 1998 R&D 100 application award winners; work in high-frequency electromagnetics modeling and optical

propagation codes resulted in a 1997 R&D 100 award for the code MELD. This work was continued in the optical-full-wave algorithms being evaluated and developed for use in target design codes.

In this report for FY-98, the computational mechanics articles cover five code development activities that have expanded our ability to handle large problem sizes on parallel computers and problems that deal with greater physical complexity than before. The parallel code work is summarized in a single article covering all of computational mechanics.

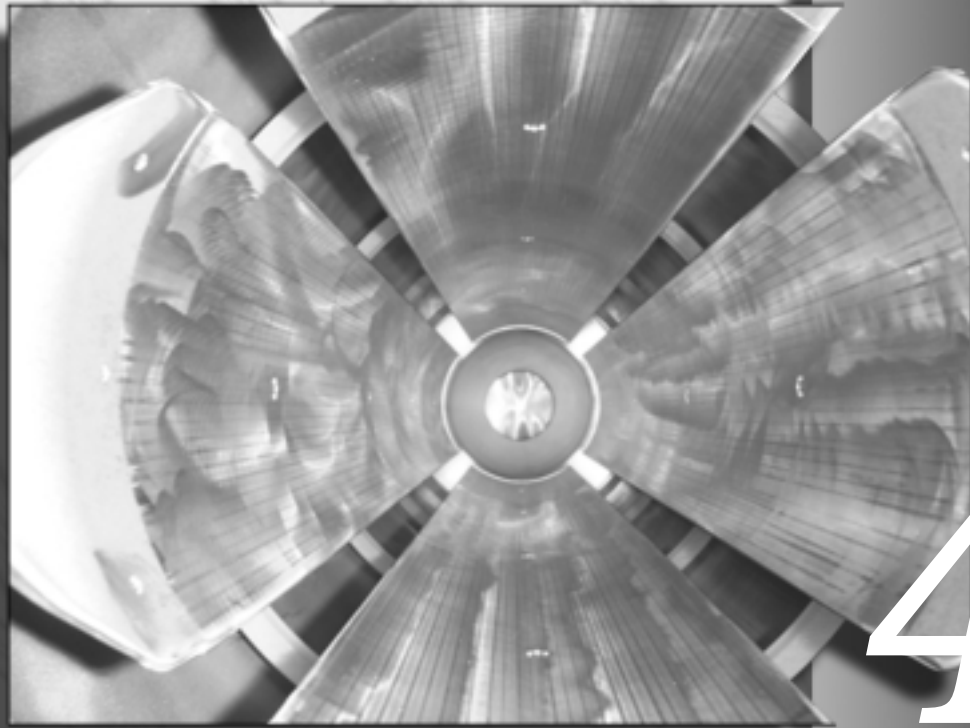
Two articles describe how the explicit DYNA3D code and the implicit codes NIKE3D and TOPAZ3D have been linked and coupled together.

For the code linkage, special element formulations were created to enhance the compatibility of the differing finite-element methods. Another article presents a substantial new cyclic viscoplastic constitutive model added to our codes. The final mechanics article talks about coupling mass diffusion and heat transfer.

The computational electronics and electromagnetics articles describe on-going code development, parallel implementation, design, and validation activities for time-dependent and multi-length scale electromagnetics.

Articles summarizing physics modeling and control of charged-particle beam devices for inertial fusion energy, microwave structure analysis, and accelerator design for LLNL's advanced radiography mission are also in this section. Another article highlights this year's development of new diagnostics which have been developed for novel laser-electron interaction experiments aimed at developing the next generation of light sources. A family of intercepting high-current electron beam diagnostics was also developed. A final article highlights progress in various facets of computational electronics, including electromagnetic and nuclear effects modeling.

Center for Computational Engineering



4

4. Center for Computational Engineering

Overview

Peter J. Raboin and Clifford C. Shang, Center Leaders

Hybrid Ray/Wave Methods for Optical Propagation

Richard P. Ratowsky, Jeffrey S. Kallman, Michael D. Feit, and Bedros B. Afeyan.....4-1

Technologies for Advanced Induction Accelerators

Maurice A. Hernandez.....4-7

TIGER: An Object-Oriented Time-Domain Simulation Code

David J. Steich, Jeffrey S. Kallman, Gerald J. Burke, S Terry Brugger, and Daniel A. White.....4-9

OPUS: An Optically Parallel Ultrasound Sensor

Jeffrey S. Kallman, Dino R. Ciarlo, Elaine Ashby, and Graham H. Thomas4-13

Optical Transition Radiation Diagnosis for Electron Beams

Gregory P. Le Sage and Roger A. Richardson.....4-19

Characterization of Electromagnetic Scattering from Defects in the EUVL Process

Lisa Wang, Scott D. Nelson, Jeffrey E. Mast, and Abbie L. Warrick.....4-23

Nuclear and Electromagnetic Radiation Simulation Tools for Dual-Revalidation of the Stockpile

David J. Mayhall and Michael F. Bland.....4-29

Self-Effects in Expanding Electron Beam Plasmas

Manuel Garcia4-33

Pump-Induced Wavefront Distortion in Prototypical NIF and LMJ Amplifiers

*Mark D. Rotter, Kenneth S. Jancaitis, Christopher D. Marshall, Luis E. Zapata,
Alvin C. Erlandson, Geoffroy LeTouze, and Stephane Seznec4-37*

Parallel Algorithm Development for Computational Mechanics

*Carol G. Hoover, Robert M. Ferencz, Anthony J. De Groot, Robert J. Sherwood,
Edward Zywickz, Yuen L. Lee, and Douglas E. Speck.....4-47*

DYNA3D-TOPAZ3D Coupling and DYNA3D-NIKE3D Linkage

Jerry I. Lin4-55

A Physically Stabilized Eight-Node Hexahedral Element

Michael A. Puso.....4-59

A Cyclic Viscoplastic Constitutive Model

Phani Kumar V. V. Nukala4-65

Electromagnetic Cold-Test Characterization of the Quad-Driven Stripline Kicker

Scott D. Nelson and James E. Dunlap.....4-71

Photonic Doppler Velocimetry

Paul D. Sargis, Nicole E. Molau, and Daren Sweider.....4-77

Modeling Coupled Heat and Mass Diffusion

Arthur B. Shapiro and Philip M. Gresho.....4-81

Analysis and Modeling of a Stripline Beam Kicker and Septum

Brian R. Poole, Lisa Wang, Yu Ju (Judy) Chen, and George J. Caporaso4-85

ybrid Ray/Wave Methods for Optical Propagation

Richard P. Ratowsky and Jeffrey S. Kallman

*Defense Sciences Engineering Division
Electronics Engineering*

Michael D. Feit

*Laser Science and Technology
Laser Programs*

Bedros B. Afeyan

*Polymath Associates
Pleasanton, California*

This aim of this project was to create a computational tool that bridges the gap between the wave and ray optical regimes, important for applications such as laser propagation in plasma and multi-mode photonics. We used phase space methods, where a set of rays distributed in a particular way in position and angle retain many essential features of wave optics. To characterize and enhance our understanding of the method, we developed a GUI-based photonics tool that can analyze light propagation in systems with a variety of axial and transverse refractive index distributions.

Introduction

Until the mid-19th century, natural philosophers argued vigorously over whether light was in reality a wave or a particle. Compelling reasons existed for both points of view: light seemed to travel mostly in straight lines like a particle, but showed diffraction and interference like a wave. In the early 20th century, the same issues surfaced again in the context of the quantum theory, where both light and matter exhibited both wave-like and particle-like behavior, depending on the observational setting.

The ability of light to act like a wave or a particle has practical consequences for the calculation of its propagation. For systems large compared to a wavelength, such as conventional bulk optics, particle-like geometrical optics is usually a good approximation. On the other hand, if the scale of features is on the order of a wavelength, such as at a focal point, solving a wave equation is necessary to capture the physics of diffraction. Often, as in the bulk optics example, both circumstances arise in sub-domains of the same problem.

Many practical situations important to Lawrence Livermore National Laboratory (LLNL) programs

share this dual length-scale property. One important application is laser propagation in fusion plasmas. Traditional modeling uses ray tracing to transport the laser intensity, and this is usually a good approximation. But when plasma gradients are wavelength scale, as may occur in regions of NIF targets, a wave optical treatment is essential.

Another relevant area is multi-mode photonics. A multi-mode optical fiber may be optically large, but calculating the effects of interference—speckle—between the modes is of critical importance.

The purpose of our proposal was to create a computational tool which would move easily between the wave and ray optical regimes. We accomplished this by using phase space methods, where a set of rays distributed in a particular way in position and angle retain many essential features of wave propagation, including diffraction.^{1,2}

By launching the right set of rays, diffraction can be calculated directly from the ray distribution without explicitly solving a wave equation. In this way, a problem domain can easily use both ray and wave optics in the regions where the descriptions are most appropriate. To characterize and enhance our understanding of the method, we developed a GUI-based photonics tool that can analyze light

propagation in systems with a variety of axial and transverse refractive index distributions.

This report gives an overview of our work in FY-98. First, we convey the principles of the phase space method and give some simple examples. Then, we describe the software tool we developed to study the propagation of fields through the Wigner method. This tool allows us to study the important issue of the appropriate sampling of rays in phase space to achieve desired accuracy.

Further examples of light propagation in systems with a variety of axial and transverse refractive index distributions are given.

Finally, we describe some of the limitations of our current scheme and the path we envision for further development and applications.

Progress

Methodology

We usually think of an electric field as a vector quantity that varies in space and time according to Maxwell's electromagnetic field equations. We can also describe the field in terms of the wavenumbers or spatial frequencies which comprise it ("Fourier

representation"). However, it is sometimes most natural to think in terms of a mixed representation, whereby the field is thought of as a set of spatial frequencies, the spectrum of which changes with position. This is analogous to the way music, which is a pressure oscillation changing in time, can be represented by a musical score which shows a set of pitches (frequencies) changing in time. For the electric field, a wavenumber defines a direction in space; the coordinates of the direction are a set of angles. Thus, the field can be represented by a function of position and angle, which defines the ray phase space.

One such function is known as the Wigner distribution.³ Originally invented for quantum mechanics, the Wigner distribution allows us to calculate wave optical properties on the position-angle ray phase space.

Mathematically, the Wigner transform can be thought of as a Fourier transform not of the field, but of its correlation function relating the field at two points in space. An example of a Wigner distribution is shown in **Fig. 1** for a Gaussian field and for a uniformly illuminated aperture. Qualitatively, the reason diffraction is included in the ray description is that, at each point in space, one

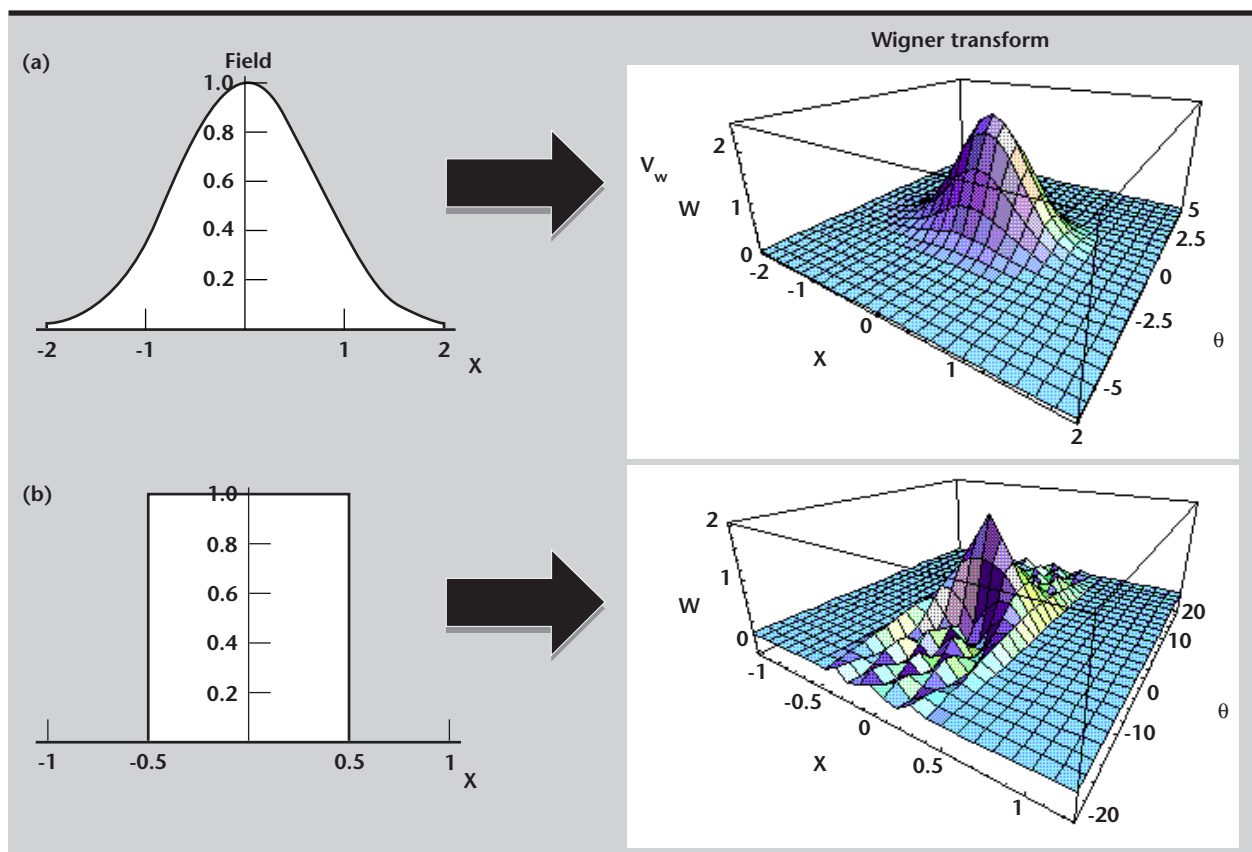


Figure 1. Wigner phase-space distributions for (a) Gaussian and (b) uniformly illuminated apertures.

has a fan of ray angles: this is just a manifestation of the Fourier uncertainty principle. The Wigner distribution is not strictly a phase-space density, however, since it is not always positive.

The Wigner propagation algorithm works as follows. From an initial complex electric field distribution, we calculate the Wigner transform. This distribution is then evolved in space by simply transporting it along rays, that is, assuming conservation along a ray. This will be an excellent approximation if the index is not too rapidly varying on a wavelength scale. If at every position in the ray phase space for the new (evolved) distribution, we integrate over all ray angles, we obtain the intensity distribution ("near field") as a function of spatial position.

Conversely, if at each angle in phase space we integrate over position, we obtain the intensity distribution as a function of ray angle ("far field"). Since in wave optics the near-field and far-field amplitudes are related by Fourier transform, the complex electric field can be reconstructed (up to a constant phase factor) from the ray intensity distributions in position and angle.

As an example of a calculation using the Wigner propagation algorithm, we calculated the diffraction pattern from a double slit (**Fig. 2**). The Wigner function is calculated in the plane of the slits, then propagated along rays to the plane of the screen. The calculated result and the exact solution are overlaid, and agreement is excellent. In fact, for free propagation, the Wigner method is formally exact, and the only errors are due to sampling. This

illustration shows strikingly that diffraction and interference, usually considered outside the domain of ray optics, can be obtained through ray tracing the Wigner distribution.

PHASTER

To study the Wigner method we developed a GUI-based code which allows us to propagate beams in a variety of media in two spatial dimensions. We call the code "PHASTER": Phase Space Techniques for Electromagnetics Research.

PHASTER allows us to set up an arbitrary initial beam consisting of a sum of Gaussians with selected widths and amplitudes. After computing and displaying the Wigner distribution for the beam, it will solve the ray equations for a set of points in the ray phase space which sample the Wigner distribution in a prescribed manner. The rays are traced using an adaptive Runge-Kutta method through a variety of refractive index distributions having both transverse and axial variation.

After propagating the prescribed set of rays to the exit plane, it will display the phase-space distribution at the exit plane, as well as the x-space and angle-space intensities (near field and far field). PHASTER gives useful insight into the dynamics of the rays in phase space and their effect on the wave optical distribution.

Our first example of a PHASTER calculation is shown in **Fig. 3**. A Gaussian beam is shown propagating through three "soft slabs," that is, small regions where the refractive index rises and falls, depicted in

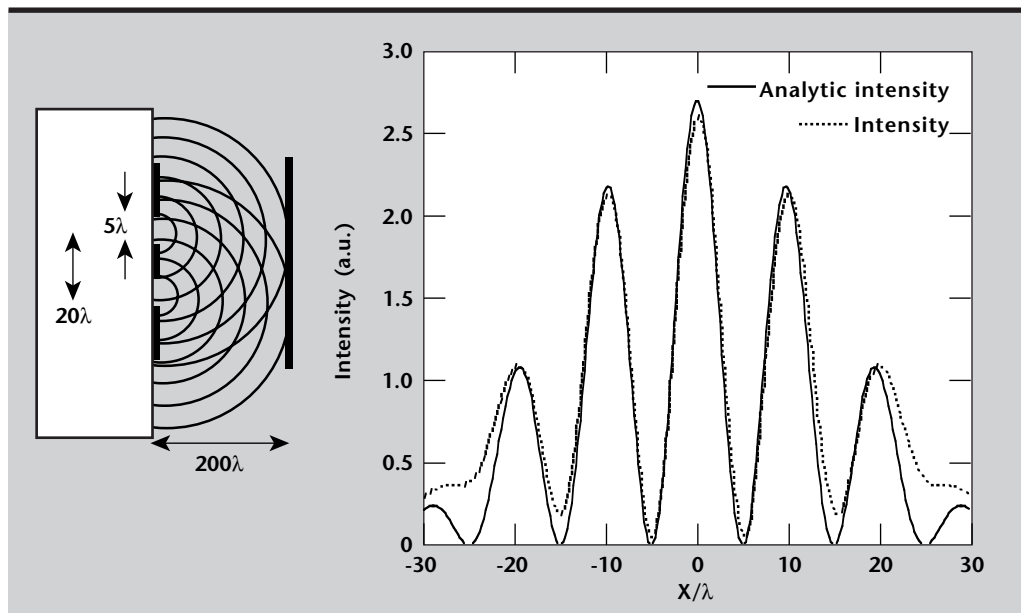


Figure 2. Wigner phase-space method calculation of double-slit diffraction by ray tracing.

Figure 3. PHASTER calculation of propagation through three slabs. The tilted distribution on the right is the manifestation of diffraction in the ray phase space.

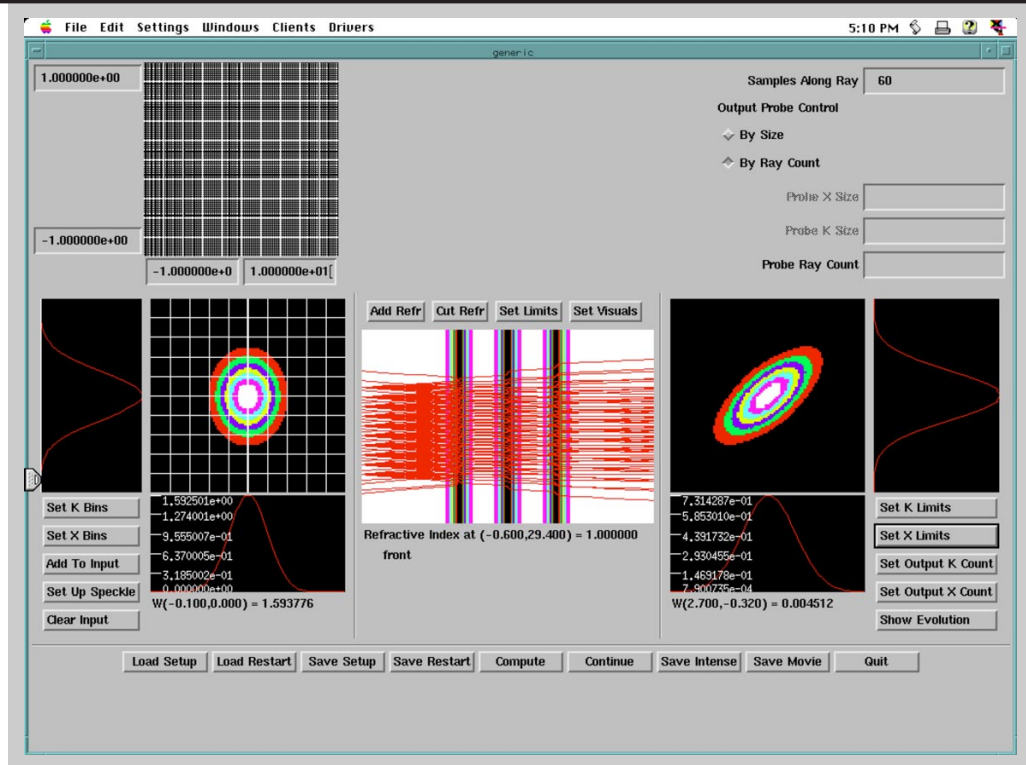
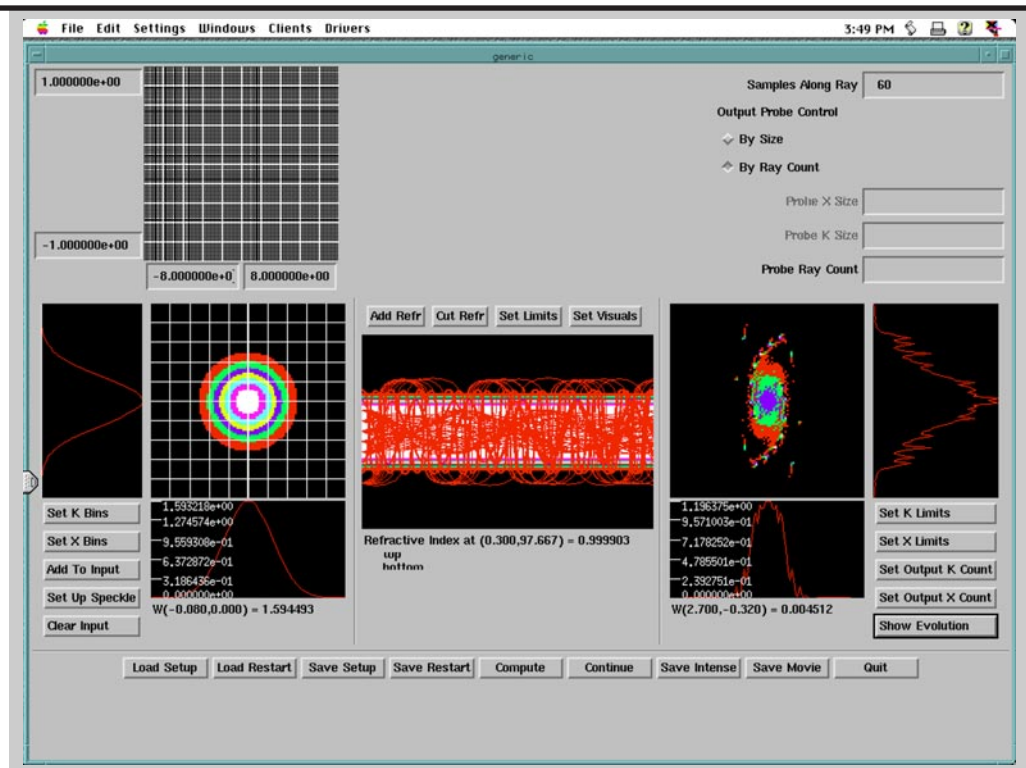


Figure 4. PHASTER calculation of waveguide propagation, showing rays with transverse turning points.



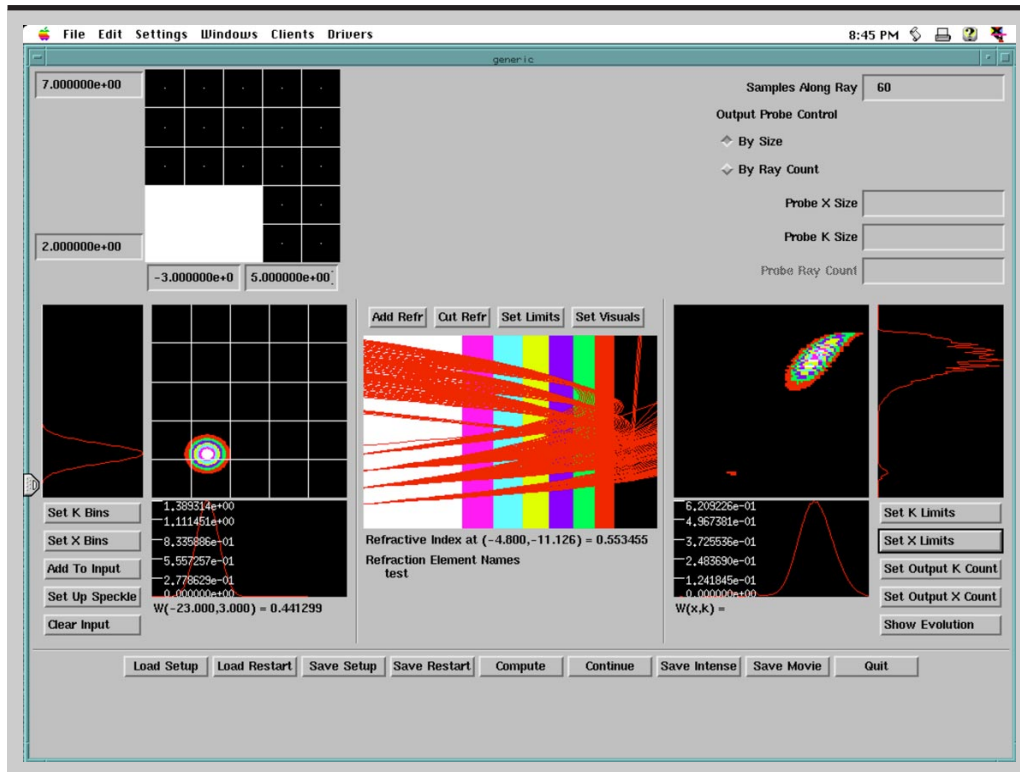


Figure 5. PHASTER calculation for oblique incidence on inhomogeneous plasma with linear density gradient.

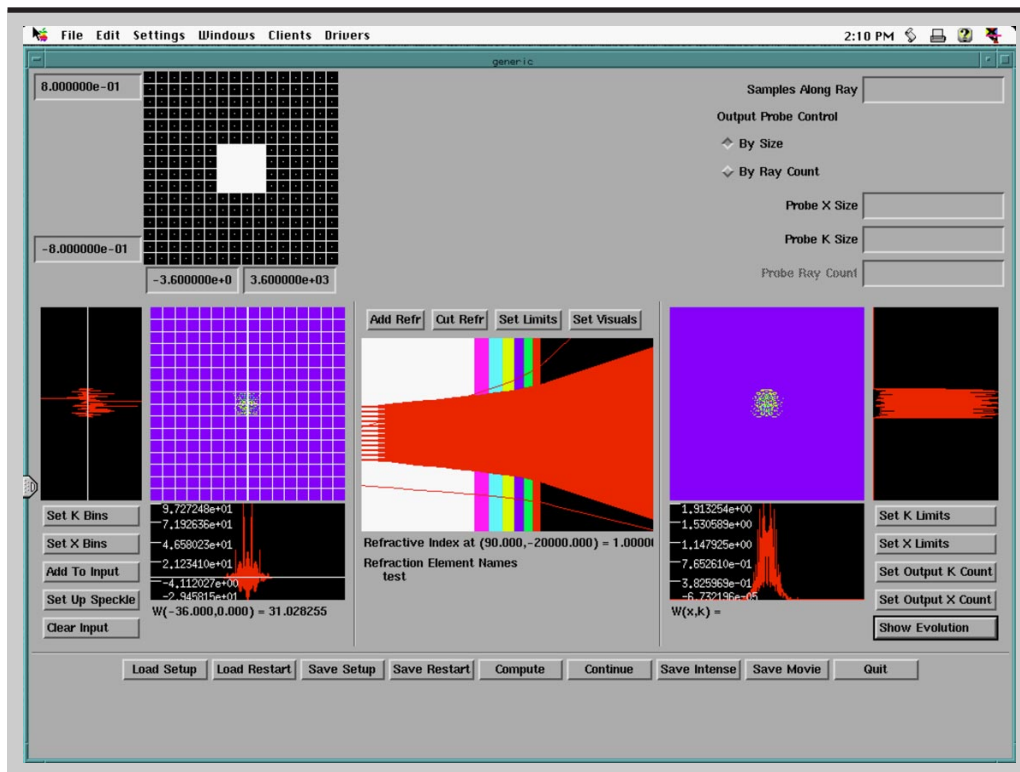


Figure 6. PHASTER calculation for speckled beam at normal incidence on inhomogeneous plasma.

the central window of the GUI. The contour plot on the left shows the initial Wigner distribution of the Gaussian. Below it we see the x-space intensity, and to the left the angle-space intensity (far field). The windows on the far right show the analogous data for the propagated distribution. Note that the phase-space distribution has become elongated and tilted: this is simply a graphic depiction of diffraction.

Rays at large-magnitude angles (top and bottom of distribution) move fastest in x, while small-angle rays (near center of distribution) move little. The result is a spreading of the x-space distribution while the angular distribution does not change, exactly what we would expect from simple free-space diffraction. Due to the plates, additional spreading occurs in x-space but not in angle, because rays receive no transverse impulse from the axially varying index.

Figure 4 shows propagation in a waveguiding structure. The rays are obviously confined to the waveguide, and at the exit have formed a “galaxy-shaped” distribution. A given ray will encircle the origin as it traces out a periodic path, but the frequency of the rotation decreases as the angle increases, causing the spiraling.

A third example is shown in **Fig. 5**. Here a beam is incident at an oblique angle on a linear index gradient, a model for a laser propagating in a plasma. A subset of the rays is reflected by the plasma index gradient, while the rays getting through form the distorted distribution on the right. This example is of particular interest because the problem admits an exact solution in terms of Airy functions,⁴ and thus will allow direct evaluation of accuracy.

Our final example (**Fig. 6**) shows the propagation of a speckled beam through the inhomogeneous plasma. By speckled we mean that we are launching a set of Gaussians with a distribution of transverse tilt angles and random phases. Propagation of speckle is important for laser-plasma interaction physics and also for propagation in multi-mode fiber. Again, an exact solution to this problem is available.

An important feature of the code is its flexibility in sampling the phase space at the entrance plane so as to put a higher density of rays where the Wigner distribution has larger values. Sampling is critical for the method, because if we do not sample wisely we suffer in computational efficiency for a given accuracy. PHASTER allows us to divide the phase space into rectangular bins and vary the size of the subdivisions of the bins.

Future Work

The Wigner method shows great promise as a wave propagation algorithm, and much remains to be done to fully exploit its capabilities. To treat reflections accurately, for example, requires extending the calculation to the time domain.


The method will be most effective when it is relatively inexpensive to trace rays, as in bulk optics where all that is required is Snell's law of refraction (and reflections if wanted) at boundaries. We are in the process of developing a 3-D bulk optics solver. Up to now, we have ignored polarization, which can also be included. More subtle effects, such as accurately calculating tunneling, will require propagating complex rays.

We recognize that using rays is only a first step for the method to come to fruition. Because rays are 1-D, it is difficult to sample a 2- or 3-D space effectively. One extension is to use “fat rays,” or Gaussian basis functions, whose centers propagate along a ray.

Ultimately, we envision using a wavelet basis, which can optimally sample a system that has disparate length scales. Resolution can be applied only where needed, and crude representations retained where they cause minimal harm. This way, from rays to full wave optics in phase space, can be simulated by retaining a hierarchy of successively more accurate approximations.

In FY-99 we are focusing on applications of the Wigner method to multi-mode photonics, where effective simulation tools are in demand but full wave optics solvers are computationally difficult.⁵

References

1. Wolf, E. (1978), “Coherence and Radiometry,” *J. Opt. Soc. Am.* **68**, pp. 6–17.
2. Bastiaans, M. (1997), “Application of the Wigner distribution function in optics,” in *The Wigner Distribution: Theory and Applications to Signal Processing*, W. F. G. Mecklenbräuker, ed., North-Holland, Amsterdam.
3. Wigner, E. (1979), “On the quantum correction for thermodynamic equilibrium,” *Phys. Rev.* **40**, pp. 749–752.
4. Afeyan, B. B. (1996), *Bull. Am. Phys. Soc.* **41**, No. 7, paper 9Q2, p. 1598.
5. Ratowsky, R. P., B. B. Afeyan, J. S. Kallman, and M. D. Feit (1998), “Propagation modeling for multimode photonics,” Lawrence Livermore National Laboratory, Livermore, California (UCRL-JC-131253-ABS). 



Technologies for Advanced Induction Accelerators

Maurice A. Hernandez

*Defense Sciences Engineering Division
Electronics Engineering*

The Technologies for Advanced Induction Accelerators project is aimed at developing the technologies necessary for a commercial fusion energy source. In FY-98, we developed components for tailored beam acceleration and bending, continued our modeling efforts, and conducted beam dynamics experiments.

Introduction

The Technologies for Advanced Induction Accelerators Project has just completed the second year of a three-year effort. This project is one component of the Inertial Fusion Energy (IFE) research at Lawrence Livermore National Laboratory, aimed at developing the technologies necessary for a commercial fusion energy source. We have focused on the concept of indirect drive targets using a heavy ion accelerator. A 1991 study showed that a recirculating accelerator (or recirculator) is a promising candidate for a cost-effective IFE driver. A recirculator is exactly what its name implies—an accelerator in which the beam travels around a ring-shaped configuration, repeatedly passing through each accelerating element.

Progress

We have used the HIF Small Recirculator (which presently has one-quarter of the full ring completed) as a test bed. Our work in FY-98 concentrated on 1) developing the components necessary for tailored beam acceleration and bending; 2) continued modeling efforts aimed at constructing efficient beam steering correction algorithms; and 3) conducting beam dynamics experiments to further our understanding of the beam control parameters.

Acceleration of the recirculating beam requires high-efficiency induction core materials driven by high-repetition-rate, programmable, pulse waveforms. As the beam is accelerated, it gains both kinetic and electrical energy. In addition, our acceleration scheme calls for compressing the beam to help reduce emittance effects. The induction core

modulators must thus be able to produce precise, fast-rise-time waveforms with varying shapes, amplitudes, and widths.

During FY-98, we designed and built two prototype versions of the required modulator. One version is based on four parallel MOSFETs and associated drivers configured as switching circuits, while the other version uses the MOSFETs as linear control elements, complete with feedback and proportional drive circuitry.


The linear version has demonstrated acceptable voltage regulation at average currents in excess of 200 A, and peak currents in excess of 800 A. This performance level is consistent with that required for the recirculator. We expect to build and install modulator boards (based on the linear prototype) to drive the induction cells on the existing 90° recirculator early in FY-99.

The dynamic beam parameters also require that we drive the beam-bending dipoles with varying voltage levels. As the beam becomes more energetic, the dipole voltage necessary to provide the proper bending increases. During FY-98, we installed and tested a prototype bending dipole pulser on the small recirculator. Pulser performance was mixed. Its power stages performed as expected, but we experienced unexplained failures in some of the output transformers. In addition, we worked to modify the pulser's waveform generation and control feedback elements, to integrate the pulser into the existing recirculator timing, control, and diagnostics sub-systems, and to compensate for the effects of output loading and filtering.

We conducted beam dynamics experiments using the modified pulser, which determined the relative effects of timing, voltage level, and output ripple on

beam bending. We will conduct further bending experiments once the induction core modulators have been brought online.

We have used beam modeling throughout this project to develop steering control algorithms and to identify critical beam control issues. During FY-98, we studied the relative merits of two fundamental steering methods, which will help determine the best configuration for steering modules on the small recirculator.

The first method applies steering corrections based on measured values of beam position, velocity, and momentum. This method tends to impart larger “kicks” to the beam, using relatively fewer steering modules. The second method is based on solving simultaneous equations designed to minimize functions based on measured beam displacements and steering module voltages. This method tends to apply smaller “kicks” using steering modules in more locations. We will carry out experiments in this area during FY-99. 



TIGER: An Object-Oriented Time-Domain Simulation Code

David J. Steich, Jeffrey S. Kallman, and Gerald J. Burke

*Defense Sciences Engineering Division
Electronics Engineering*

S Terry Brugger

*Computer Applications Sciences and Engineering
Computation*

Daniel A. White

*Center for Applied Scientific Computing
Computation*

This report discusses our progress to date and our future plans for the Time-Domain Generalized Excitation and Response (TIGER) code. TIGER is an object-oriented computational electromagnetics (CEM) field solver. A prototype version of TIGER was built last year. This year we extended the code to model more realistic structures, and began building the next version. We also studied the incorporation of thin-wire algorithms. Our FY-99 plans include the continued development of the parallel-hybridized version of TIGER and the building of a powerful GUI for the code.

Introduction

There is a significant need to advance our time-domain simulation capabilities. Projects desiring more advanced CEM include antenna applications, vulnerability and susceptibility assessments, field/radiation effects due to outside stimulus, full-wave field behavior of kickers, splitters, induction cells, broadband phased arrays, Eigenvalues/Eigenvectors of lossy cavities, and lightning assessments, to name a few.

Time-domain CEM techniques have been in existence for more than 30 years and have grown in popularity. There are now hundreds of publications each year in the area as the techniques have matured. With so much previous work, it remains a challenge to keep up with the latest approaches. Often today it does not suffice to apply a single method to a complex application. Although we are living in an age where simplicity is preferred over complexity, the advantages of hybridized solutions cannot be ignored. However, the management of this complexity comes at a price. This price is usually delayed technology advances and increased effort to solve the problem.

The TIGER project endeavors to circumvent much of the complexity involved in judiciously applying multiple algorithms to a given geometry to improve accuracy and lower computational overhead. TIGER accomplishes this management of complexity by using object-oriented techniques.

This report describes our continuing progress in modeling components for the Advanced Hydrotest Facility (AHF) at Lawrence Livermore National Laboratory (LLNL), our parallelization progress, and our current efforts to model thin wires in the time domain.

Progress

Last year we built a prototype version of TIGER and modeled a Beam Position Monitor (BPM), which is essentially a 1/10-scale version (1/100 volume) of a simplified kicker. We achieved a greater than 100-fold reduction in the number of cells required to simulate the BPM with comparable or improved accuracy. We also performed extensive testing and validation of the code.

Testing and validation included comparisons with analytic solutions, convergence studies, and careful study of known error sources often found in these simulations, such as absorbing boundary conditions and accurate modeling of sources and feeds.

Last year's results were limited to monopole and dipole wakefield calculations of a BPM. This year we chose to model a full scale 3-D kicker structure built as a prototype design for LLNL's AHF programs, and obtained wakefield results for modes $m = 0$ through $m = 4$. Previous modeling was limited to $m = 0$ and $m = 1$ for a scaled BPM geometry only.

Figure 1 is a photograph of a prototype accelerator kicker for LLNL's Experimental Test Accelerator (ETA-II). Shown in **Fig. 2** is a view of a CAD kicker model. **Figures 3** and **4** depict the real and imaginary transverse quadrupole wake impedances of the kicker, respectively. **Figures 5** and **6** depict normalized sextupole ($m = 3$), and dipole ($m = 1$) transverse wake potentials for an $m = 3$ source, respectively.

Results show that the dipole wakes caused by a sextupole excitation are not insignificant and must be taken into account. This is in agreement with experimental evidence of the kicker. Preliminary testing of the kicker shows a triangular-shaped beam hitting a foil for large input beam radius (**Fig. 7**), suggesting a large sextupole wakefield. Research into understanding this phenomenon is ongoing.



Figure 1. Photograph of prototype ETA-II accelerator kicker.

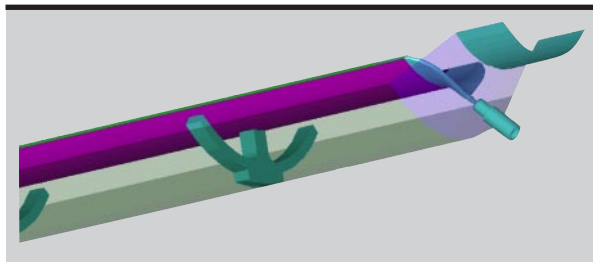


Figure 2. CAD enlargement of feed transition region for prototype ETA-II accelerator kicker.

Also in FY-98, we focused on building the next major parallel version of TIGER. This next version will be even more capable, flexible, and extensible. Shown in **Fig. 8** is a plot of speed-up versus number of processors for TIGER's preprocessor on the ASCI Blue machine. The geometry is a 234,000-cell mesh that is partitioned on 1, 2, 4, 8, 16, and 32 processors. We are getting excellent speed-ups up to 32 processors.

The slight decrease in speedup performance for the 16- and 32-processor runs is due to the extra communication that is involved. Since we are splitting up the same geometry on successively more and more processors, the surface to volume ratio is increasing. This means there is less relative work to do for a given amount of required communication. In general, we must communicate the entire outer surface cell layer(s) of the geometry to adjacent processors. For 32 processors, there are only roughly 7312 cells per processor.

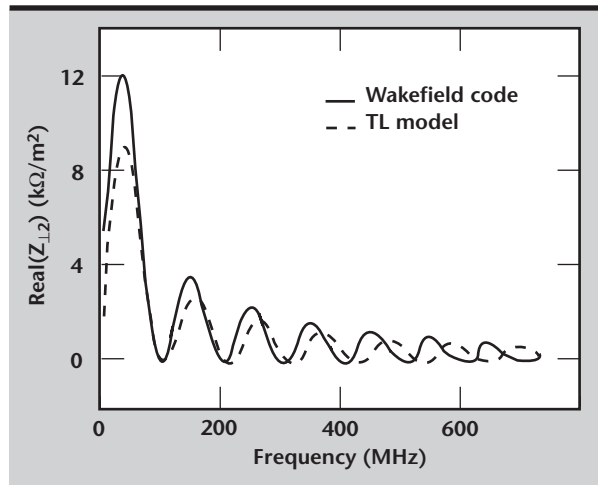


Figure 3. Real transverse quadrupole wakefield impedance for prototype ETA-II accelerator kicker.

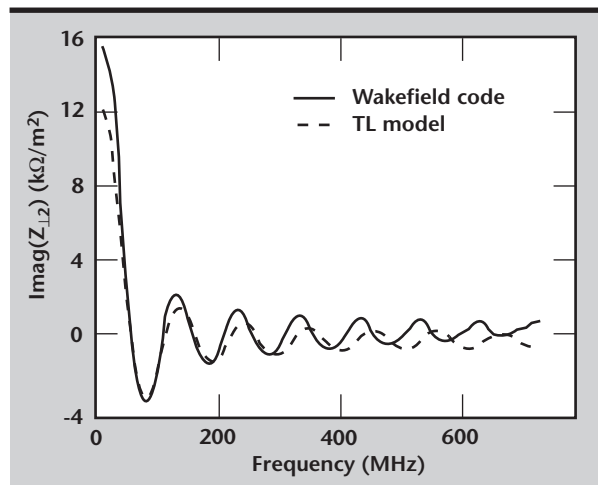


Figure 4. Imaginary transverse quadrupole wakefield impedance for prototype ETA-II accelerator kicker.

If we would instead increase the geometry so that the number of cells per processor remained a constant, our speed-up would again start to approach perfect speed-up performance. For real production runs we would keep at least several hundred thousand cells per processor. It is our intent to eventually run problems with tens to hundreds of millions of cells.

Time-Domain Thin-Wire Capabilities

Adding thin-wire capabilities to TIGER would greatly extend its usefulness to LLNL programs. There are applications in micro-impulse radar, nonproliferation, defense technologies, and the Department of Defense that could utilize thin-wire simulation capabilities. While finite-difference and finite-volume techniques are very powerful and have found widespread use in electromagnetics, modeling

thin wires in such algorithms presents several challenges. The wires are usually much thinner than the desired cell size. Several methods, which use either contour path integration, integral equations for wire currents, or transmission line equations have been used. Each of these methods has different advantages and disadvantages. However, each of the above mentioned techniques requires the wires to lie along electric or magnetic mesh edges, which restricts the wire geometry when cells are orthogonal. Furthermore, with more general meshes, generation of a new mesh is required when a wire is moved.

Our goals for FY-98 were to implement a thin-wire algorithm and see if we could generalize the algorithm to move the wire laterally along the grid. This would be the first step toward having an arbitrary wire within the grid without having to mesh the wire.

We successfully implemented thin-wire algorithms by Holland¹, Riley², and Taflov³. We also improved the accuracy of Holland's method and generalized the algorithm to allow for wires moved laterally within a mesh. Results for our new scheme are shown in **Fig. 9** for the real part of a dipole impedance for a thin wire of 0.001-m radius with a cell size of 0.035 m for various wire locations within an FDTD cell.

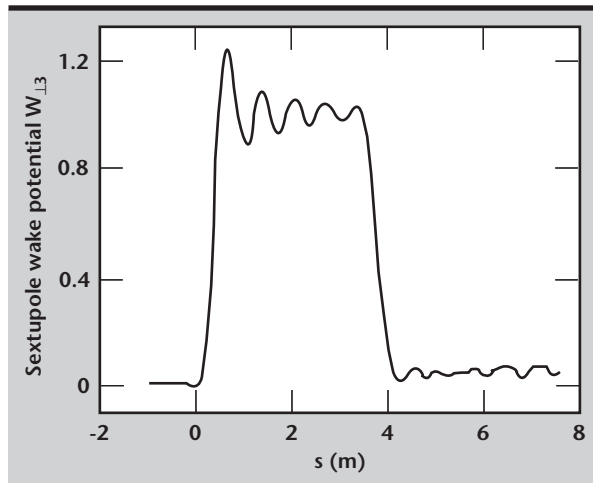


Figure 5. Normalized sextupole ($m = 3$) transverse wake potential for an $m = 3$ source.

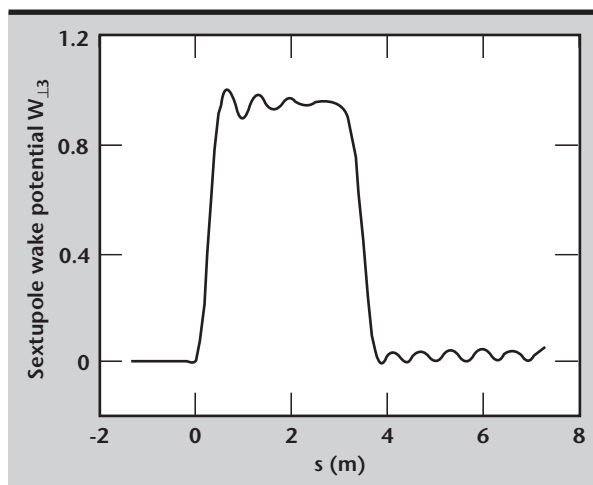


Figure 6. Normalized dipole ($m = 1$) transverse wake potential for an $m = 3$ source.

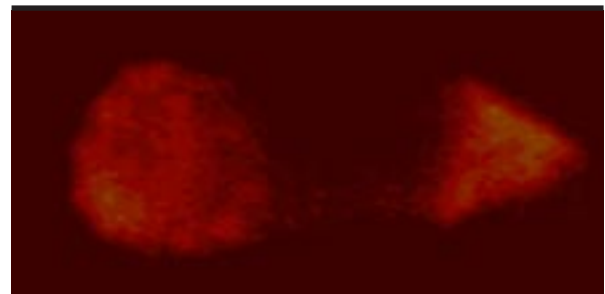


Figure 7. Experimental results for triangular-shaped beam hitting foil, for large input beam radius in the prototype ETA-II accelerator kicker.

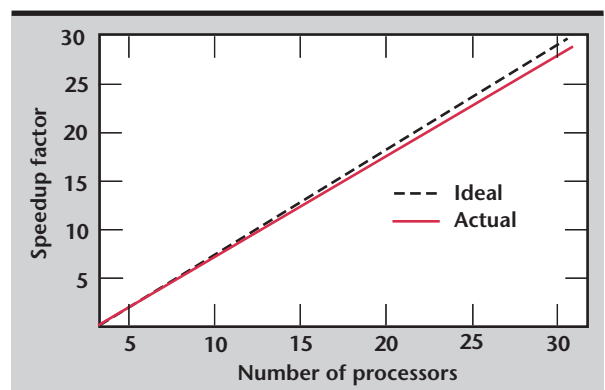


Figure 8. TIGER preprocessor speed-up factor vs number of processors on ASCI-blue.

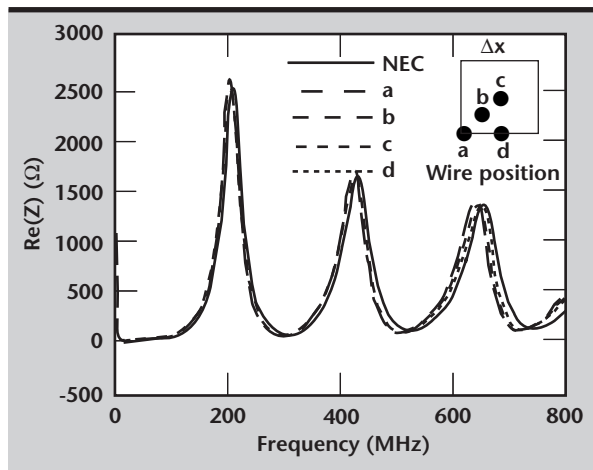


Figure 9. Thin-wire results for dipole moved to various locations within a cell.

Shown in **Fig. 10** is Holland's scheme for the same dipole impedance. Note the large variation in the real part of the dipole impedance of Holland's scheme for various wire locations.

Future Work

Next year, our technology-base focus will be to provide a powerful graphical user interface (GUI) for TIGER. This GUI will be object-oriented and allow many of TIGER's capabilities to be used in a user-friendly environment. We will continue to extend the parallel version of TIGER. Extensions will include the parallelization of the solver and the simultaneous hybridization of mesh types and physics algorithms.

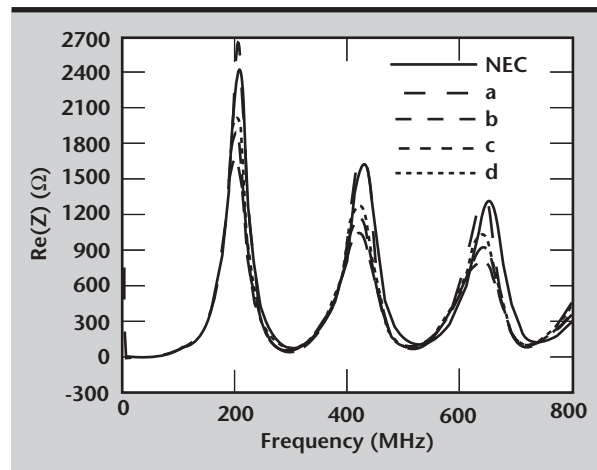



Figure 10. Holland's thin-wire results for dipole moved to various locations within a cell.

References

1. Holland, R. (1981), "Finite-Difference Analysis of EMP Coupling to Thin Struts and Wires," *IEEE Trans. Electromag. Compat.*, Vol. EMC-23, No. 2, May.
2. Riley, D. J., and C. D. Turner (1998), "The VOLMAX Transient Electromagnetic Modeling System, Including Sub-Cell Slots and Wires on Random Non-Orthogonal Cells," *Fourteenth Annual Review of Progress in Applied Computational Electromagnetics*, March.
3. Umashanker, K. R., A. Taflove, and B. Beker (1987), "Calculation and Experimental Validation of Induced Currents on Coupled Wires in an Arbitrary Shaped Cavity," *IEEE Trans. Antennas and Propagation*, Vol. 35, pp. 1248-1257. 



PUS: An Optically Parallel Ultrasound Sensor

Jeffrey S. Kallman

*Defense Sciences Engineering Division
Electronics Engineering*

Dino R. Ciarlo

*Engineering Research Division
Electronics Engineering*

Elaine Ashby and Graham H. Thomas

*Manufacturing and Materials Engineering Division
Mechanical Engineering*

This development project addresses the need for a faster, less expensive method of transmission ultrasound. It uses the principle of frustrated total internal reflection to transduce acoustic pressure into optical modulation. An entire 2-D plane of data at a time can be acquired. We describe the modeling and verification of a final sensor design.

Introduction

Ultrasound imaging is used to inspect parts, monitor processes, and diagnose problems in human patients. Soon after x-ray CT was invented, attempts were made to do the same kind of imaging with ultrasound. One of the many problems encountered was the difficulty of acquiring the necessary data in a timely fashion. Other problems included the tendency of ultrasound not to travel in straight lines, and to require a couplant between source, object, and sensor.

The existence of these problems is unfortunate, considering that 3-D volumetric imaging by ultrasound would be quite useful for screening for breast cancer. Consider the advantages: no ionizing radiation, no compression, and no toxic developing solutions or film. At present the only way to get the information necessary to do this kind of imaging is to use arrays of piezoelectric sensors, and either multiplex them in time or have multiple copies of the necessary electronics to read them, which is expensive. The sensor we are developing addresses these problems.

Our new sensor uses the classical optical phenomenon, frustrated total internal reflection (FTIR), to make the incident ultrasonic wave modulate a beam of light, which is then acquired by a

camera and computer. A sequence of images, each taken at a different source acoustic phase, enables us to reconstruct the ultrasonic phase and amplitude over an entire 2-D surface.

In this report we detail the development and design of our optically parallel ultrasound sensor.

Optics

FTIR is a consequence of the wave nature of light.¹ When light moves from a slow medium to a fast one, there is a critical angle, $\theta_c = \sin^{-1}(n_2/n_1)$ (where n_1 is the index of refraction of the slow medium and n_2 is the index of the fast medium), beyond which the light is totally reflected. However, an evanescent wave extends a short distance (approximately one wavelength) into the fast medium, and if another piece of slow medium intercepts this evanescent wave, some of the light tunnels across the gap (**Fig. 1**). How much light tunnels is a function of the angle of incidence, the indices of the media, and, most importantly from our point of view, the size of the gap.

We can exploit this effect to build an array of acoustic pixels. Each acoustic pixel is composed of a thin silicon nitride membrane suspended on short gold walls over an optical substrate. The gap

between the membrane and the optical substrate is filled with air (**Fig. 2**). The entire assembly is immersed in the ultrasonic couplant. When an ultrasonic pressure wave impinges on the acoustic pixel, the membrane deflects, causing a change in the amount of light reflected from the total internal reflection surface of the acoustic pixel. An entire array of acoustic pixels can be used to modulate a beam of light.

The information we desire from this sensor is the phase and amplitude at each acoustic pixel. To obtain this information we illuminate the sensor with ten sequences of optical pulses, each sequence timed to act as a strobe light at a specific acoustic phase (**Fig. 3**). We extract the phase and amplitude at each pixel by fitting the intensity at that pixel through the sequence to the form $I = B + A \sin(2\pi i/10 + \phi)$, where I is the intensity, B is the background, A is the amplitude of the sinusoidal variation, i is the index of the image in the sequence, and ϕ is the phase of the variation.

The optical train of this device is as follows: we illuminate the sensor using an LED, the light from which is homogenized, polarized, and collimated. We acquire the reflection from the sensor using a CCD still camera.

Acoustics

The inspection technique we are interested in is transmission ultrasound. In this modality, an acoustic source sends out pressure waves through a couplant, such as water, oil, or medical ultrasound gel, to the object of interest. The pressure waves are transmitted through the object, being changed in amplitude and phase along the way. The pressure wave emerges from the object of interest and travels, via the couplant, to an acoustic sensor. The sensor determines the acoustic phase and amplitude, either

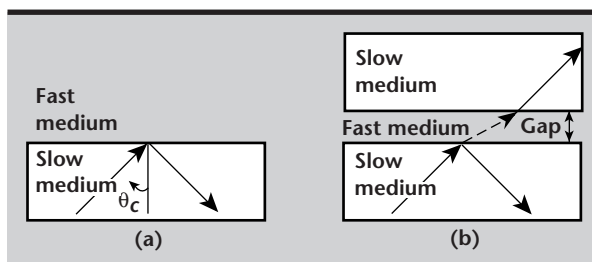


Figure 1. (a) Illustration of total internal reflection. Light trying to exit the slow medium at an angle higher than the critical angle will be completely reflected. (b) Frustrated total internal reflection. The evanescent wave that extends into the fast medium overlaps another piece of slow medium, and some of the light tunnels across the gap. The amount of light that tunnels through the gap is sensitively dependent on the size of the gap.

at a point, on a line, or in a plane. The sensor we are developing will measure the acoustic phase and amplitude of an entire plane at a time.

Our sensor works because the pressure wave causes the flexing of a membrane, causing it to vibrate with a phase and amplitude that are functions of that wave.

In designing our sensor, we needed to have a membrane with a frequency response high enough to vibrate at the frequencies of interest to us (approximately 1 MHz).

Progress

Modeling

We began our work on this project by modeling as many of the systems and processes as possible. We used TSARLITE to model the optical elements of the sensor (FTIR), DYNA3D to model the acoustic responses of the membranes and their supports, and

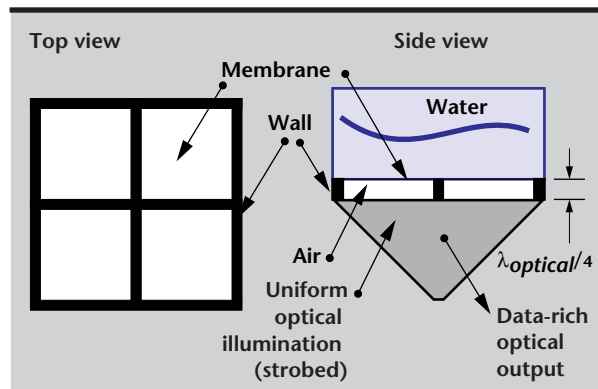


Figure 2. Illustration of an acoustic pixel, a thin membrane suspended over an optical substrate by gold walls. There is an air gap between the membrane and the optical substrate, and the acoustic pixel is exposed to water. An ultrasonic pressure wave moving through the water will cause the membrane to vibrate, changing the air gap enough to modulate a beam of light reflected from the total internal reflection surface of the optical substrate.

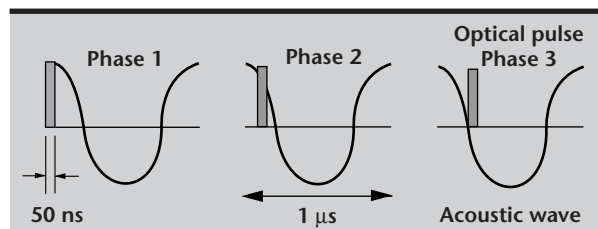


Figure 3. Illustration of the illumination of the optical substrate at particular times during the acoustic wave. This causes the optical beam to act as a strobe light. A sequence of ten images allows us to deduce the motion of each acoustic pixel through the acoustic wave, and thus the pressure and phase of the acoustic pixel excitation.

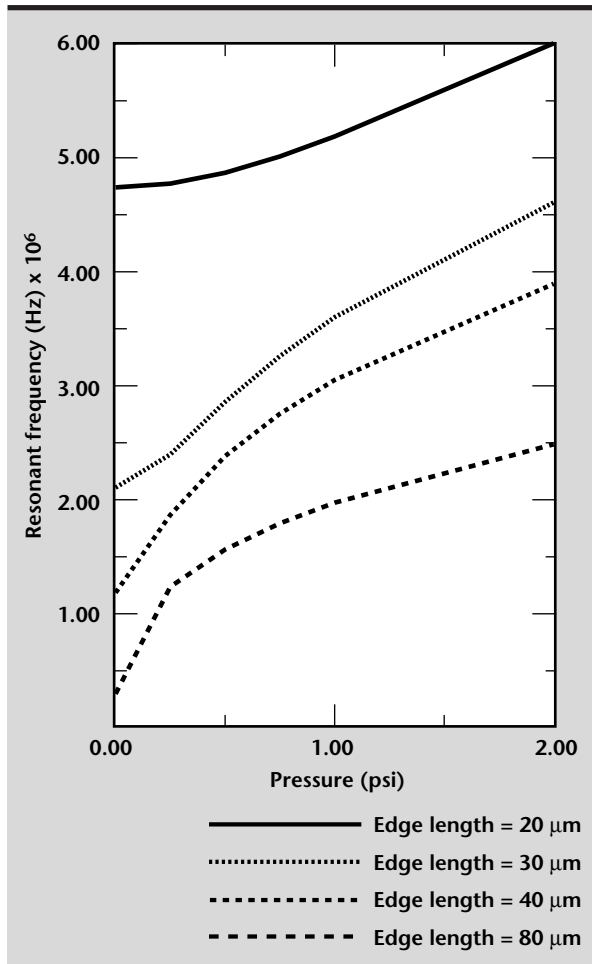


Figure 4. Graph showing how the resonant frequency of a set of simulated acoustic resonators varies with the hydrostatic pressure load.

a modification of BEEMER to model the imaging system as a whole.

Using TSARLITE, we were able to determine the ranges where we could expect FTIR to be useful, and bounded the permissible thickness of the membrane and the heights of the supports it would stand upon. This aspect of the modeling was performed to make certain that we would be able to engineer to the physical phenomenon we were using.

The modified BEEMER program was used to examine the issues that will arise when we use the sensor for diffraction tomographic imaging. It was used to model the tomographic data acquisition processes, as well as a variety of reconstruction algorithms.

The simulation program we used most was DYNA3D. We used this program to model our first sensor design, a membrane suspended on an array of posts. DYNA3D showed us that this design had neither the sensitivity nor the frequency response necessary to allow us to acquire the data we needed. Guided by our simulations, we developed a more responsive design, a set of resonant membranes suspended on walls (Fig. 2). Simulation showed this design was responsive and sensitive, but had problems with cross-talk and drift of the resonant frequency as a function of hydrostatic pressure (Fig. 4). Further simulation allowed us to modify the design so as to greatly reduce cross-talk (Fig. 5).

Simulation eliminated the need to experiment blindly, but we still needed to do experiments to verify that the simulations were correct, and get proof of principle system. To do these experiments we built a test system.

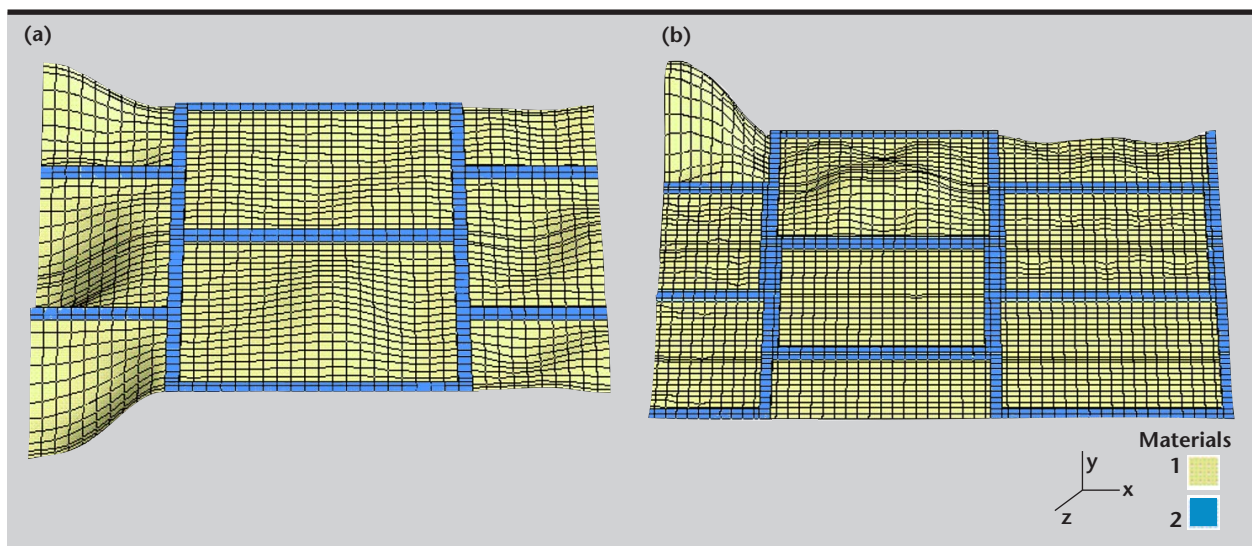


Figure 5. Simulation Results. (a) All of the acoustic pixels in this simulation have the same resonant frequency. An excitation of the rear left pixel spreads to all the surrounding acoustic pixels. (b) Staggering the sizes of the acoustic pixels greatly reduces the spread of energy (cross-talk).

Verification

The test system we built consisted of the test membrane, a tank with an acoustic source, and the optics. The test membrane was designed to allow us to examine the responses of a wide range of membrane resonator sizes to variations in hydrostatic pressure. The rest of the system was designed to make all of the parameters of interest easily available for manipulation.

The test membrane consists of a 1-cm-by-1-cm membrane of silicon nitride, supported by gold walls, held in a silicon frame. The gold walls are patterned as shown in **Fig. 6**. On the left hand side of the test membrane are alternating rows of 60 acoustic pixels ranging in size from $20\text{ }\mu\text{m}$ to $80\text{ }\mu\text{m}$ on a side. On the right hand side of the test membrane only half of the rows are populated with acoustic pixels. The reason for the wide range in size is evident from **Fig. 4**.

We suspected that only acoustic pixels that were at the exact resonant frequency would be sensitive enough to modulate the optical input, and so attempted to include all pertinent sizes. In addition to the wide range in resonator sizes available we had membrane fabrication parameters available for modification as well, that is, membrane thickness and gold wall height.

The remainder of the system is illustrated in schematic form in **Fig. 7**. The oscillator provides a 1-MHz signal, which is amplified and fed through the power meter to the acoustic source in the

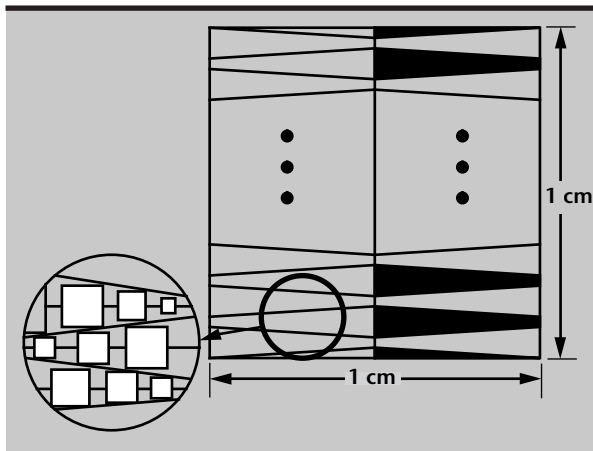


Figure 6. Schematic of the pattern of acoustic pixels in the test membrane. On the left are alternating rows of 60 acoustic pixels ranging in size from $20\text{ }\mu\text{m}$ to $80\text{ }\mu\text{m}$ on a side. On the right only half of the rows are populated with acoustic pixels.

water tank. The same signal goes to the pulse generator, which in turn excites the optical source as a strobe light. The pulse generator output and the oscilloscope output are both fed to an oscilloscope to allow the user to place the optical pulse at any point in the acoustic phase. The optical pulses are homogenized, polarized, collimated, and fed through the prism to the sensing surface, and the reflected light is captured by the camera and saved in the computer. The user has control over the oscillator frequency, the amplifier gain, the camera exposure time, the optical pulse width, amplitude, and placement in the acoustic phase, and the depth of the water in the tank.

This is the procedure followed during a typical experimental run: the water tank is filled to the desired depth, and the acoustic power level, camera exposure time, optical pulse width, and optical pulse amplitude are set. Four sequences of ten images are acquired, each with the optical pulse occurring at a different acoustic phase.

We learned a great deal using the test system, most importantly that: 1) we can engineer to the sizes and tolerances necessary to use the physical phenomenon; 2) we can extract phase and amplitude data at each acoustic pixel from sequences of images; 3) the resonances are so broad as to make acoustic pixel size non-critical; and 4) hydrostatic pressure causes little change in membrane response.

After performing numerous experimental runs we were able to arrive at an optimal set of design parameters for the final sensor.

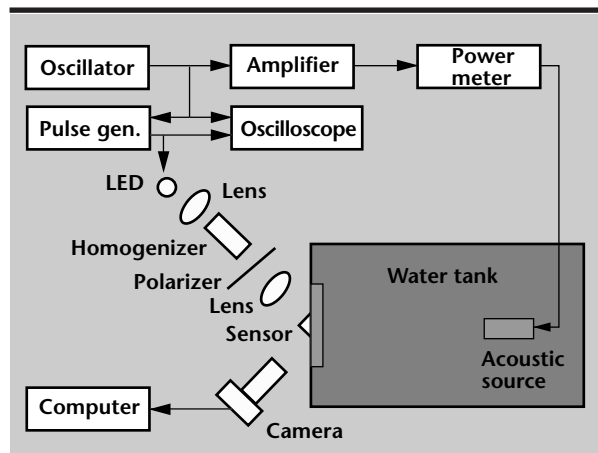



Figure 7. The test system. The oscillator drives the amplifier and pulse generator with a 1-MHz sinusoid. The acoustic source insonifies the test membrane which is illuminated with 50-ns optical pulses strobing at a user-specified acoustic phase. Images of the membrane are acquired by the camera and stored and processed in the computer.

Future Work

We have completed the design for the final sensor. The final sensor is currently in the process of fabrication. Since we have funding to continue this work in the next fiscal year, we will complete the construction of our final sensor, calibrate it, and use it to collect phase and amplitude data through a variety of test subjects. Initially we will only make 2-D transmission ultrasound images, but ultimately we will generate volumetric images of 3-D objects using data from this sensor to feed a diffraction tomography code.

References

1. Yeh, P. (1988), *Optical Waves in Layered Media*, John Wiley and Sons, New York, New York. 



Optical Transition Radiation Diagnosis for Electron Beams

Gregory P. Le Sage and Roger A. Richardson

Defense Sciences Engineering Division

Electronics Engineering

We describe the accomplishments of two technology-base projects dealing with the development of electron beam diagnostics using optical transition radiation (OTR). Diagnostic experiments using OTR were performed at the Lawrence Livermore National Laboratory (LLNL) flash x-ray facility (FXR), and at the LLNL 100-MeV RF linac facility. The original charter for the RF linac was the development of diagnostics appropriate for a high-peak-brightness electron beam. OTR appeared to be a suitable candidate for measuring micron-scale beam spots, and milliradian divergences. Transition radiation diagnostics were evaluated using the thermionic electron beam produced by the LLNL RF linac facility. The diagnostics are intended for use with the high-brightness electron beam that will be produced by a photocathode injector currently under development. The FXR effort concentrated on the use of OTR for transverse beam profile imaging at viewing angles away from the OTR radiation peaks, at time scales short compared to the bunch length. The effects of surface roughness on the radiation pattern of OTR were examined theoretically.

Introduction

Transition radiation is produced when a charged particle traverses a barrier between two media with different dielectric characteristics. This radiation emerges with a distinct angular distribution, which can be exploited to reveal electron beam characteristics that are otherwise difficult or cumbersome to measure. The basic configurations for these measurements include a single or multiple samples of dielectric or metallic material inserted into the electron beam. Using appropriate materials and optical measurement techniques, the spatial profile and the divergence of the electron beam can be measured at a single point, in a single shot.

Though the divergence of the beam is degraded by the thin (few micron) dielectric foils, it is not completely disrupted, as in the case of traditional slit projection techniques used to measure the same information. These seemingly delicate foil samples have in fact proven to be quite robust in some cases, accepting long macropulse lengths, high-average currents, high-energy beams, and relatively tight focal spots.

The equations describing this radiation are well known, but are somewhat cumbersome to use for real materials, particularly for relativistic particles. Typically, approximations are made so the equations

can be used analytically. The materials used to produce transition radiation are described by dielectric constants in the desired frequency range, both real and imaginary parts. Simplified forms of the transition radiation formulae were programmed for comparison to measured data, and for estimation of flux levels at angles away from the peaks of the OTR pattern.

A characteristic of the radiation pattern at high energies is the directivity of the back-scattered radiation. For a relativistic factor γ of 100, OTR is confined to tens of milliradians of the reflection angle. The reflection angle is equal to the incident angle, so that for a foil angled at 45° with respect to an electron beam, the radiation pattern will be centered at 90° .

This is convenient for most applications, but for the confined space available in the FXR experiment, it was not possible to view transition radiation at the proper angle of maximum intensity. To broaden the radiation pattern, the surface of an OTR foil was roughened so that a more random incident angle is presented to the electron beam.

The effects of surface roughness on an OTR radiation pattern were modeled using MATHEMATICA. The surface roughness was modeled as a random Gaussian function, centered at the foil angle. An OTR distribution was integrated over this Gaussian

function to observe the effects of this roughness model. When the foil surface roughness was increased in the model, the radiation lobes were broadened. Light produced by OTR was successfully measured at the FXR using a roughed KAPTON foil far from the optimum specular angle.

Progress

The efforts and accomplishments for the RF linac facility for FY-98 are described in this section. We have expanded the scope of the effort to include preparation of the photocathode electron accelerator.

A single foil OTR measurement in FY-98 provided the first emittance data ever collected on the high-energy S-Band RF linac beam at LLNL. The technique was proven for our beam parameters, and the diagnostic will certainly be used as the machine is improved.

A theoretical study of the angular distribution of transition radiation was performed to evaluate the measured data under our particular conditions. One can imagine that while a single electron produces a perfect angular distribution of transition radiation light, a broad thermal distribution of electrons with a large spot size produces a blurred pattern with characteristics that are not readily tractable. A simulated distribution of electrons with imposed spatial and angular distribution (MATHCAD-script developed) was used to generate characteristic OTR patterns that could be compared to measured data. Added complication results from the large spot size, which affects the optical collection of the data, and depends on the distance to the point of measurement (a CCD).

Taking all relevant effects into account, a multiple-parameter fit was performed to compare the theoretical and measured distributions (C++-code developed). Error bars were thus established between the measured data and the theoretical fit over a range of measured angles, and an emittance with specified tolerance was measured.

When two or more foils are used for a transition radiation measurement, an interference pattern is produced by the forward-projected OTR light from the first foil, and the specularly reflected light from the adjoining foils. This technique is useful since multiple peaks and nulls allow more precise evaluation of the beam divergence.

From a practical perspective, the angular pattern of light coming from a multi-foil arrangement is much less ambiguous than that from a single foil,

since the interference fringes appear to sharpen considerably as the beam and optical system parameters are properly adjusted.

Just such an effect was measured this year, again using the LLNL linac beam, and a pair of aluminized mylar foils. This measurement also provided another significant milestone in the life of the linac beam. For the first time, we had visual feedback for tuning the divergence of the linac beam at a given point. Starting with a beam spot optimized for small size and regular (round) appearance, we noticed that the OTR interference pattern was quite poor. As the fringe sharpness was optimized by tuning the linac optics, we found that the spot image became much more irregular, indicating that the beam transport system was astigmatic (horizontal and vertical focal lengths were not equal). With a remotely rotatable polarizer, the collimation in orthogonal directions can be investigated. These capabilities will provide essential information for interaction experiments between the linac beam and a short laser pulse.


In addition, the prompt light produced by transition radiation can be used to characterize the temporal characteristics of an electron beam. The FXR effort described previously included the use of a gated intensifier to measure the beam evolution. Short pulse beams can be similarly characterized using a streak camera.

Measurement of the OTR light produced by the two-foil setup using a fast-risetime PMT was performed at the RF linac facility, confirming the RF signals produced by low bandwidth beam current monitors. With the bandwidth of the PMT (3 GHz), we were able to detect changes in the macropulse as a function of time.

Future Work

In FY-99 an experiment is planned to relay-image OTR light to an optical test bench, where the image can be masked to allow precise measurement of divergence characteristics across the beam profile. If a mask with multiple apertures is used, an "optical pepper-pot" measurement will be possible, allowing reconstruction of the beam phase space. This technique would be extremely useful for the high-energy linac beam, since a collimator for a 100- to 150-MeV electron beam would be many centimeters thick. The imaging arrangement is near completion, with relay optics and wall penetrations in place. Though the concept for this technique is patented, this diagnostic has never been implemented before. We are

currently discussing this and other collaborative experiments with the two authors of the optical pepper pot diagnostic patent.

OTR has been successfully demonstrated as a useful diagnostic for two very different classes of relativistic electron beams. Closer ties are being forged between the RF linac group, FXR, and ETA II. Further development of these diagnostics is expected. 

Characterization of Electromagnetic Scattering from Defects in the EUVL Process

Lisa Wang and Scott D. Nelson
Defense Sciences Engineering Division
Electronics Engineering

Jeffrey E. Mast and Abbie L. Warrick
Laser Engineering Division
Electronics Engineering

Extreme ultraviolet lithography (EUVL) is a promising technology for producing high-resolution semiconductor features in next generation lithography. For EUVL, even small defects can pose a significant problem. Scattering models of defects, both for the substrate and the mask blank, are needed to understand the critical issues associated with mask defects. In FY-98, we have applied both asymptotic/analytical methods and numerical techniques to model the electromagnetic scattering from substrate defects to study how electromagnetic waves at optical or EUV wavelengths interact with anomalies on the substrate.

Introduction

In recent years, there has been an increasing interest in extreme ultraviolet lithography (EUVL), which is a promising technology for producing semiconductor features with resolutions $<0.07\ \mu\text{m}$. The use of EUV technology would permit the development of computer chips with faster speed and more memory storage. At EUV wavelengths, all materials become very absorptive. Therefore, unlike transmissive masks used in traditional optical lithography, this technology uses multi-layer coated reflective masks.

Currently, the mask blanks are constructed by depositing 81 alternating layers of molybdenum (Mo) and silicon (Si) on an Si substrate. Each layer pair is 7 nm thick (3 nm of Mo and 4 nm of Si), producing a 284-nm high multi-layer coating. The masks are then made by depositing absorber patterns on top of the Mo/Si multi-layer mask blanks.

Figure 1a shows the complete EUV lithographic process. The EUV light, created using a laser plasma source, is directed toward the mask using reflective Mo/Si multi-layer coated condenser optics. After the EUV light passes through the mask containing the circuit patterns, it then passes through the multi-layer imaging optics to reduce the image size to allow very small circuits to be printed.

The multi-layers are deposited using a newly developed ion beam deposition system, IBD-350, shown in **Fig. 1b**. This system is capable of producing uniform low-defect-density multi-layer-coated reflective mask blanks (**Fig. 2**).^{1,2} In depositing different layers of material for a reflective mask, ions collide with the target of Mo or Si, and are then precisely deposited on the substrate.

For EUVL, even small defects on the substrate or in the multi-layer mask blank may pose a significant problem. It is not only because of the small feature size, but also because very small defects may introduce compound errors from the multi-layer deposition process, which can then cause problems when the circuit patterns are printed. Preliminary printability models suggest that defects $>30\ \text{nm}$ in diameter may print in the EUVL lithographic process.³

There is considerable concern about the effect of defects in the EUVL mask blanks caused by contaminating particles, substrate scratches, and other imperfections that may result in printable defects. The identification of printable defects is essential to the development of projection EUVL. This is the subject of an ongoing experimental program at Lawrence Livermore National Laboratory.

The development of a realistic scattering model to predict how electromagnetic waves interact with anomalies in the multi-layer coating of the mask

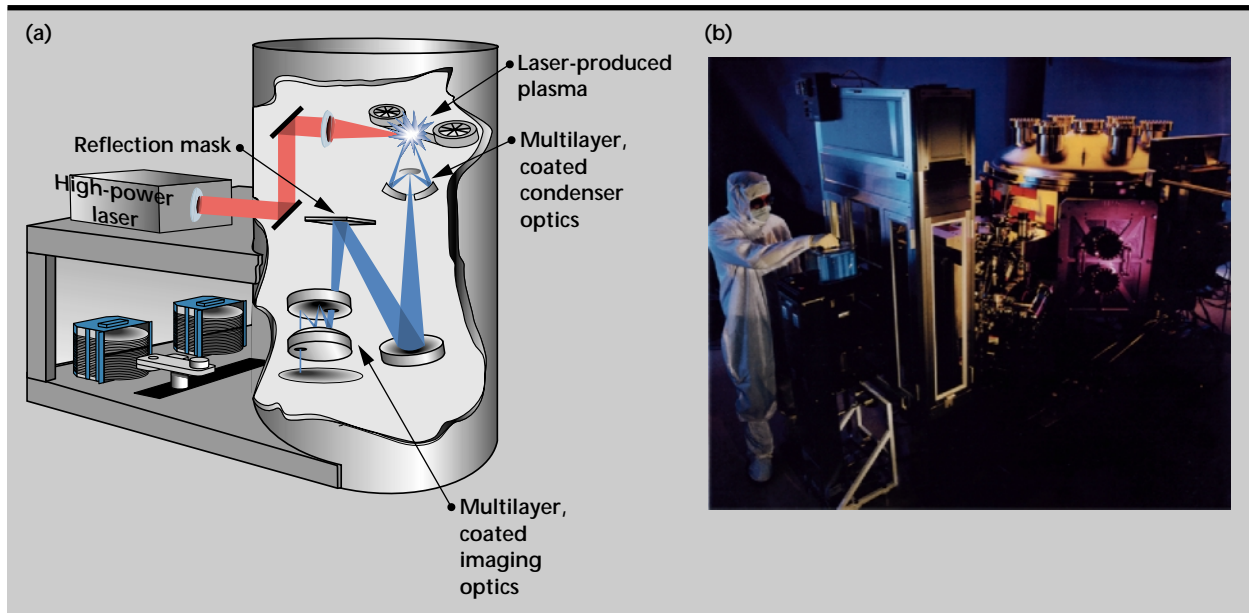


Figure 1. The EUV lithographic process. (a) EUV light is guided toward the mask using multi-layer-coated reflective optics. After the light passes through the mask and the multi-layer imaging optics, the circuit patterns on the mask are transferred onto Si wafers with reduced image size. The ion beam deposition system (b) is used to produce these uniform low-defect-density multi-layer-coated reflective mask blanks. The system includes the substrate loader and the deposition chamber where the multi-layer coatings are applied.

blank is needed for the identification of printable defects. In addition, the scattering cross-section of printable EUVL defects is needed for the development of inspection tools and effective diagnostic algorithms at both optical and EUV wavelengths.

Progress

Both asymptotic/analytical methods and numerical techniques were applied to model the electromagnetic scattering from defects on the substrate. The applicability of asymptotic/analytical methods as a function of defect size and shape was first evaluated.

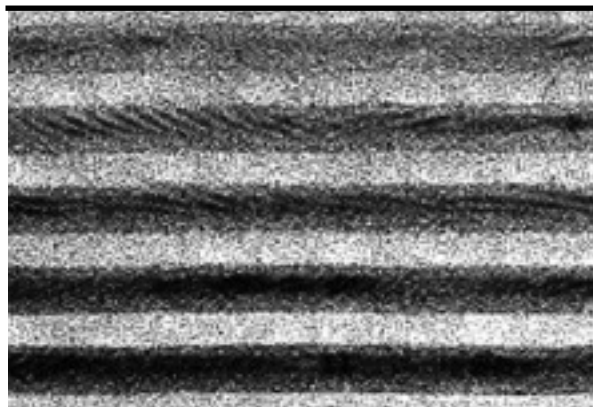


Figure 2. Magnified image of multi-layer coating, showing alternating layers of Mo and Si. The dark and light bands are Mo and Si, respectively.

Within their range of validity, asymptotic methods increase the computational efficiency at least tenfold, compared to current numerical methods, helping us gain physical insights into scattering mechanisms, and facilitating the interpretation of numerical solutions. Several asymptotic/analytical methods were examined, among which are the physical optics approximation (which is applicable when the defect is large compared to a wavelength);⁴⁻⁷ the physical theory of diffraction (which takes into account the diffracted rays due to edges, corners, and curved surfaces);^{6,8} the shooting and bouncing ray technique;⁸ and radiative transfer theory.⁷

Electromagnetic models were developed to simulate the scattering from substrate defects and particles including spheres, cylinders, disks, ellipsoids, and hemispheres. Given an incident wave E_i in the direction θ_i, ϕ_i , the first-order solution of the back-scattered electric field from a substrate defect can be expressed as

$$\begin{aligned}
 E_q^s(\bar{r}) = & \frac{e^{ikr}}{r} \left[f_{qp}(\pi - \theta_i, \pi + \phi_i; \theta_i, \phi_i) \right. \\
 & \times e^{i[\bar{k}_p^i(\theta_i, \phi_i) - \bar{k}_q^s(\pi - \theta_i, \pi + \phi_i)] \cdot \bar{r}} \\
 & + R_q(\theta_i) f_{qp}(\theta_i, \pi + \phi_i; \theta_i, \phi_i) \\
 & \times e^{i[\bar{k}_p^i(\theta_i, \phi_i) - \bar{k}_q^s(\theta_i, \pi + \phi_i)] \cdot \bar{r}} \\
 & \left. + f_{qp}(\pi - \theta_i, \pi + \phi_i; \pi - \theta_i, \phi_i) R_p(\theta_i) \right]
 \end{aligned}$$

$$\begin{aligned}
& \times e^{i[\bar{k}_p^i(\pi-\theta_i, \phi_i) - \bar{k}_q^s(\pi-\theta_i, \pi+\phi_i)] \cdot \bar{r}} \\
& + R_q(\theta_i) f_{qp}(\theta_i, \pi + \phi_i; \pi - \theta_i, \phi_i) R_p(\theta_i) \\
& \times e^{i[\bar{k}_p^i(\pi-\theta_i, \phi_i) - \bar{k}_q^s(\theta_i, \pi+\phi_i)] \cdot \bar{r}} \Big] E_p^i,
\end{aligned}$$

where q and p are the polarization components ($\{q, p\}$ = horizontal or vertical) of the scattered and incident waves, respectively; f_{qp} is the scattering matrix element; \bar{k}_p^i is the propagation vector of the incident wave; \bar{k}_q^s is the propagation vector of the back-scattered wave; \bar{r} is the location of the scatterer; $R_p(\theta_i)$ and $R_q(\theta_i)$ are the Fresnel reflection coefficients.

The first-order solution in the above equation describes four major scattering mechanisms (Fig. 3). The first term in the equation is the direct scattering from a particle (Fig. 3a). The second term is a single scattering from the scatterer, followed by a reflection off the boundary between air and the substrate (Fig. 3b). The third term is the opposite of the second term (Fig. 3c), and the fourth term describes a reflection by the boundary followed by a single scattering from the particle and further followed by a reflection off the boundary (Fig. 3d).

The scattering matrix element f_{qp} in the equation is calculated using the analytic method for different defect shapes. For example, Rayleigh and Mie scattering methods were applied to calculate the scattering returns from spheres.⁴ Scattering from cylindrical defects (Fig. 4a) was calculated using the finite cylinder approximation⁹ in which the induced current in the dielectric cylinder was assumed to be the same as that of the infinitely long cylinder of the same radius. This is a good approximation when the cylinder is long and thin compared to the wavelength. The scattered field is obtained by evaluating the field radiated from this approximate induced current source.

For disk-shaped defects (Fig. 4b), the returns were calculated using the physical optics approximation for elliptic disks,¹⁰ which assumes the internal field inside the disc to be the same as that of the infinitely extended dielectric layer of the same thickness. Numerical full-wave techniques in both the time and the frequency domain, including ANSOFT™ and TSARLITE,¹¹ were used to validate scattering returns calculated with asymptotic/-analytical methods.

The scattering result from a cylindrical dielectric defect is shown in Figs. 5 to 7 as an example

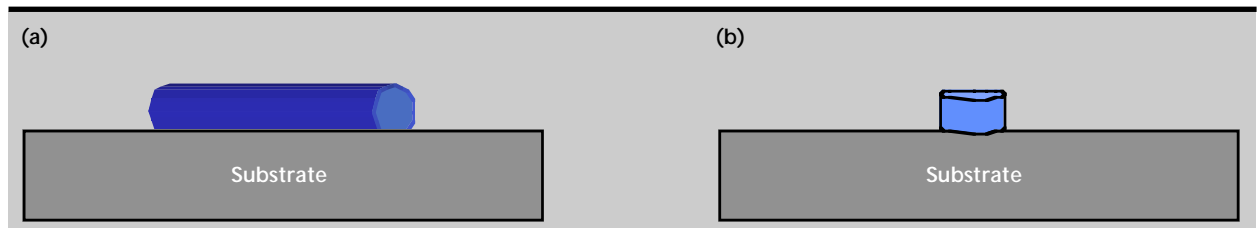
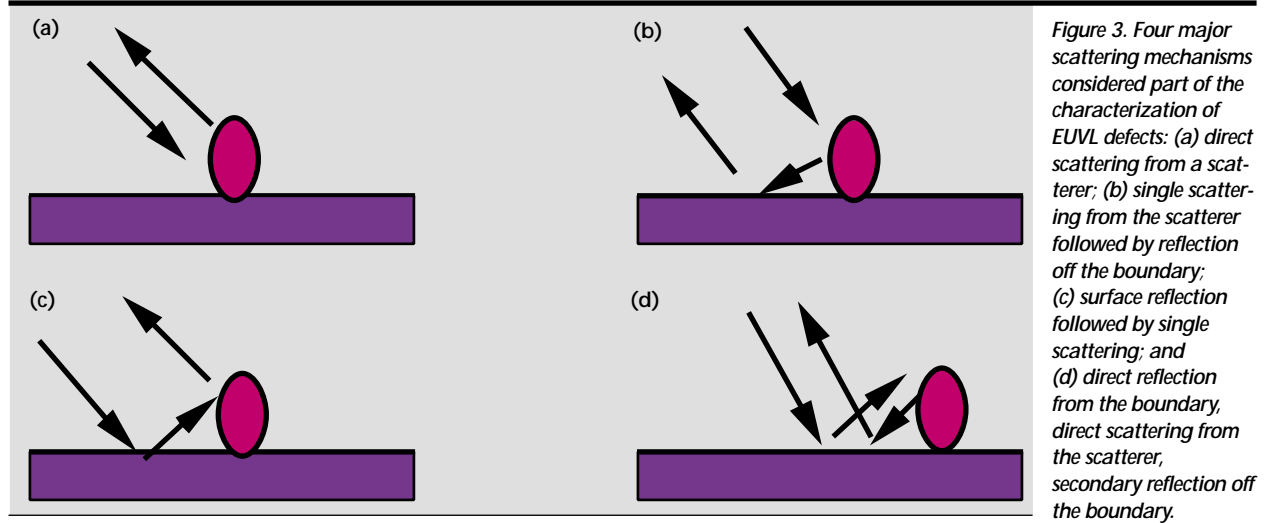


Figure 4. (a) Scattering from a cylindrical dielectric defect, calculated using the finite cylinder approximation; (b) scattering from a dielectric disk-shaped defect, obtained using the physical optics approximation.

of the results we have obtained. Before the scattering from a cylindrical defect on top of the substrate was calculated, analytic scattering results from a vertical dielectric cylinder (without considering the ground effect) was first compared with the result obtained from TSARLITE, a 2-D finite-difference time-domain code.

The 2-D problem is equivalent to taking a cut-plane at some length along the cylinder. A TSARLITE simulation of scattering from a cylinder is shown in **Fig. 5**.

In **Fig. 6**, scattering cross-sections of a vertical dielectric cylinder for HH and VV polarizations are plotted as a function of the scattering angle on the cut-plane. Scattering in the forward direction is at 0° , while back-scattering is at 180° . The vertical axis is the scattering cross-section of the cylinder in units of μm^2 , plotted in dB.

The scattering cross-section, σ_{qp} , is defined in terms of the incident field and the scattered electric field described in the previous equation, as follows:

$$\sigma_{qp} = 4\pi \lim_{r \rightarrow \infty} r^2 \frac{|E_q^s|^2}{|E_p^i|^2}.$$

For the 2-D problem, instead of scattering area, the scattering width (obtained for the infinite structure) is defined:

$$\sigma_{2Dqp} = 2\pi \lim_{r \rightarrow \infty} r \frac{|E_q^s|^2}{|E_p^i|^2}.$$

The 3-D scattering cross-section of a truncated 2-D structure can then be calculated from the approximate relationship¹²

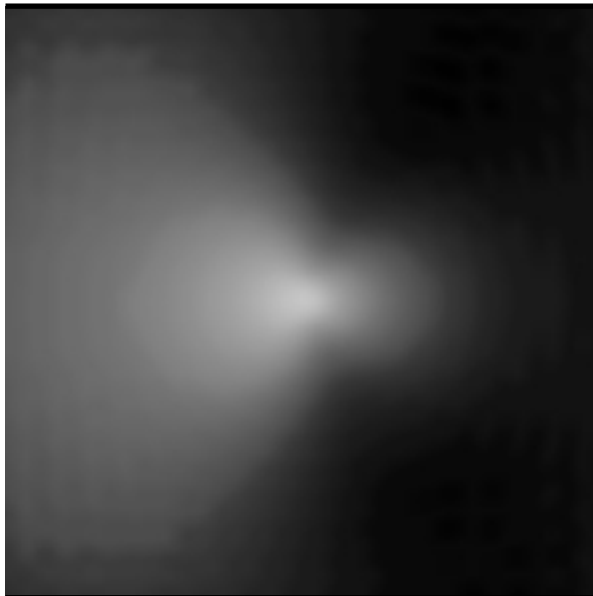


Figure 5. TSARLITE simulation of scattering from a dielectric cylinder, performed to validate the analytical approximation.

$$\sigma_{3Dqp} = \frac{2\ell^2 \sigma_{2Dqp}}{\lambda} \left| \frac{\sin(k\ell \sin \tau)}{k\ell \sin \tau} \right|^2,$$

where ℓ is the length of the structure, λ is the wavelength, and τ is the tilt angle of the structure measured from broadside incidence.

The comparison between σ_{HH} , σ_{VV} calculated from analytic approximation and σ_{3DHH} , σ_{3DVV} obtained from TSARLITE is shown in **Fig. 6**. The length and radius of the cylinder are 5λ and 0.1λ , respectively. The dielectric constant of the cylinder is $19 + i0.7$. The comparison shows good agreement between the analytic and TSARLITE results.

Figure 7 shows the HH and VV back-scattering radar cross-section of a cylindrical dielectric defect lying on top of the substrate as a function of the incident angle (measured from the vertical direction). The scattering returns include the direct scattering from the cylinder, and the phase interactions between the substrate and the cylinder. The length and radius of the cylinder are the same as in **Fig. 6**. The dielectric constant of the cylinder and substrate is $19 + i0.7$.

This analytic solution is indicative of the size/structure of the defect and will allow the experimental inspection to determine characteristics of the substrate anomalies.

Future Work

For the coming year, we will extend the models to include scattering from defects under multi-layer coatings. A combination of asymptotic/analytical

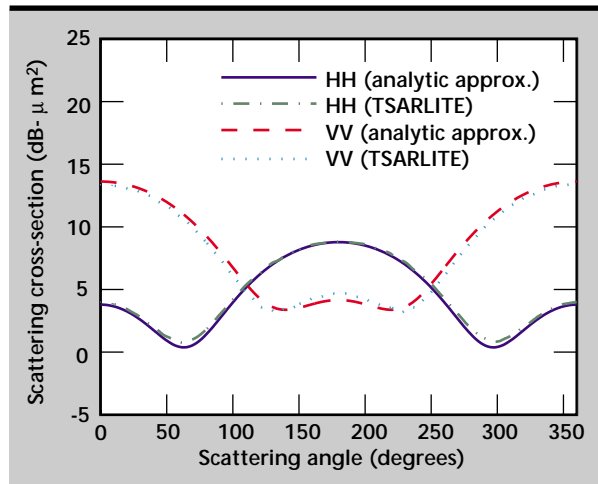


Figure 6. Scattering from a vertical dielectric cylinder as a function of the scattering angle on a cut-plane at some length along the cylinder. The length and radius of the cylinder are 5λ and 0.1λ , respectively. The dielectric constant of the cylinder is $19 + i0.7$.

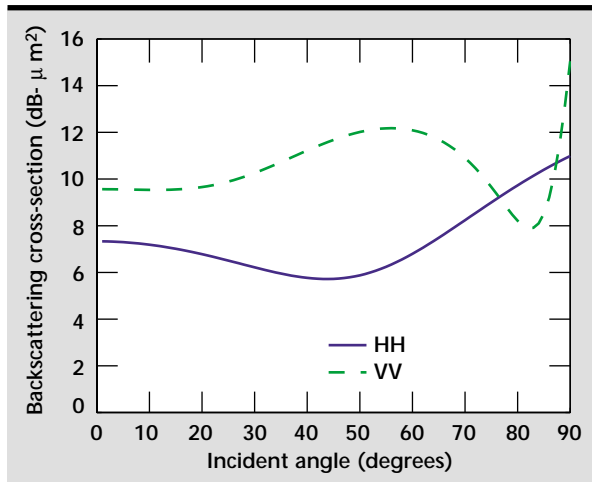


Figure 7. Back-scattering radar cross-section from a cylindrical dielectric defect lying on top of the substrate, as a function of the incident angle. The result takes into consideration the phase interactions between the cylinder and the substrate. The length and radius of the cylinder are 5λ and 0.1λ , respectively. The dielectric constant of the cylinder is $19 + i0.7$.

methods and numerical techniques will be used to calculate scattering from those defects. Numerical techniques will be used to validate scattering returns calculated with asymptotic/analytical methods. They will also be used in calculating scattering from defects with more complex shapes, and in those cases where the asymptotic/analytical methods are no longer valid.

At the end of the year, the scattering model will be extended to include scattering from defects under multi-layer coatings. The simulation results include scattering cross-section for detection of defects, as well as the scattered field. The latter couples into lithography printing simulation codes. Simulation programs will be benchmarked with experimental data.

Acknowledgment

The authors wish to thank M. Bujak for assistance with the TSARLITE results.

References

1. Vernon, S. P., D. R. Kania, P. A. Kearney, R. A. Levesque, A. V. Hayes, B. Druz, E. Osten, R. Rajan, and H. Hedge (1996), "Reticle Blanks for Extreme Ultraviolet Lithography: Ion Beam Sputter Deposition of Low Defect Density Mo/Si Multilayers," *OSA Topical Meeting on Extreme Ultraviolet Lithography*, Vol. 4, G. Kubiak and D. Kania, eds, pp. 44-48.
2. Kearney, P. A., C. E. Moore, S. I. Tan, S. P. Vernon, and R. A. Levesque (1997), "Mask Blanks for Extreme Ultraviolet Lithography: Ion Beam Sputter Deposition of Low Defect Density Mo/Si Multilayers," *Journal of Vacuum Science and Technology B*, Vol. 15, (6), pp. 2452-2454.
3. Lin, Y., and J. Bokor (1997), "Minimum Critical Defects in Extreme-Ultraviolet Lithography Masks," *Journal of Vacuum Science and Technology B*, Vol. 15, (6), pp. 2467-2470.
4. Ishimaru, A. (1991), *Electromagnetic Wave Propagation, Radiation, and Scattering*, Prentice Hall, Englewood Cliffs, New Jersey.
5. Kong, J. A. (1990), *Electromagnetic Wave Theory*, 2nd ed., John Wiley and Sons, New York, New York.
6. Ruck, G. T., D. E. Barrick, W. D. Stuart, and C. K. Krichbaum (1970), *Radar Cross Section Handbook*, Vol. 1, 2, Plenum Press, New York, New York.
7. Tsang, L., J. A. Kong, and R. T. Shin (1985), *Theory of Microwave Remote Sensing*, John Wiley and Sons, New York, New York.
8. Bouche, D., F. Molinet, and R. Mittra (1997), *Asymptotic Methods in Electromagnetics*, Springer-Verlag, New York, New York.
9. Karam, M. A., A. K. Fung, and Y. M. M. Antar (1988), "Electromagnetic Wave Scattering from Some Vegetation Samples," *IEEE Transactions on Geoscience and Remote Sensing*, November, Vol. 26, (6), pp. 799-808.
10. Le Vine, D. M., A. Schneider, R. H. Lang, and H. G. Carter (1985), "Scattering from Thin Dielectric Disks," *IEEE Transactions on Antennas and Propagation*, December, Vol. 33, (12), pp. 1410-1413.
11. Kallman, J. S., and R. J. Hawkins (1992), *TSARLITE and BEEMER: Tools for Integrated Optic Design*, Lawrence Livermore National Laboratory, Livermore, California (UCRL-JC-110403).
12. Skolnik, M. (1990), *Radar Handbook*, 2nd ed., Chapter 11, McGraw-Hill, New York, New York.

Nuclear and Electromagnetic Radiation Simulation Tools for Dual-Revalidation of the Stockpile

David J. Mayhall and Michael F. Bland

*Defense Sciences Engineering Division
Electronics Engineering*

We have obtained and installed three codes for the assessment of system-generated electromagnetic pulse effects for dual-revalidation of the stockpile. We have run these codes and have begun validation of them. The good agreement between results from the MEEC vacuum regime code and the MAFIA code for the case of low-emitted charge gives us confidence that the MEEC provides accurate results for non-space-charge-limited emission for simple internal geometries. Documents we have obtained show good agreement between MEEC simulations and experiments for low- and high-pressure cases using simple geometries.

Introduction

The goal of this project is to obtain, install, validate, use, and improve simulation software tools for predicting system-generated electromagnetic pulse (SGEMP) effects in the stockpile dual-revalidation program. SGEMP is the transient electromagnetic pulse created by electrons emitted by a system exposed to incident photons from large gamma fluences.

SGEMP can be external or internal. In the external case, the electromagnetic fields are produced on the outer surfaces of the system. In the internal case, the fields are produced within the system. SGEMP can cause upset, damage, and system failure due to large currents burning out components. The presence of trapped or evolved gasses around the system or inside cavities significantly modifies SGEMP. Experiments indicate that breakdown of the space charge layer occurs at low pressures, significantly increasing current flow. For this reason vacuum simulations are not sufficient to evaluate worst case threats.

Approach

Our approach to this project has been to obtain, install, run, and test the codes MEEC, MCNP, and CEPXS. We have also obtained a dedicated Pentium-class PC with a removable hard drive and a state-of-the-art FORTRAN compiler and development studio to run these codes. We have contracted to have the presently script-based MEEC code upgraded with a

GUI to make it much more user-friendly. In addition, we have compared results from the MEEC vacuum regime code with those from the TS3 electromagnetic particle-in-the-cell (EM-PIC) module of the MAFIA code.

MEEC is a set of 2- and 3-D EM-PIC codes for SGEMP in the vacuum, low-pressure, and atmospheric regimes. MCNP (Monte Carlo Neutron Photon) is a 3-D, time-dependent code for electron generation due to photon and neutron incidence and transport in materials. CEPXS solves the 1-D transport equation for coupled photon-electron cascades for energies greater than 1 keV. Since CEPXS is a deterministic, finite-difference code, it is less computationally intensive than a Monte Carlo code and will allow more efficient calculation of generated electron fluences for input to the MEEC code.

Validation

As a validation of the MEEC vacuum regime code, we have run a test problem consisting of an electrically perfectly conducting right rectangular solid within an electrically perfectly conducting right rectangular container. Two values of electron charge emission from the top of the internal solid, 6.33×10^{-8} C and 6.33×10^{-6} C have been simulated. We have also run the same problem with a similar, but slightly different, computational grid with MAFIA TS3.

The MAFIA geometry is shown in **Fig. 1**. Since symmetry is assumed about the z-axis, the MAFIA calculation is confined to the first quadrant of the

z-projected xy plane (positive x and positive y). The xz and yz planes are symmetry planes. The domain of the inner solid is $0 \leq x \leq 0.5$ m, $0 \leq y \leq 0.5$ m, -0.5 m $\leq z \leq 0.5$ m. The domain of the computational space within the outer solid is $0 \leq x \leq 2$ m, $0 \leq y \leq 2$ m, -2 m $\leq z \leq 2$ m. Part of the spatially uniform MAFIA grid is shown on the surfaces of the inner solid.

The time history of the emission is triangular, with a linear rise from 0 to 10 ns, followed by a linear fall from 10 ns to 20 ns to a null value. The angular distribution of emitted particles about the z-axis in the plane parallel to the xy plane is uniform. The angular distribution of emitted particles, as measured from 0 to 90° from the positive z-axis, is parabolic, with minima at 0 and 90° and a maximum at 45°. The spatial distributions of emitted particles are uniform in the x and y directions. The distribution of emitted particles with kinetic energy is half-parabolic with the maximum at 1 keV, the minimum at 24 keV, and a maximum to minimum

ratio of 10. The spatial state of the electron macroparticles emitted from the top surface of the inner solid at 21.6 ns, for 6.33×10^{-8} C of emitted negative charge, is shown in **Fig. 1**.

The MAFIA calculation uses one randomly emitting area. The MEEC calculation uses five emitting areas of extent, 0.1 m \times 0.5 m, in the x and y directions. Each calculation uses 4000 macroparticles. The MEEC grid is nonuniform, with finer spacings near the interfaces of the inner solid with the surrounding vacuum space. In both calculations, the electrons incident on the inner surfaces of the outer container and inner solid are totally absorbed. Because of restrictions on image plane locations, the MEEC calculation is performed in the third quadrant of the z-projected xy plane (negative x and negative y).

Figure 2 shows the spatial state of the particles for the MAFIA calculation at 21.6 ns for 6.33×10^{-6} C of emitted charge. For this case, fewer particles are

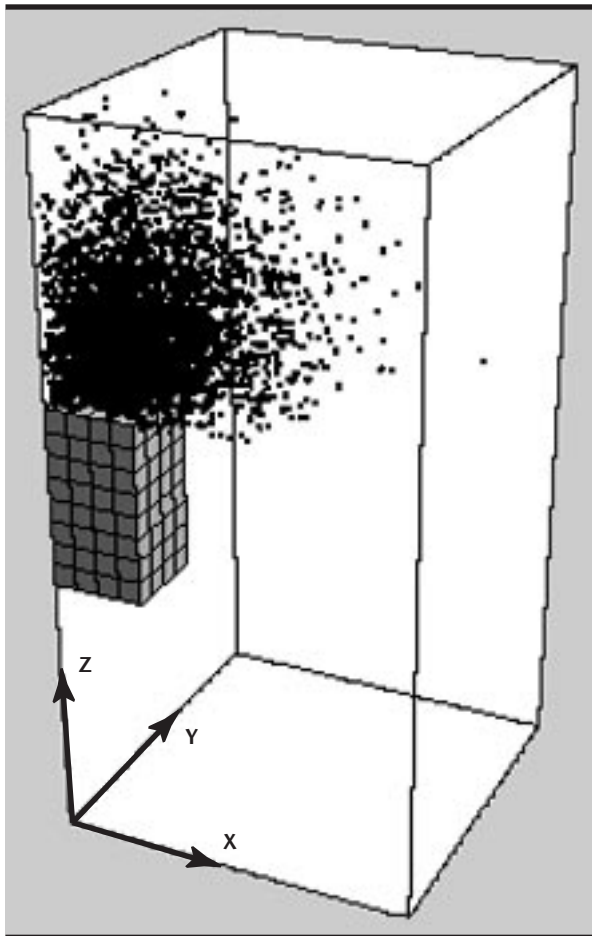


Figure 1. MAFIA problem geometry and the electron macroparticles at 21.6 ns for 6.33×10^{-8} C of emitted charge.

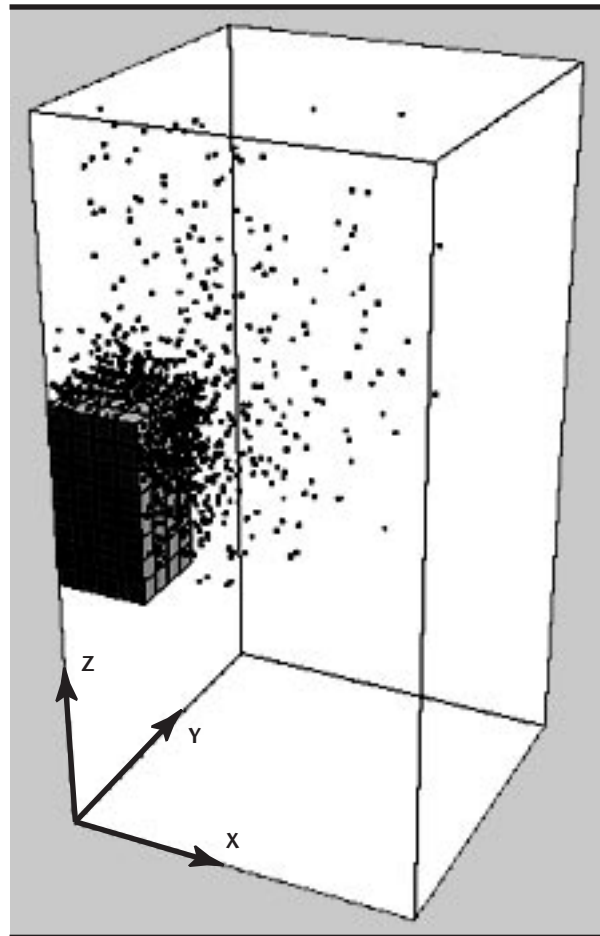


Figure 2. The MAFIA electron macroparticles at 21.6 ns for 6.33×10^{-6} C of emitted charge.

situated within the bulk of the space between the two solids. More are confined near the surface of the inner solid. Space-charge-limited emission is thus evident in this second calculation. For this amount of emitted charge, many of the emitted particles remain close to the inner solid, move down its sides, and then move across its bottom at $z = -0.5$ m.

Figure 3 shows a comparison of MEEC and MAFIA E_z -field waveforms at two nearby points above the emitting top of the solid on the positive z -axis. The MEEC electric field point is at (0, 0, 0.81 m); the MAFIA point is at (0, 0, 0.8125 m). The MAFIA result is noisier and rises to a higher corresponding positive value than does the MEEC result. Some of the MAFIA noise may be due to the single emitter used, as opposed to the five emitters used in the MEEC calculation. The discrepancy in the values after the negative peaks may be due to differences in the two grids.

Figure 4 shows a comparison of MEEC and MAFIA H_x waveforms at two more nearby points. The MEEC field component is calculated at (0, -0.425 m, 0.525 m); the MAFIA component at (0, 0.4375 m, 0.5625 m). These points lie on the $x = 0$ symmetry plane, slightly above the emitting surface near the outer edges of the inner solid. Because the initial axial current density in the space above the inner solid is in the negative z direction, the right-hand rule gives a negative H_x component for the MEEC simulation in the third quadrant and a positive one for the MAFIA simulation in the first quadrant.

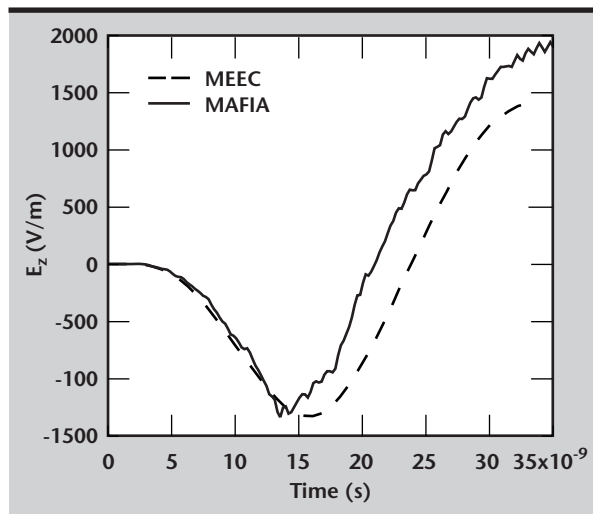


Figure 3. Comparison of MEEC and MAFIA E_z components for 6.33×10^{-8} C of emitted charge.

For ease of comparison, we have inverted the MAFIA result in **Fig. 4**. The MAFIA point is slightly closer to a top edge of the inner solid (1.25 cm) and somewhat higher above the emitting surface (3.75 cm) in the positive z direction. The MAFIA waveform is thus expected to be delayed with respect to the MEEC waveform and to be somewhat lower in amplitude. **Figure 4** shows the MAFIA result to be delayed by about 1 ns during the fall toward the negative peaks. An apparent smoothed value of the MAFIA negative peak is ~ -2.5 A/m, which is slightly lower in magnitude than the MEEC negative peak of ~ -2.55 A/m. The MAFIA result is once again more noisy than the MEEC result.

Greater differences between the results of the two codes occur for 6×10^{-6} C of emitted charge. Although the shapes of the waveforms are generally similar, the MAFIA peaks are usually greater and delayed. Some of the MAFIA E_z waveforms show strong late time (>29 ns) discrepancies. The MAFIA waveforms, especially for the magnetic field and current density components, are also noisier. The reasons for these discrepancies are not yet known. Some possibilities include computational differences and object description differences. However, because a run with a more refined MEEC grid produced results for the high-charge-emission case similar to those for the initial MEEC grid, we believe that MEEC results are good for space-charge-limited emission in simple geometries.

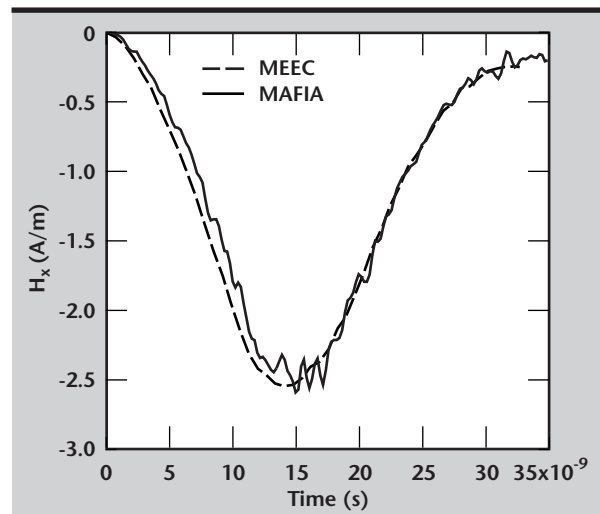



Figure 4. Comparison of MEEC and MAFIA H_x components for 6.33×10^{-8} C of emitted charge.

Future Work

We plan to further investigate the accuracy of the MEEC vacuum and the MAFIA codes for cases of space-charge-limited emission. Benchmarking against standard test problems or accepted analytical solutions is desired. We plan to validate the MEEC

low- and atmospheric-pressure codes in simple geometries. When available, we plan to test MEEC with the new GUI capability. To support the W76 revalidation we plan to model the W76 weapon electronic and radiation case geometry. Simulations of cable-induced SGEMP currents will be calculated and compared to test data. 



Self-Effects in Expanding Electron Beam Plasmas

Manuel Garcia

Laser Engineering Division

Electronics Engineering

An analytical model of plasma flow from metal plates hit by intense, pulsed, electron beams aims to bridge the gap between radiation-hydrodynamics simulations and experiments in the Advanced Hydrotest Facility at Lawrence Livermore National Laboratory (LLNL). This model also helps quantify the self-effect of the electron beam penetrating the target material, which is not addressed by simulations.

Introduction

When a pulsed electron beam hits a metal plate with sufficient energy, a volume of the metal becomes ionized fluid that subsequently sprays out of the plate. Does this counterflow disrupt the tight focus of the initial electron bunch, or later pulses in a train? This work aims to model the spatial distribution of plasma speed, density, degree of ionization, and magnetization to address this question.

Progress

Numerical simulations of target flows are very accurate for the initial 2 μ s. Beyond this point, the relative density is quite low, precision drops, and calculation times are long. The initial solid-density, several-eV plasma expands to 1 cm and 10^{-4} relative density by 2 μ s. Yet, a Faraday cup detector located 25 cm from the target at LLNL's experimental test accelerator (ETA-II) facility, observes the flow after an expansion of 50 μ s. In addition, the Faraday cups at ETA-II are immersed in the focusing magnetic field of the accelerator. There is a wide gap between what the Faraday cups see and what the simulations provide. An analytical model of the plasma flow helps to connect the experimental observations with the simulations of early times.

The expansion of the target plasma into the vacuum of the accelerator is so rapid that the ionized portion of the flow departs from local thermodynamic equilibrium downstream. In fact, we found that when the temperature (in eV) in a parcel of fluid drops below $V_1 \times [(2\gamma - 2)/(9\gamma + 15)]$, where V_1 is the ionization potential of the target metal (for example, 7.8 eV for tantalum), and γ is the ratio of

specific heats, then the fractional ionization and electron temperature in that parcel remain fixed during its subsequent expansion. This effect is called freezing. For atoms, $\gamma = 5/3$ and the freezing temperature as defined here is $V_1/22.5$.^{1,2}

An electron beam penetrating the target and its plasma will experience a radical change in the balance it had in vacuum, between the pinching force of its own azimuthal magnetic field and the disruptive electric field of its negative space charge.

The effects are as follows: 1) the target plasma cancels the electric field of the beam by an overwhelming charge density; 2) the plasma conductivity creates an internal eddy current to counter the magnetization introduced by the transit of relativistic electrons; and 3) the plasma magnetization changes as electron beam heating alters the density gradient and the magnitude of the conductivity.

This combination of effects could cause either pinching or expansion of a penetrating beam (aside from scattering) at different times during its transit. References 3 and 4 initiate the exploration of thermally-generated magnetization, while References 5, 6 and 7 are guides to a deeper analysis.

Figures 1, 2, and 3 show a tantalum flow generated by depositing an impulse of 5 J within a diameter of 0.8 mm and depth of 50 μ m. The initial temperature of this plasma was 9 eV.

Figures 1, 2, and 3 also show profiles of the heavy particle density, fluid and electron temperatures, and electron density, respectively, outside the plate at 300 ns. The leading edge of the flow has reached 1.2 mm, the source volume within the plate has cooled to less than 1 eV, and the source plasma has 2% of its original density.

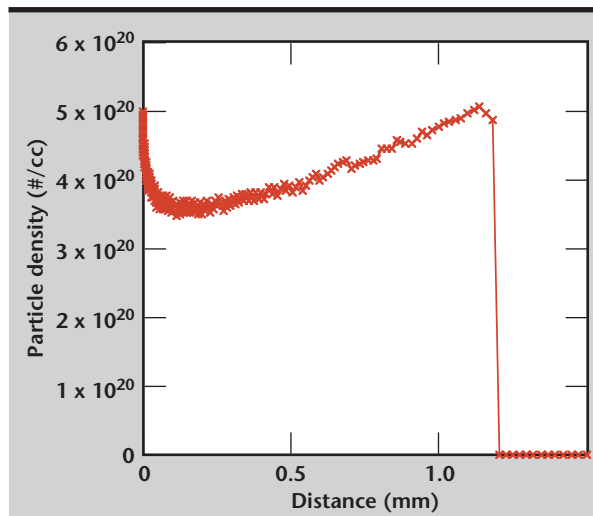


Figure 1. Particle density at 300 ns.

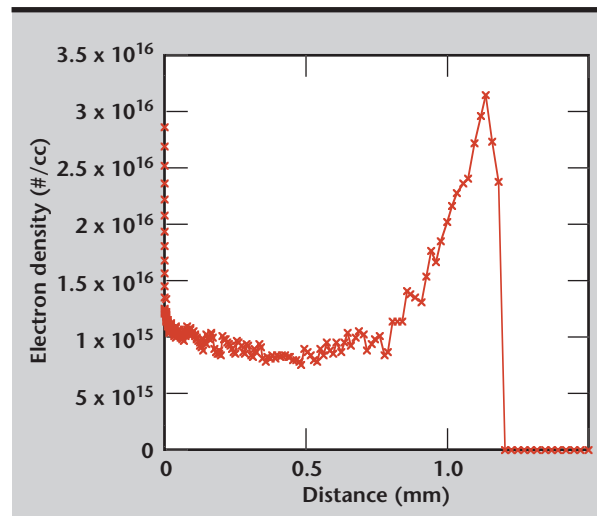


Figure 3. Electron density after 300 ns.

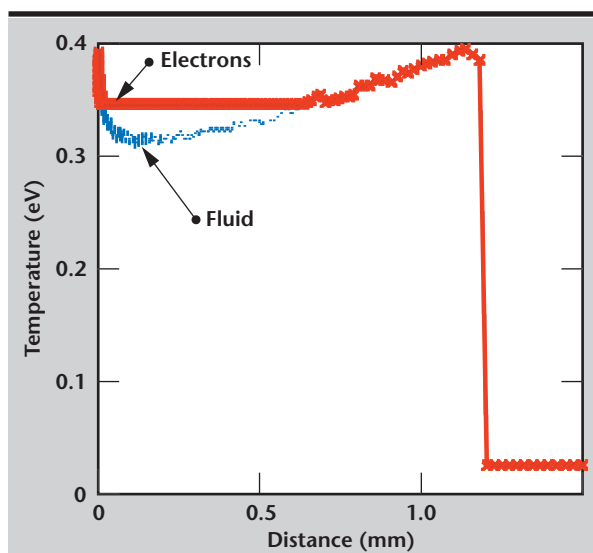


Figure 2. Electron and fluid temperatures after 300 ns.

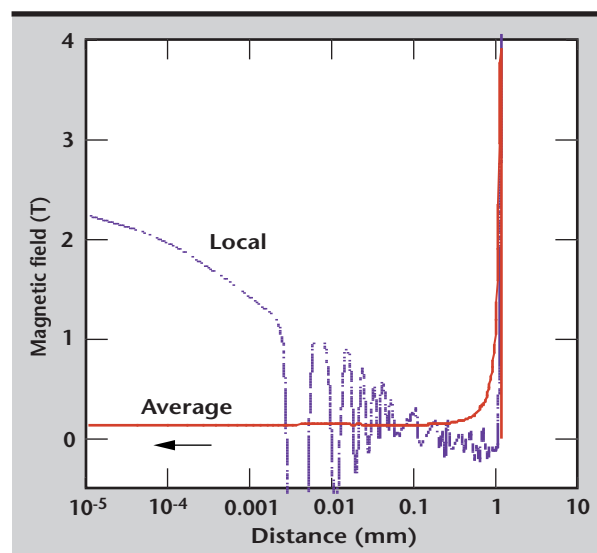


Figure 4. Local and average magnetic field along the flow.

The freezing effect is just visible in **Fig. 2**. Flow later in time and downstream of this point will have a frozen ionization fraction (2×10^{-5}) and electron temperature (0.35 eV). An ideal probe at 25 cm from the plate would observe the arrival of plasma at 51 μ s, with an atom density of $2 \times 10^{16} \text{ cm}^{-3}$, an electron density of $4 \times 10^{11} \text{ cm}^{-3}$, and a decrease to one quarter of these peak values by 140 μ s.


Figure 4 shows profiles of the azimuthal magnetic field (tesla) that arises within the tantalum cloud, just described, on being penetrated and heated by an electron beam pulse of 1000 A within a 0.8-mm diameter for 30 ns. One profile in **Fig. 4** is of local magnetic field values, the other is a running average from the leading edge of the flow.

The magnetic field is generated thermally by the nonalignment of the gradients of electron temperature and density.^{5,6} This thermally-generated magnetic field has the opposite polarity to the self-field of the electron beam (which is -0.5 T in this example). Large local values arise where the density gradients are large: at the leading edge, and at the exit of the plate. In this example, the average thermally-generated field does not cause the electron beam to diverge because high local fields occur only in narrow zones.

Future Work

Current work aims to improve the estimates of thermally-generated magnetic fields by refining the many approximations required to describe such intricate physics in an analytical model. In particular, a realistic conductivity model $\sigma(T, N)^8$ and a more accurate dynamic heating model for improved density gradients are the focus of effort. Also, comparison to the Faraday cup and interferometer data from ETA-II can help improve both model and experiment.

References

1. Garcia, M. (1997), "Splash flow from a metal plate hit by an electron beam pulse," Lawrence Livermore National Laboratory, Livermore, California (UCRL-ID-128660).
2. Garcia, M. (1997), "Frozen plasma within the flow from a metal plate hit by an electron beam pulse," Lawrence Livermore National Laboratory, Livermore, California (UCRL-ID-126296).
3. Garcia, M. (1998), "On electromagnetic acceleration of material from a plate hit by a pulsed electron beam," Lawrence Livermore National Laboratory, Livermore, California (UCRL-JC-130448).
4. Garcia, M. (1998), "Electron beam expansion by target heating," Lawrence Livermore National Laboratory, Livermore, California (UCRL-ID-131291).
5. Haase, R. (1969), *Thermodynamics of Irreversible Processes*, Addison-Wesley Publishing Company, London.
6. Haines, M. G. (1997), "Saturation mechanisms for the generated magnetic field in a nonuniform laser-matter irradiation," *Phys. Rev. Lett.* **78** (2), p. 254.
7. Craxton, R. S., and M. G. Haines (1978), " $\mathbf{j} \times \mathbf{B}$ acceleration of fast ions in laser-target interactions," *Plasma Physics*, Vol. **20**, Pergamon Press Ltd., Northern Ireland, pp. 487–502.
8. Redmer, R. (1998), "Electrical conductivity of dense metal plasmas," submitted to *Phys. Rev. E*, **6**. 

Pump-Induced Wavefront Distortion in Prototypical NIF and LMJ Amplifiers

Mark D. Rotter

*Laser Engineering Division
Electronics Engineering*

**Kenneth S. Jancaitis, Christopher D. Marshall, Luis E. Zapata,
and Alvin C. Erlandson**

*Laser Science and Technology
Laser Programs*

Geoffroy LeTouze' and Stephane Seznec

*Commissariat à l'Energie Atomique
Villeneuve, St. Georges, France*

In large-aperture laser amplifiers such as those envisioned for the National Ignition Facility (NIF) and Laser Megajoules (LMJ) lasers, the geometry is such that the front and back faces of the laser slab are heated unevenly by the pump process. This uneven heating results in a mechanical deformation of the laser slab and consequent internal stresses. The deformation and stresses, along with a temperature-dependent refractive index variation, result in phase variations across the laser beam, so-called pump-induced wavefront distortions. These phase variations lead to beam steering which may affect frequency conversion as well as energy-on-target. We have developed a model that allows us to estimate the pump-induced wavefront distortion for a given amplifier configuration as well as the spatially-resolved depolarization. The model is compared with experiments taken in our amplifier development laboratory (AMPLAB).

Introduction

We are currently developing large-aperture amplifiers for the National Ignition Facility (NIF) and Laser Megajoules (LMJ) lasers at Lawrence Livermore National Laboratory (LLNL). These multi-segment amplifiers are the flashlamp-pumped, Nd:Glass type, and are designed to propagate a nominally 36-cm-square beam. The apertures within a particular amplifier bundle are arranged in a four-high-by-two-wide configuration and use two side flashlamp arrays and a central flashlamp array for pumping (**Fig. 1**).

As shown in **Fig. 1**, the slabs are oriented at Brewster's angle and are pumped on both sides by arrays of flashlamps, denoted as central arrays (lamps that pump both slabs) and side arrays. The geometry of the amplifier results in one end of the slab being situated closer to the lamps than the other. Consequently, the amount of heat deposited in the slab (primarily from the quantum defect of the

broad-band pump light) is uneven front-to-back as well as side-to-side.

This uneven pumping results in a warping of the laser slab, indicated by the dashed lines in **Fig. 1**. An initially plane wavefront incident on such a slab will not remain planar upon exit. Ultimately, wavefront distortion is due to differences in the optical path (defined as the refractive index times the physical path length) at one point in the aperture vs that at another. We have seen one source of these optical path differences (OPDs), namely, the mechanical distortion of the laser slab. There is another source of OPD: the spatially-varying refractive index to which temperature and stress contribute.

We have developed a model that takes all of the above effects into account, and that allows us to predict the pump-induced wavefront distortion for these large-aperture amplifiers. In this report, we describe various aspects of the model and present comparisons between the model and experimental data taken on AMPLAB, our amplifier test laboratory.

Progress

Pump-Induced Wavefront-Distortion Model

Description of Model. As mentioned in the introduction, the non-uniform deposition of heat in the laser slab is responsible for slab distortions and aberrations of any plane wavefront incident on it. Thus, the fundamental ideas may be summarized as follows: the non-uniform heat deposition results in a distortion of the laser slab and accompanying stresses. The distortion of the laser slab, in conjunction with the temperature and stress-induced refractive index variations result in the OPDs and consequent wavefront distortion.

To calculate the various effects listed above, we use a suite of computer codes: TOPAZ3D¹ to calculate the temperature distribution within the laser slab, NIKE3D² to calculate the displacements and stresses from the temperature field given by TOPAZ3D, and OPL, which calculates the OPDs, given the results from NIKE3D. The codes NIKE3D and TOPAZ3D are 3-D finite element analysis codes which have been in use at LLNL for more than ten years. The optics code OPL is an in-house code based on the BREW code.³

Determination of Temperature. The first step in calculating the wavefront distortion is to determine the temperature distribution within the laser slab. To do this, we need to specify the thermal source function as a function of position and time. In general, this thermal source function is an arbitrary function of position and time. For purposes of this model, however, we have assumed a separable source function, that is:

$$Q(x, y, z, t) = As(x) [g_0(y) f(z)]$$

$$+ g_h(y) f(h - z)] u(t) + Q_{ec} , \quad (1)$$

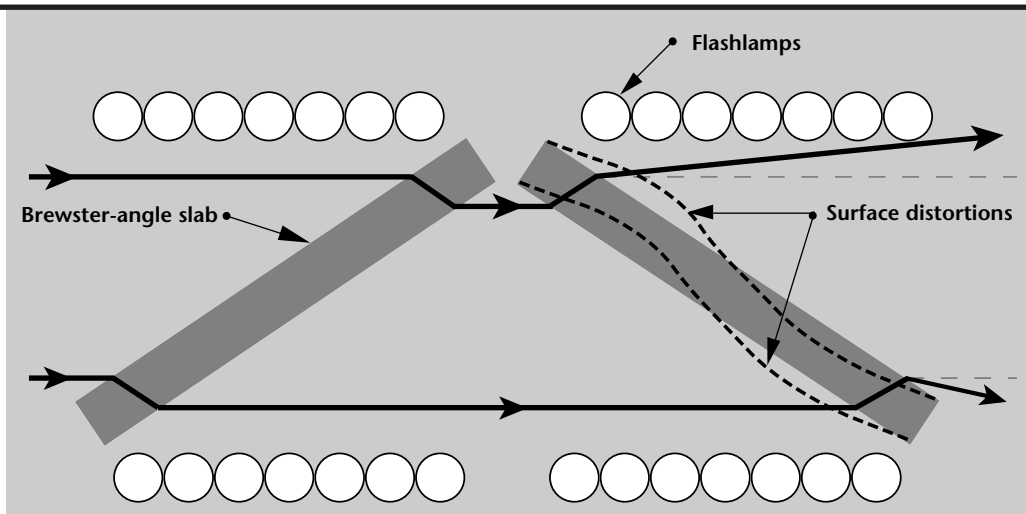
where $s(x)$ denotes the vertical variation of the pump profile; $g_{0,h}(y)$ denotes the horizontal variation of the pump profile at $z = 0, h$; $f(z)$ denotes the pump profile through the thickness of the slab; and Q_{ec} is the thermal source term for the edge cladding. The units for this source function are W/cm.³ In Eq. 1, h is the thickness of the slab and A is a constant multiplier. Each of these terms will now be described.

In the multi-segment amplifiers envisioned for use in the NIF, there is strong vertical symmetry. The flashlamps are oriented vertically, and there are silver-coated metal reflectors at the top and bottom of the pump cavity. As a result, we have taken the function $s(x)$ to be a constant. In reality, the reflectors are not perfect, and so there is a slight roll-off in pump light at the extreme top and bottom of the pump cavity. We have found that this is a small effect insofar as calculating the pump-induced wavefront distortion is concerned, and so have elected to keep $s(x)$ a constant.

As mentioned above, the geometry of the pump cavity results in a roll-off of the pump radiation from one side of the aperture to the other. We used our 2-D+ ray-trace code⁴ to calculate the distribution of pump light across the laser slab. An example of the functions so obtained is shown in Fig. 2. Because these functions can be rather convoluted, no curve fitting is done. Instead, TOPAZ3D uses $g(y)$ as is, and interpolates to return values for Q for any y .

The thermal energy deposition through the thickness of the slab is given by the function $f(z)$. This function is calculated using our Lamp Model code,⁵ which calculates the energy deposition profile as a

Figure 1. Plan view of multi-segment amplifier showing geometry of Brewster-angle laser slabs. Surface distortions (greatly exaggerated) are caused by uneven pumping.



function of slab geometry, doping density, and lamp operating level. The profile so obtained is a spectrally-integrated thermal energy deposition profile, which we then fit to a double exponential:

$$f(z) \propto e^{-\mu_1 z} + c e^{-\mu_2 z}, \quad (2)$$

where μ_1 , μ_2 , and c are the fit coefficients. A plot of the energy deposition profile and the corresponding fit is shown in **Fig. 3**.

To describe the temporal behavior of the pump pulse, we use an analytic expression for $u(t)$. We first need to describe the temporal behavior of the electrical input power to the lamp. Since the flashlamp is a nonlinear circuit element, the actual pulse shape is described by a nonlinear differential equation.⁶ We have found, however, that an excellent approximation to the shape is given by the function:

$$p(t) \propto t \exp\left[-(t - a)^2 / \tau^2\right], \quad (3)$$

where a and τ are fit parameters. A plot of the electrical input power as determined from a numerical integration of the circuit equation and the approximation given by **Eq. 3** is shown in **Fig. 4**. With the electrical input power so determined, we then calculate the optical output power from the flashlamp. The output power, $u(t)$, may be calculated from the following equation:⁷

$$du/dt = [\eta(u)p(t) - u(t)]/\tau_R, \quad (4)$$

where $\eta(u)$ is the instantaneous radiant efficiency of the flashlamp (corrected for arc-expansion effects), and τ_R is radiative recombination time of the plasma ($\sim 30 \mu\text{s}$). Since $\eta(u)$ is a nonlinear function of u , **Eq. 4** is likewise nonlinear.⁷ We have found, however, that an excellent approximation is to take $\eta(u)$ to be a constant, parametric in the pulsewidth:

$$\eta(u) = .653 + 2.33 \times 10^{-4} \tau_{10} \quad (5)$$

$$200 < \tau_{10} < 500 \mu\text{s},$$

where τ_{10} is the full-width tenth-maximum time of the electrical input power pulse. In **Fig. 5** we show the comparison between the numerical solution to **Eq. 4** and the solution using the approximation given by **Eq. 5**. We see that over the time range specified, the agreement is quite good. Using **Eqs. 3** to **5**, an analytic expression for $u(t)$ may be obtained.

At this point, we do not have a good *ab initio* calculation for the heat deposited in the laser slab. Present calculations disagree with measurements by

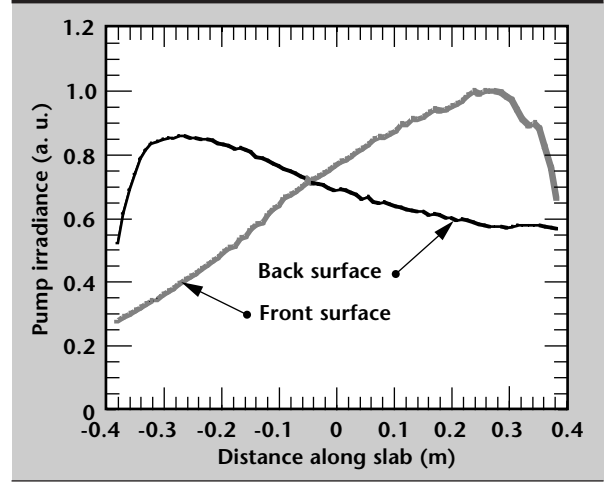


Figure 2. Pump irradiance profiles—AMPLAB diamond configuration.

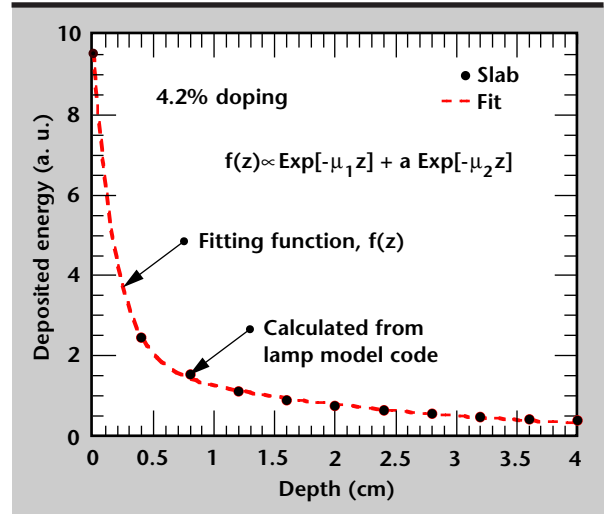


Figure 3. Energy deposition profile through slab and fit.

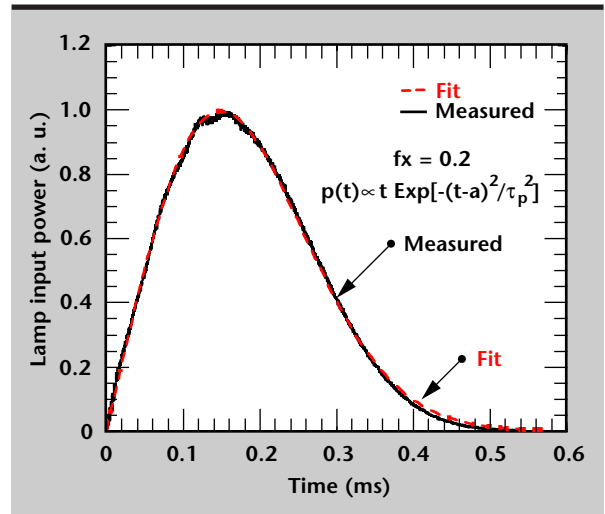


Figure 4. Measured electrical input power to lamp and fit.

about a factor of two. The cause of this discrepancy is currently not known. Thus, we have included a scale factor, A in **Eq. 1**, to scale our results to experimental measurements. It should be pointed out that once this factor is determined (for example, from AMPLAB measurements), then that factor is held constant for all succeeding calculations.

The last term in **Eq. 1** represents the heat deposited into the edge claddings that surround the laser glass. This term, Q_{ec} , is composed of two parts:

$$Q_{ec} = Q_{ec,pump} + Q_{ec,ASE} , \quad (6)$$

where $Q_{ec,pump}$ and $Q_{ec,ASE}$ represent the heat deposited into the edge claddings by the pump and by amplified spontaneous emission (ASE), respectively. The source term is broken up in such a manner because the time dependence of the two parts is different. For $Q_{ec,pump}$ the time dependence is just $u(t)$, described above. For $Q_{ec,ASE}$ the time dependence is different due to the fact that the peak of the ASE pulse occurs at the time of peak gain, not at the time of peak pump power. The relationship between the output power from the flashlamp and the stored energy density, $\rho(t)$, is given in Reference 7. Once $\rho(t)$ is determined, it may be shown that the time dependence of the ASE, $\phi(t)$, may be written as:⁸

$$\phi(t) \propto \rho(t) \left[a + b \left\{ \exp[\rho(t)] - 1 \right\} \right] , \quad (7)$$

where a and b are constants. With **Eq. 7** describing the time dependence of the ASE, we then have, for example, for the edge cladding at $x = \text{constant}$:

$$Q_{ec,ASE} \propto \phi(t) \beta \Gamma e^{-\beta x} , \quad (8)$$

where β is the edge-cladding absorption coefficient, and Γ is the incident fluence. At present, we do not have an accurate *ab initio* calculation of the ASE fluence on the edge cladding. However, based on measurements with the Beamlet laser, we estimate a fluence of 4 J/cm² for ASE and another 2.5 J/cm² due to the pump light.

Equations 1 to 8 are used in TOPAZ3D to determine the temperature distribution in the laser slab. Due to the shortness of the pump pulse (a few hundred μ s), adiabatic boundary conditions are used on all faces of the slab. The result of this calculation is used in the code NIKE3D to calculate the displacements and stresses, as described in the next section.

Determination of Displacements and Stresses.

As mentioned above, we use the temperature distribution in the slab to calculate the displacements and stresses. Since the displacements are very small (on the order of 1 μ m), we are in the linear elastic regime and the problem is a standard one in thermo-elasticity. Consequently, we use a thermo-elastic material model and specify Poisson's Ratio, Young's Modulus and the thermal expansion coefficient.⁹ These parameters are taken to be constants, independent of temperature, insofar as the maximum temperature rise is on the order of 1 °C.

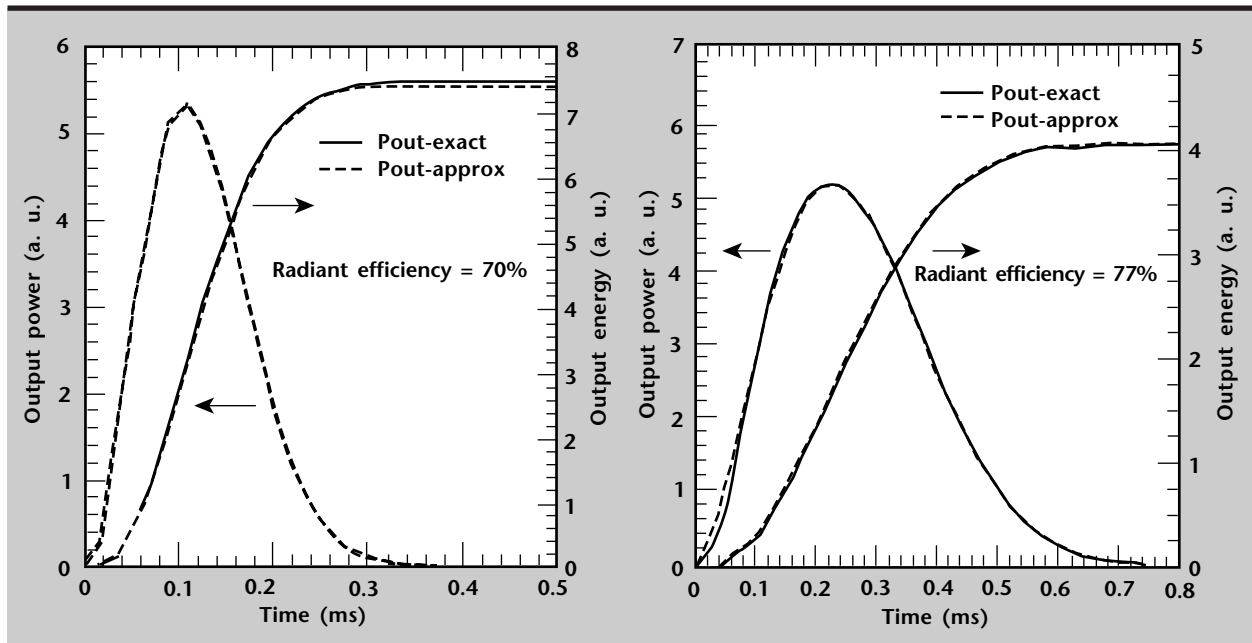


Figure 5. Comparison of exact and approximate solutions to flashlamp output equation.

At this point in the calculation, the mechanical boundary conditions for the slab are specified. In reality, the slab sits on a Marcel spring—a sinusoidally varying metal strip. While the capability exists to model the spring as it actually exists, we have found that a satisfactory substitution is to have the slab sit on a region of metal one element thick. The nodes in the glass material are joined to the nodes in the metal so no slipping can occur. The bottom of the metal region is simply supported, and we also fix the displacements at two additional corners to eliminate rigid-body motion. The rest of the slab surfaces are assumed to be free.

NIKE3D calculates the displacements and stresses as a function of time during the course of the pump pulse. Typically, the code is run up to the time of peak gain as the wavefront distortion at that time is what is usually requested. However, it is a simple matter to run the code for times longer than the time of peak gain to compare with experiments.

Determination of OPDs. The last part of the calculation involves computing the OPDs through the laser slab. For this, we use our in-house code OPL. The optical path length of a ray through the slab may be written as:

$$\text{OPL} = \int n(x, y, z) ds, \quad (9)$$

where n is the (spatially-varying) refractive index and s is the distance along the ray path. There are two main sources of OPD in the laser slab: 1) variations in path length caused by mechanical motion of the slab, and 2) variations in path length caused by refractive index changes.

The variations in path length caused by mechanical motion of the slab are due to the spatially-varying displacements calculated in NIKE3D; that is, a point x, y, z on the slab is translated to:

$$\begin{aligned} x &\rightarrow x + u(x, y, z, t) \\ y &\rightarrow y + v(x, y, z, t) \\ z &\rightarrow z + w(x, y, z, t). \end{aligned} \quad (10)$$

We take two effects into account to calculate the spatially-varying refractive index: 1) the variation of refractive index with temperature, and 2) the variation of refractive index with stress (stress-optic effect), that is:

$$\begin{aligned} n(x, y, z) &= n_0 + (dn/dT)\Delta T(x, y, z) \\ &+ (dn/d\sigma)\Delta\sigma(x, y, z), \end{aligned} \quad (11)$$

where n_0 is the isotropic refractive index, dn/dT denotes the change of refractive index with temperature, and we have symbolically written the change in refractive index due to stress as $dn/d\sigma$.

Note that in general, ΔT and $\Delta\sigma$ are functions of time. However, for the purposes of calculating the OPD, we select one point in time for the calculation. This is permissible since the time duration of the laser pulse is at most 20 ns. On this time scale, all thermal and mechanical motion is frozen.

The sequence of events in calculating the OPD is as follows. The OPL code reads in the finite-element geometry from the NIKE3D plot file. We then go through the mesh and break up each finite-element “brick” into six four-node tetrahedra and generate a connectivity matrix for these tetrahedra. We then use **Eq. 11** to calculate the refractive index at each node in the mesh. Within each tetrahedra, we linearize the refractive index:

$$n(x, y, z) = a + bx + cy + dz. \quad (12)$$

The four unknowns in **Eq. 12** are uniquely determined by the values of the refractive index at the four nodes of a given tetrahedron. With the refractive index linearized as in **Eq. 12**, we can then analytically solve the Eikonal equation¹⁰ for the ray path within a tetrahedron:

$$\frac{d}{ds} \left(n \frac{d\mathbf{r}}{ds} \right) = \nabla n, \quad (13)$$

where s is the distance along the ray path and \mathbf{r} is the position vector of the ray. The connectivity matrix helps us determine which tetrahedron the ray will enter, and consequently at which nodes to evaluate the refractive index to calculate the unknowns in **Eq. 12**. We then track the ray as it propagates through all the tetrahedra, all the while accumulating the distance that the ray propagates.

In addition to calculating the OPD for the ray, we can also calculate the depolarization a ray experiences as it propagates through the optic. We do this by assuming each tetrahedron acts as a linear retarder, and calculate the Jones matrix¹¹ for each tetrahedron. The final amount of retardation (and hence depolarization) is given by the product of all the individual Jones matrices for a given ray path.

A typical result from this calculation is shown in **Fig. 6**. The calculation was performed for the AMPLAB amplifier in the diamond configuration. In **Fig. 6a** we show the OPD for all effects (displacement, temperature, and stress) combined. It is often

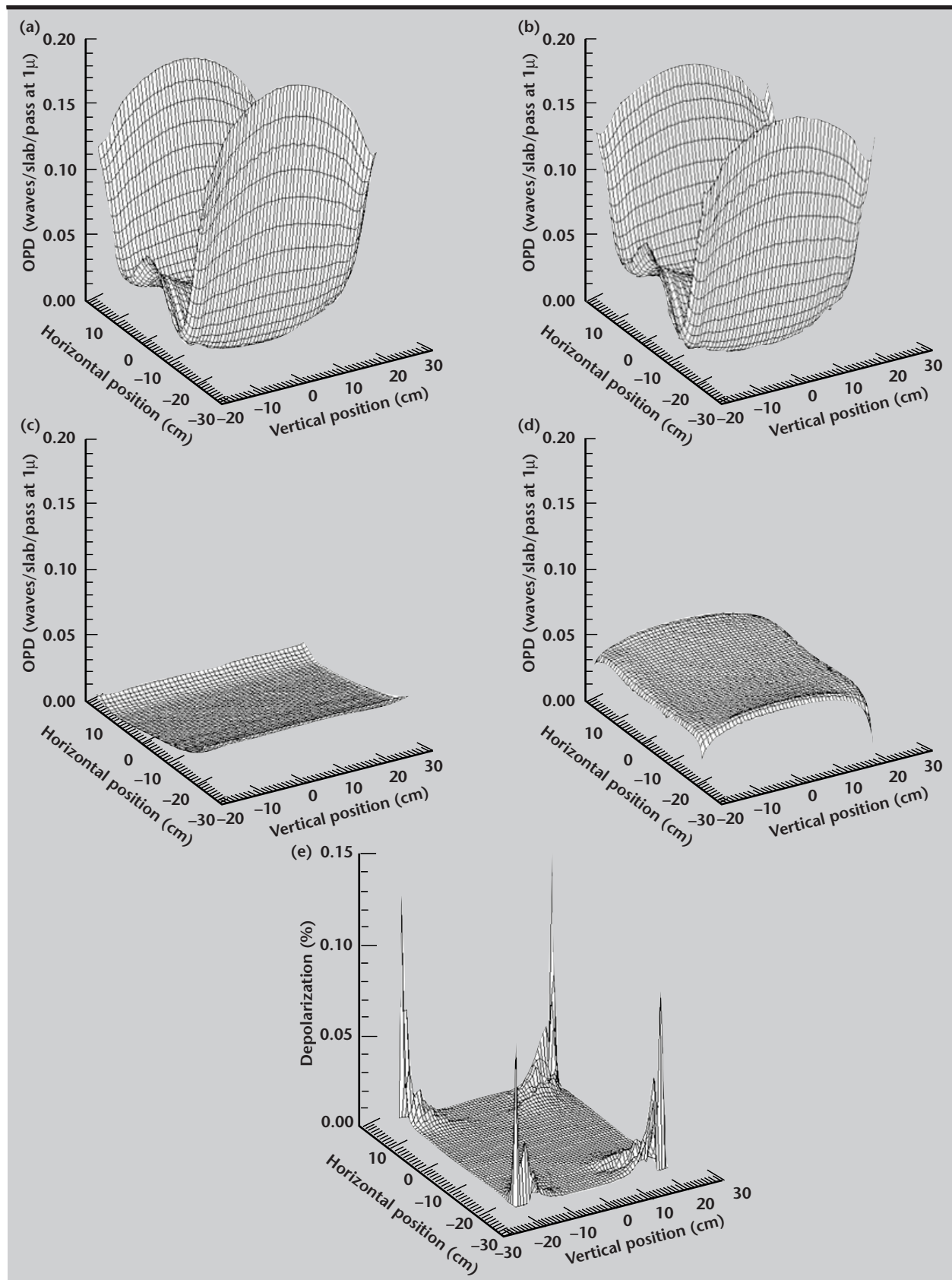


Figure 6. OPD calculated for the AMPLAB diamond configuration, $f_x = 0.2$: (a) all effects; (b) displacement effects only; (c) dn/dT effects only; (d) stress effects only; and (e) depolarization.

useful to examine each component individually, and this is done in **Figs. 6b, c, and d**. In **Fig. 6b** we show the contribution to the OPD due solely to mechanical deformation.

Comparison with **Fig. 6a** shows that for AMPLAB, the wavefront distortion is due mainly to the mechanical deformation of the slab. In **Figs. 6c and d** we show the contribution to the OPD from temperature and stress effects on the refractive index. As may be seen, these effects play a relatively minor role in determining the overall OPD. Finally, in **Fig. 6e** we show the P-to-S depolarization.

As expected, the greatest amount of depolarization occurs in the corners, where the two pieces of edge cladding meet. It is there where the greatest amount of stress occurs. Nevertheless, the overall amount of depolarization is small, well within its specification of 0.05% averaged over the aperture.

Error Analysis. In this section, we estimate the error in our calculation of the OPD. For the amplifier conditions considered in this report, the dominant contribution to the OPD is the mechanical deformation of the laser slab (see **Figs. 6a and b**). Consequently, it makes sense to closely analyze the uncertainties associated with mechanical motion.

For simplicity, assume the laser slab is a simply-supported thin plate, with the thin dimension along the z -axis. We will neglect any time dependence in this analysis. It may be shown that the equation for w , the displacement in the z -direction, is given by:¹²

$$\nabla^2 w(x,y) = -\left(\frac{M_T(x,y)}{1-\nu}\right), \quad (14)$$

where the thermal moment, defined as:¹²

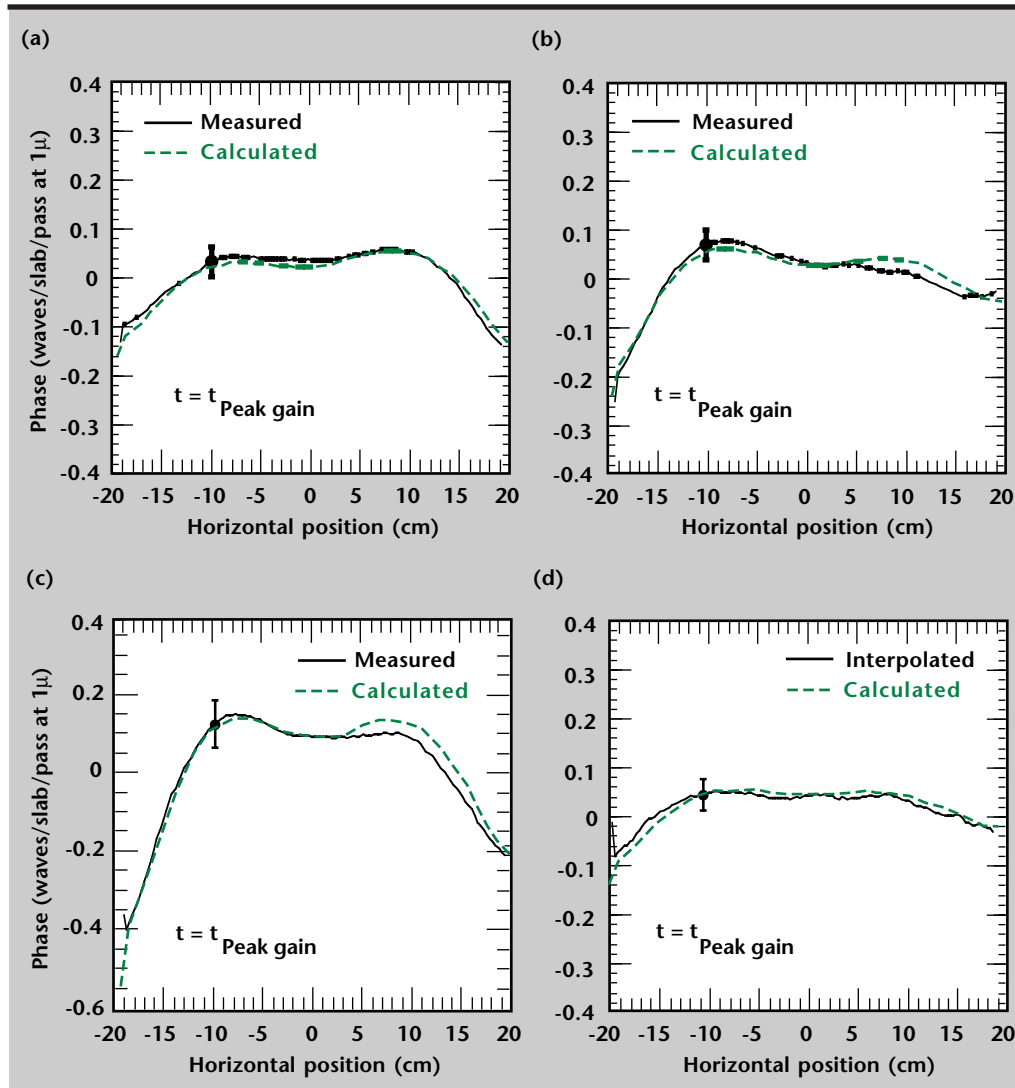


Figure 7. Measured and calculated wavefront, horizontal component—AMPLAB: (a) diamond configuration; (b) X configuration. Error bar shows typical error for measurements. (c) Three-slab-long configuration; (d) interior configuration—interpolated from 3-slab-long, diamond, and X results.

$$M_T(x, y) = \alpha E \int_0^h (z - h/2) T(x, y, z) dz \quad (15)$$

is the source function for the displacement. In **Eqs. 14** and **15**, ν is Poisson's Ratio, α is the thermal expansion coefficient, and E is Young's modulus.

On the time scales of interest, one may neglect diffusion. Consequently, $T(x, y, z) \propto Q(x, y, z)$. If one substitutes **Eq. 1** into **Eq. 15** using **Eq. 2**, one finds that the thermal moment is proportional to the difference in pump profiles, that is, $M_T \propto g_0(y) - g_h(y)$. Consequently, small uncertainties in the values of g_0 and g_h can lead to large uncertainties in the thermal moment, and hence the amount of deformation. Since the steering of the laser beam is driven by the curvature of the laser slab, it follows that the phase front, which is the integral of the beam-steering, is proportional to the gradient of the displacement, or the integral of the thermal moment.

With our 2-D ray-trace code, we can match the gain profile across the aperture to within 1%. Because of ASE within the laser slab, we can vary the pump profile by 2% and still be within 1% in the gain coefficient. Consequently, if we take the pump profiles shown in **Fig. 1**, and assume a worst-case uncertainty of 2%, it can be shown that the variation in the peak-to-valley value for the phase front can be as much as $\pm 15\%$.

Comparison with AMPLAB Experiments

In this section, we present comparisons of experiments performed in AMPLAB with the model described in the previous section. Unless otherwise mentioned, all comparisons are done at the time of peak gain at an explosion fraction of 0.2. As shown in **Fig. 6**, the OPD is calculated over the entire aperture. However to facilitate making comparison with the data, we shall show horizontal lineouts of calculations and experiments. These lineouts were taken at the vertical midplane of the aperture.

In **Figs. 7a** and **b**, we show the comparison between the calculated and measured phase front (essentially the negative of the OPD) for the diamond and X configurations in AMPLAB. Also indicated on the experimental curve is a typical value

for the error in the measurement. As may be seen, there is excellent agreement in both configurations over the entire aperture.

In **Figs. 7c** and **d**, we show the calculated and measured phase front for the 3-slab-long and interior configurations, respectively. As indicated on the graph, the data for the interior configuration was interpolated from the measured diamond, X, and 3-slab-long data using the following algorithm:

$$\phi_i = \phi_3/2 - \phi_d - \phi_x, \quad (16)$$

where ϕ_3 is the measured 3-slab-long phase in waves and all other phases are in waves/slab/pass. As can be seen from the figure, there is excellent agreement between calculation and measurement over the entire aperture.

Another check on the model is to calculate the wavefront distortion at times other than the time of peak gain. The results of these calculations, and comparison with the measurement, are shown in **Figs. 8a** to **f** (**Fig. 8b** is repeated for ease of comparison).

In these experiments, we measured the prompt wavefront distortion at 100, 200, 300, and 500 μ s after the time of peak gain. As may be seen, the amount of wavefront distortion continues to increase after the time of peak gain up to 500 μ s. In fact, the peak-to-valley value of the wavefront distortion is about three times greater at $t_{\text{peak gain}} + 500 \mu$ s than at $t_{\text{peak gain}}$. The agreement of the model with the measurement is excellent, matching both the magnitude and the shape of the wavefront at all times.

Summary and Conclusions

We have presented the results of detailed analysis and modeling of the AMPLAB data, summarized in **Table 1**.

We have also presented a description of our prompt pump-induced wavefront model. This model calculates the wavefront distortion due to mechanical deformation, and refractive index changes due to temperature and stress. We have benchmarked the code against AMPLAB measurements and will be using it to predict the wavefront distortion for the NIF amplifiers.

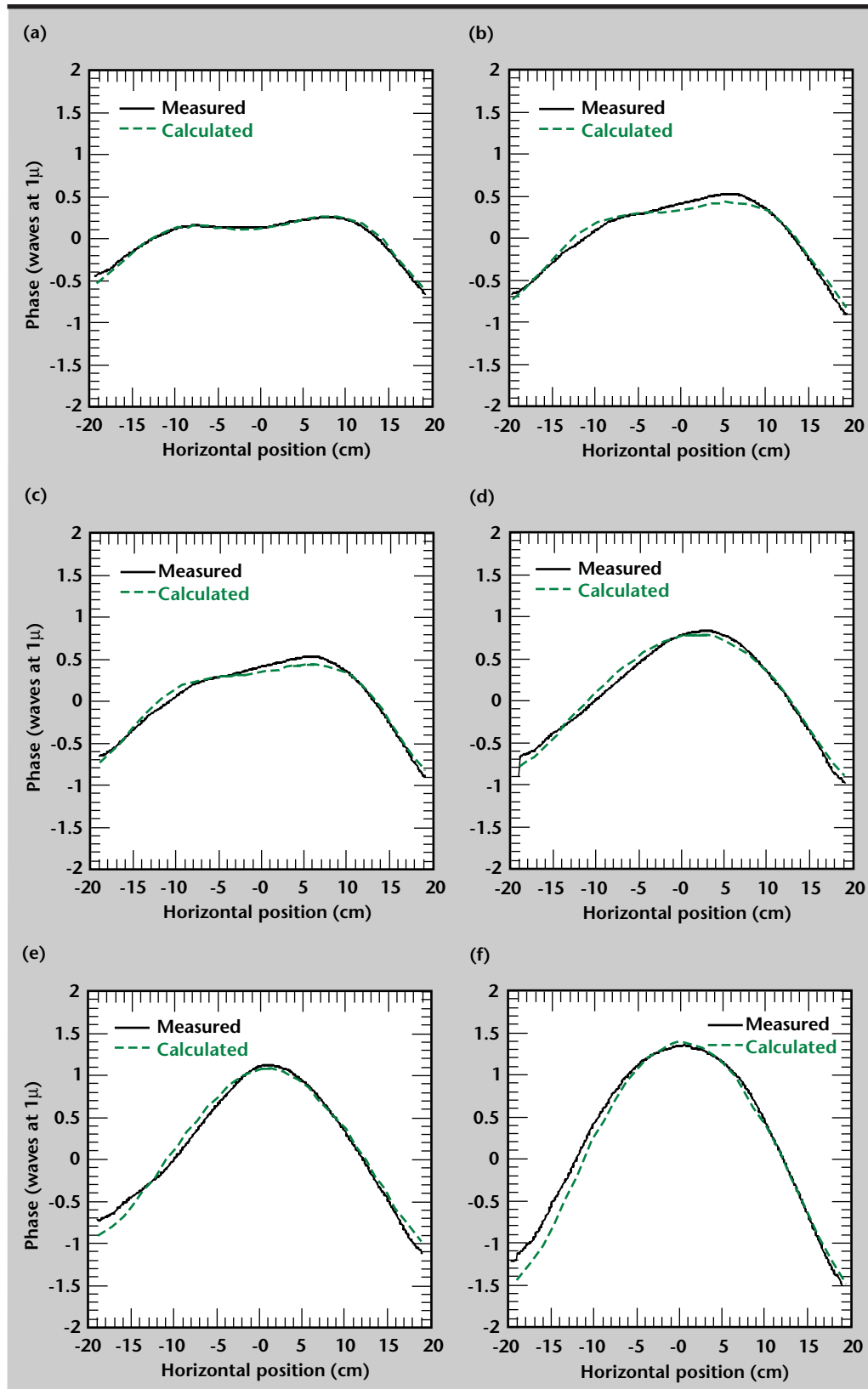


Figure 8. Measured and calculated wavefront, horizontal component—AMPLAB, diamond configuration: measurements taken at (a) $t = t_{\text{peak gain}}$; (b) $t = t_{\text{peak gain}} + 0.1$ ms for $f_x = 0.2$; (c) $t = t_{\text{peak gain}} + 0.1$ ms; (d) $t = t_{\text{peak gain}} + 0.2$ ms; (e) $t = t_{\text{peak gain}} + 0.3$ ms; and (f) $t = t_{\text{peak gain}} + 0.5$ ms.

Table 1. AMPLAB data analysis.

Configuration	Measured $\phi_{\text{horiz.}}$ (waves/slab/pass)	Calculated $\phi_{\text{horiz.}}$ (wave/slab/pass - LG-770)
Diamond	$0.22 \pm .03$	$0.21 \pm .03$
X	$0.29 \pm .03$	$0.27 \pm .04$
Interior	$0.18 \pm .03$	$0.16 \pm .02$

References

- Shapiro, A. (1985), "TOPAZ3D—A 3-D Finite Element Heat Transfer Code," Lawrence Livermore National Laboratory, Livermore, California (UCID-20484), August.
- Maker, B. N. (1995), "NIKE3D—A Nonlinear, Implicit 3-D Finite Element Code for Solid and Structural Mechanics," Lawrence Livermore National Laboratory, Livermore, California (UCRL-MA-105268, Rev. 1), April.
- Doss, S., and R. Gelinas (1986), "Mathematics and Physics of the BREW Code," Lawrence Livermore National Laboratory, Livermore, California (UCRL-50021-86), pp. 7-132.
- LeTouze', G., O. Cabourdin, J. F. Mengue, M. Rotter, and K. Jancaitis (1996), "Shaped Reflectors for Pump Cavities," *2nd Annual Conf. Solid State Lasers for Application to ICF*, Limeil, France.
- Jancaitis, K. (1986), "Flashlamp Modeling," Lawrence Livermore National Laboratory, Livermore, California (UCRL 50021-86), p. 6-3.
- Markiewicz, J. P., and J. L. Emmett (1966), "Design of Flashlamp Driving Circuits," *IEEE J.Q.E.*, **QE-2**, p. 707.
- Powell, H. T., A. C. Erlandson, K. S. Jancaitis, and J. E. Murray (1990), "Flashlamp Pumping of Nd:Glass Disk Amplifiers," *SPIE* **1277**, p. 103.
- Jancaitis, K. S. (1993), "Disk Amplifier Performance Model," Lawrence Livermore National Laboratory, Livermore, California (UCRL-LR-105820-88/89), p. 6-12.
- Stokowski, S. E., R. A. Saroyan, and M. J. Weber (1981), "Laser Glass - Nd-doped Glass Spectroscopic and Physical Properties, V1," M-095, Rev. 2, V. 1, Lawrence Livermore National Laboratory, Livermore, California.
- Born, M., and E. Wolf (1980), "Principles of Optics, 6th ed.," p. 122, Pergamon Press, New York, New York.
- Azzam, R. M. A., and N. M. Bashara (1987), "Ellipsometry and Polarized Light," North-Holland, Amsterdam, p. 488.
- Boley, B., and J. Weiner (1960), "Theory of Thermal Stresses," Ch. 12, John Wiley and Sons, New York, New York.

arallel Algorithm Development for Computational Mechanics

Carol G. Hoover and Robert M. Ferencz

*Defense Technologies Engineering Division
Mechanical Engineering*

Anthony J. De Groot and Robert J. Sherwood

*Defense Sciences Engineering Division
Electronics Engineering*

Edward Zywickz

*New Technologies Engineering Division
Mechanical Engineering*

Yuen L. Lee and Douglas E. Speck

*Computer Applications Division
Computations*

We have successfully implemented dynamic load balancing algorithms in the automatic contact and material erosion algorithms in the ParaDyn program. These algorithms provide an efficient method for treating arbitrary interface motion and extend the applicability and scalability of ParaDyn simulations to large problems of interest. ParaDyn algorithms for partitioning, parallel contact, and load balancing can be applied to parallel implicit methods. The most challenging algorithm research foreseen for future parallel models is the development of an efficient linear solver for both implicit solid mechanics and fluid models. New areas of development in particle continuum methods and parallel visualization are also described.

Introduction

This report features five parallel algorithm development projects that are part of our plan for implementing a full structural mechanics capability on our Accelerated Strategic Computing Initiative (ASCI) parallel computers.

Progress

Parallel Contact Algorithm with Load Balancing

Partitioning methods are the key to developing efficient algorithms for parallel computers. Generally, in designing parallel algorithms for a finite element method, the mesh is divided up by assigning elements to processors so that the calculation of the internal forces is balanced across the processors. However, some applications in nonlinear mechanics

involve calculating contact at material interfaces that may represent as much as fifty to eighty percent of the total computation time.

For example, timing results for a benchmark crashworthiness simulation show that nearly eighty percent of the total time is used for the contact calculation. In the algorithm described below two partitions are used. The first is a partitioning of the mesh and the second is a method for localizing and partitioning the contact surfaces.

In our previous work¹ we described a parallel technique for treating contact interfaces when the surface motion remained in a localized region of the mesh throughout the dynamics of the calculation. In the more general case it is not possible to define *a priori* which surfaces will come into contact. This more general form of contact, referred to here as arbitrary contact, will occur if material surfaces undergo folding or large deformation, or if objects on the grid are in motion.

Hence, a localization technique must be used. The arbitrary contact algorithm currently implemented in DYNA3D^{2,3} uses a localization technique that is conveniently extended into a parallel implementation. This algorithm is a node-on-patch method. The steps are as follows:

1. For each surface node, find a second surface node which is the nearest node in the remaining set of surface nodes;
2. Construct the facets connected to the second surface node; and
3. Determine whether the first surface node penetrates a facet connected to the second node. If so apply a contact force to prevent penetration.

The first step uses a grid of cubes, also referred to as buckets, to localize the search for nearest surface nodes. Surface nodes are sorted into the buckets and the search for the closest node is carried out over 27 buckets in three dimensions. The side length of the buckets is set to the maximum diagonal length of a face, plus an incremental length based on the velocity of the nodes forming the diagonal (**Fig. 1a**). This characteristic length is used so that at least one of the surface nodes associated with a penetrated patch is always contained in one of the 27 buckets in the set over which the search is conducted.

The parallel implementation of the arbitrary contact algorithm partitions the contact surfaces by allocating the buckets to processors. The buckets are added to the processors so as to approximately equalize the total number of surface nodes in each processor. One overlap bucket is needed across processors so that surface nodes in the center bucket of a strip of three buckets will find its connected patches in either the adjacent left or right bucket (**Fig. 1b**).

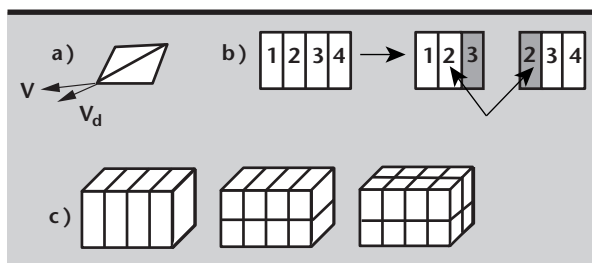


Figure 1. Illustration of the three steps in the load balancing of arbitrary contact surfaces. a) The bucket length is set to the maximum diagonal length of a face, plus a predicted incremental length based on the velocity along the diagonal; b) a set of buckets, in this case 4 1-D strips, is divided among two processors with one overlapping strip at the processor boundary; c) the grid of buckets is divided among processors by dividing the grid into 1-D slices, 2-D pipes, or 3-D cubes. The examples above show 4-, 8-, and 16-processor allocations of the same grid using slices, pipes, and cubes, respectively.

The allocation of buckets to processors is carried out by using 1-, 2-, or 3-dimensional geometric layout of processors (**Fig. 1c**). This corresponds to allocating buckets which are slices of the grid in one dimension, rectangular pipes in two dimensions, and cubes in three dimensions. The algorithm is currently implemented based on a fixed maximum number of buckets, N_{\max} , for the full problem. The processor geometry is selected based on whether the number of buckets for a particular processor geometry is less than N_{\max} . If more than one processor geometry satisfies this condition, then the processor geometry with the highest dimensionality is selected.

The use of two partitions (one for the full mesh and a second for contact surfaces) requires communication of the contact force values from the contact partition to the mesh partition. After this communication step, the total nodal forces are computed in processors associated with the mesh partition. Similarly, the time integration to compute the velocities and coordinates are calculated for nodal points in the mesh partition. After the time integration step, the updated nodal coordinates and velocities are communicated back to the processors containing the nodes in the contact partition.

The load balancing of the contact calculations occurs at time intervals corresponding to the time interval over which rebucketing occurs in the case of a single processor computer. This interval corresponds to the time required to move a surface node across the length of a bucket. The load balancing is carried out in parallel using parallel reduction operations which provide each processor with the global minimum and maximum for the geometry, the bucket structure, and the number of nodes in each bucket.

All processors then compute the rebucketing on the full grid. This is followed by a communication step in which each processor sends and receives surface nodes and patches corresponding to the buckets in the new contact partition.

Reliably detecting contact is a difficult task. **Figure 2** illustrates the deformation of a sheet of shell elements enclosed by moving stonewalls forming the faces of a cube. Contact detection for this problem uses the new method for treating contact which accounts for the thickness of shell elements. This problem runs correctly using 64 processors.

The material erosion algorithm in DYNA3D uses an algorithm formulation similar to the arbitrary contact described above and consequently was merged into the arbitrary contact algorithm. The erosion algorithm has been implemented in parallel during this last year. **Figure 3** illustrates the erosion algorithm for a small benchmark similar to the

model in large production calculations of a hypervelocity impact on a reentry vehicle.

Linear Solvers for Implicit Methods

Essentially all the parallel algorithmic strategies implemented within ParaDyn will be directly applicable to our implicit mechanics code, NIKE3D. However, NIKE3D's requirement for the solution of coupled systems of linear equations creates a new and significant challenge. Traditionally, linear equation solvers are divided into two classes: direct and iterative.

Direct methods are known for their robustness and predictable number of operations. However, they require a global data structure that grows rapidly with problem size and that presents challenges for large-scale parallelism.

Iterative methods typically use a much smaller data structure that can be readily distributed for large-scale parallelism. Unfortunately, the operation counts for iterative solvers grow enormously in the presence of ill-conditioning, that is, the existence of widely-spaced natural frequencies in the system. Sources of ill-conditioning are most often part of the simulations we seek to perform: material softening and damage, material anisotropy, mesh refinement to capture local effects, combined bending and membrane response of shells, and near-singularities as buckling behavior is approached.

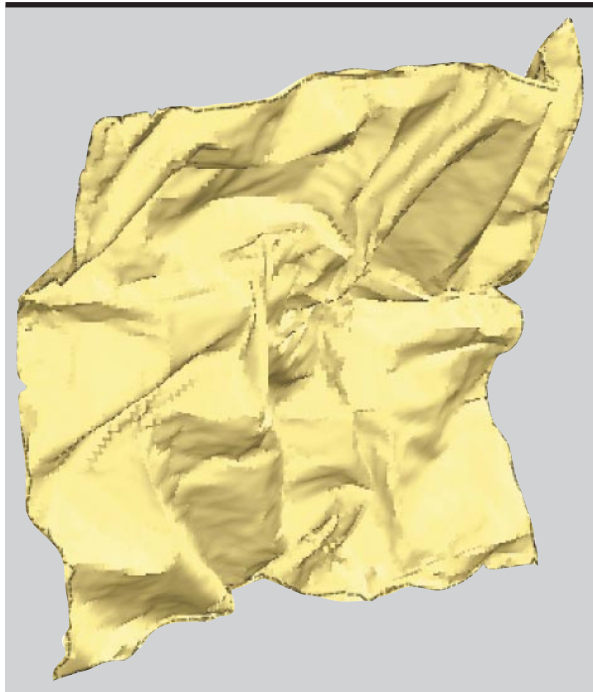


Figure 2. Arbitrary contact algorithm, used when a sheet of shell elements is deformed by moving stonewall boundaries that are the faces of a cube enclosing the sheet

These tradeoffs between direct and iterative methods mean there is no one technology presently available that totally meet our needs for parallel linear equation solving. Fortunately, this topic is a broad area of inquiry in the academic community and one that is well supported by multiple efforts within the ASCI program.

We are monitoring and interacting with these activities as we assess current capabilities. As an example, we completed an interface within NIKE3D to a parallel direct linear equation solver named PSPASES from the University of Minnesota.⁴ This was a prototype effort used to evaluate the linear solver technology.

The first processor acts as "master": it performs all I/O, computes the finite element matrices, and then works in cooperation with the remaining "slave" processors to perform the linear equation solving. This NIKE3D prototype is running in message-passing mode on our DEC cluster and IBM SP (ASCI Blue Pacific).

The test problem examined is the so-called Boussinesq problem: a concentrated force on the surface of an elastic half space. In this case the domain is represented by a mesh of $24 \times 24 \times 24$ hex elements, resulting in a system of 45,000 equations. This highly coupled system of equations is representative of those arising from true 3-D geometries.

The CPU data plotted in Fig. 4 immediately illustrate one limitation of this particular solver: it only permits the use of 2^N processors. Comparing the "linear algebra" and "total" CPU times for the uniprocessor run confirms that this simulation is dominated by the cost of linear equation solving.

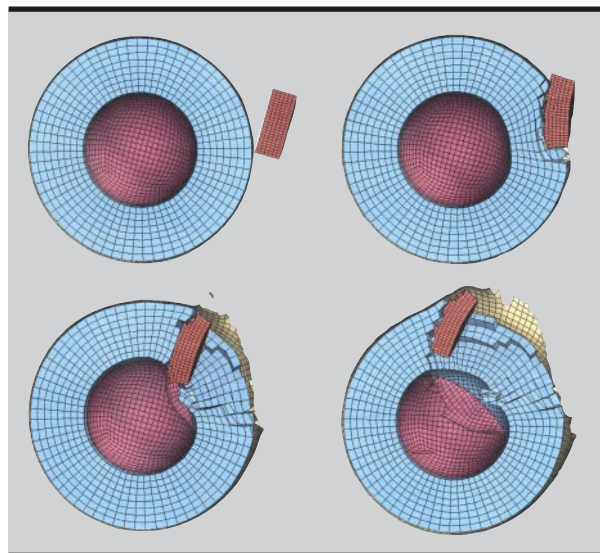


Figure 3. Benchmark test, illustrating the material erosion algorithm.

The trends for the parallel runs show reasonable scalability. Given the fixed problem size, the timing curve will flatten as the number of processors increases. The quite mild growth in the gap between the linear algebra CPU time for Processor 0 and the wall time for the factorization seems to indicate that communication latency is not a major penalty even for the case of 32 processors.

Finally, for the parallel runs, one sees a larger, though relatively constant offset between the linear algebra and total CPU time for Processor 0. This contrast from the uniprocessor case reflects the cost of mapping from NIKE's internal representation of the global system of equations to that required by this parallel solver. This cost could be readily eliminated by having NIKE assemble into the desired data structures from the outset.

When assessing the performance of a particular software library, it is important to characterize the effect of the available algorithmic features and run-time environment.

For example, the data in **Fig. 5** illustrate the impact of two different ordering strategies available in this package. Sparse direct solvers use a reordering of the equations to reduce the number of non-zero coefficients created during the factorization process. In one case, the "parallel" ordering option uses multiple processors to collectively perform this operation. The "serial" ordering restricts the operation to a single processor.

The latter approach has the advantage that the entire equation structure is simultaneously optimized, and thus a better overall ordering is attained.

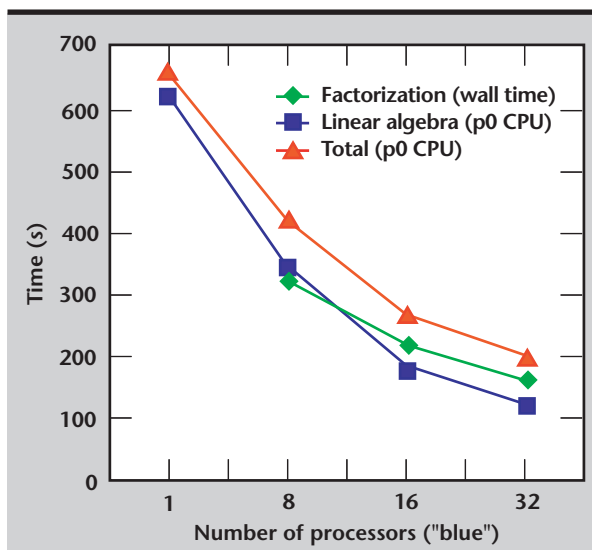


Figure 4. Timing comparison for the $24 \times 24 \times 24$ Boussinesq problem of uniprocessor NIKE3D with trials on the IBM R/S6000 SP (ASCI Blue-Pacific), using the PSPASES sparse direct parallel linear equation solver.

The developers note that typically the serial option results in twenty to thirty percent fewer non-zero terms in the factorized representation of the matrix, leading to possibly a factor of two reduction in arithmetic operations. These savings are reflected in **Fig. 5**.

Additional performance improvements will be available when we are able to use the SP's "User Space" high-speed communication sub-system. We are currently restricted to the slower "IP" communication sub-system, due to a combination of limitations in this prototype "master-slave" implementation, as well as the vendor's operating system.

The total memory graph in **Fig. 6** illustrates how memory for this benchmark grows with the number of processors when using the parallel reordering option in PSPASES. To provide a basis for comparison, note that a uniprocessor execution of NIKE3D using a sparse direct solver requires less than 600 Mb of total memory.

As mentioned previously, the parallel reordering cannot reduce factorization fill-in as effectively as serial reordering, thus more memory and floating-point arithmetic operations will be required. However, for sufficiently large problems, the serial reordering will require more memory than is available on a single node of the IBM SP system. In such instances the parallel option will be the only viable choice and we can anticipate the behavior shown in this graph.

Iterative methods for linear equation solving are not out of the running, and we look forward to additional improvements through ASCI-related efforts.

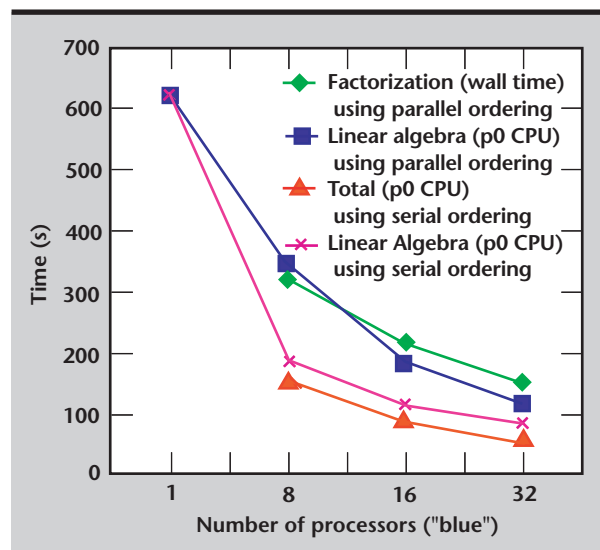


Figure 5. Timing comparison for the $24 \times 24 \times 24$ Boussinesq problem, using the two reordering strategies available within the PSPASES package.

For example, algorithms such as algebraic multi-grid have proved quite powerful for computational fluid dynamics and may prove equally useful for solid mechanics. And, looking at the relative strengths of direct and iterative methods, it is plausible that the ultimate solution will be the blending of the two technologies into so-called "hybrid methods."

One example of this approach is the FETI algorithm developed for large-scale aerospace structure by C. Farhat (University of Colorado).⁵ We are currently creating a prototype implementation of FETI which will be used to evaluate the methodology on problem classes of interest to Lawrence Livermore National Laboratory (LLNL).

Shared Memory Parallelism

We have been motivated to evaluate shared memory parallelism for our finite element programs for two reasons. Computer companies developing multiprocessor workstations and workstation clusters with up to 32 processors in a box are providing fast, efficiently-coded shared-memory parallel linear solvers. A second reason is that the target computer architecture for the ASCI Blue Mountain and Blue Pacific computers will consist of multiple processors on shared memory nodes connected with a very high speed interconnect network.

The ASCI architectures will support hybrid parallel models combining shared memory and message passing. Although the computer operating system and compiler software is very immature at this point, we have experimented with shared memory

parallel syntax in the DYNA3D program using the new OpenMP standard.

We had determined in earlier tests with NIKE3D that the automated compiler parallelism generated on a loop level provided parallel granularity that was too small to overcome the latency associated with allocating the threads to a processor. The DYNA3D shared memory implementation uses a large granularity for parallel tasks by defining OpenMp parallel regions in the upper level integration routine.

For example, the threads are initialized over the stress divergence calculation by element type. Threads are also distributed across the materials for each element type. Shared nodal data for the scatter step in the nodal force update are treated as a critical data region so that the nodal force update remains sequential. The contact algorithms are treated by spreading the loops which include large amounts of computational work over the processors.

The most tedious aspect of this implementation was the identification of shared and processor-local variables when parallel threads are initialized. Some modifications to the COMMON blocks storing element and material data were required in this step. Further modifications would be needed in the future for a hybrid model to identify shared and processor-local variables which are used in message passing data structures. This step would be taken only if the performance of the shared memory parallelism provides large speed gains over message passing models with multiple domains on a computer node.

Our performance results for shared memory parallelism are still quite preliminary. We find good performance for a two-processor SGI Octane workstation and also for some problems on a four-processor SGI Origin 200. On the other hand we have found it difficult to achieve good performance with some of our test cases using more than four processors on an SGI Origin 2000. By using performance analysis tools we were able to identify cache misses as the most significant limitation on the performance. Nodal reordering techniques may provide a remedy for these performance problems and may be investigated in the future.

Parallel Smooth-Particle Applied Mechanics

The use of particle techniques to solve the equations of continuum mechanics has become of increasing interest over the last decade. This interest in particle methods is motivated by the fact that they can be used to recast the partial differential

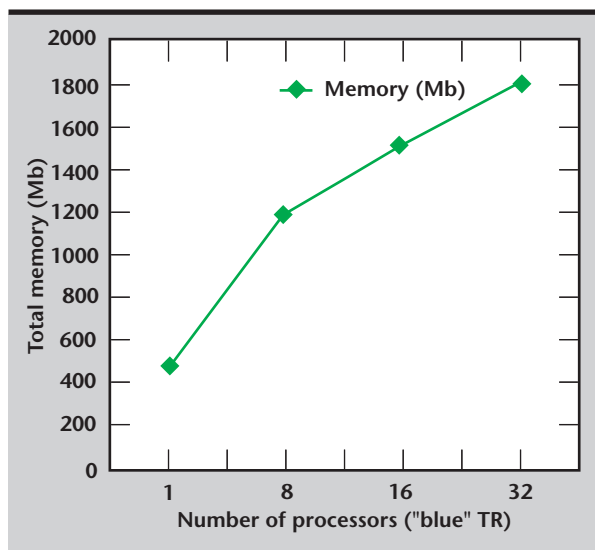


Figure 6. Memory comparison for the $24 \times 24 \times 24$ Boussinesq problem of uniprocessor NIKE3D with trials, using the PSPASES sparse direct parallel linear equation solver with parallel reordering.

equations describing continuum mechanics into a set of ordinary differential equations which may be easier or more efficient to solve numerically.

Perhaps a more compelling reason for using particle methods is that there is no underlying grid in the calculation. Thus, models for fracture, fragmentation, penetration mechanics, and plastic flow can be developed without resorting to adaptive grid methods.

The smooth-particle applied mechanics (SPAM) method, often referred to as smooth-particle hydrodynamics (SPH), is one of several particle methods.

SPAM has been applied to both solids as well as fluid mechanics problems.^{6,7} This method describes the continuum as a set of particles with each particle associated with a position and a weighting function. The weighting function has a range that smears out the particle over a region around its position. The density at any point in space is calculated by the summed contribution of all particles within the range of the point.

Similarly, other physical quantities such as velocity, strain, stress, and energy are calculated by the weighted averages of the same physical variables ascribed to the particles. Details of this method for converting the partial differential equations of continuum mechanics into an equivalent set of ordinary differential equations are described in the above references.

Work is in progress to develop a SPAM model for anisotropic granular solid-melt systems generated during mold filling and other manufacturing processes. Two-dimensional atomistic simulations of this system have been completed and will be compared to SPAM calculations for an equivalent continuum model.⁸ A parallel implementation of a two-dimensional SPAM algorithm is under development and will be used for simulating solid-melt systems on ASCI parallel computers.

Parallel Visualization

In anticipation of problem sizes in the range of 15 million elements and larger, we are developing a prototype parallel visualization tool based on the GRIZ program. Our initial implementation assumes the domain decomposition from the finite element analysis and uses a master/slave parallel model which splits GRIZ functionality over one master processor and multiple slave processors. The master processor is responsible for all interactive functions including full frame display and interactive menu and mouse commands. The slave processors compute results and render frames associated with their subdomain from the full mesh.

Frame generation proceeds as follows. The master processor receives user input to generate a frame displaying a result (primal or derived). The master broadcasts this command to slave processors that process the command, calculate results, and render their portion of the frame into a local offscreen frame buffer. The slave processors perform a global reduction of the pixel color values, based on their associated z-buffer (depth) values to arrive at a composite mesh image across all subdomains. The composite mesh image is sent to the master, which loads it into the user's frame buffer and renders foreground information such as text, labels, and colormap over it.

We use two MPI (Message Passing Interface) communicator groups to implement this model. The first contains the master and all of the slave nodes. The second contains slave nodes only.

This parallel prototype is implemented in the Mili version of GRIZ. Mili (Mesh I/O Library) provides code developers with a flexible tool for creating self-defining binary data bases for the visualization of complex grids. The self-defining feature is particularly useful for parallel simulations where it is important to limit the size of the resulting data sets.

Future Work

The ParaDyn program has matured to a full production status. New algorithms or extensions to existing DYNA3D algorithms are now being designed with a plan that includes the parallel implementation. Three projects scheduled for next year are: 1) to write a users' manual for the ParaDyn program; 2) to add message-passing communication to the Lagrange contact algorithm; and 3) to complete the programming for the few remaining DYNA3D options not implemented in parallel.

Future development projects will include parallel algorithm development for NIKE3D and a collaborative effort with LLNL's Thermal Fluids Group to develop parallel versions of TOPAZ3D and fluid codes used in coupled thermomechanical analysis.


Investigations will continue in grid-free methods such as SPAM. These methods may prove to be useful in capturing highly localized physical phenomena when used in combination with finite element methods which describe a large-scale engineering analysis on a parallel computer.

Acknowledgments

We gratefully acknowledge support for ParaDyn code development from the Weapons Program at LLNL and from the Department of Defense High-

Performance Computing and Modernization Program. We especially thank M. Giltrud from the Defense Threat Reduction Agency (formerly the Defense Special Weapons Agency) for funding both serial and parallel contact algorithm development. Professor W. Hoover (University of California, Davis) inspired the model for the crumpled material benchmark for ParaDyn. He has also conducted extensive research on the SPAM algorithm and has developed many physical applications using the method. We appreciate the feedback and helpful comments from analysts running the ParaDyn program, especially D. Badders, T. Lee, and D. Faux from LLNL, and R. Namburu and P. Papados from the U. S. Army Corps of Engineers Waterways Experiment Station.

References

1. Hoover, C. G., A. J. De Groot, and R. J. Sherwood (1998), "Parallel Contact Algorithms for Explicit Finite Element Analysis," *Modeling and Simulation Based Engineering*, S. N. Atluri and P. E. O'Donoghue, eds., Tech Science Press, Palmdale, California.
2. Whirley, R. G., and B. E. Engelmann (1993), "DYNA3D: A Nonlinear, Explicit, Three-Dimensional Finite Element Code for Solid and Structural Mechanics—User Manual," Lawrence Livermore National Laboratory, Livermore, California (UCRL-MA-107254, Rev. 1).
3. Benson, D. J., and J. O. Hallquist (1990), "A Single Surface Contact Algorithm for the Post-Buckling Analysis of Shell Structures," *Computer Methods in Applied Mechanics and Engineering*, Vol. **78**, pp. 141-163.
4. Gupta, A., F. Gustavson, M. Joshi, G. Karypis, and V. Kumar (1997), "Design and Implementation of a Scalable Parallel Direct Solver for Sparse Symmetric Positive Definite Systems," *Proceedings, Eighth SIAM Conference on Parallel Processing*.
5. Farhat, C., and F.-X. Roux (1991), "A Method of Finite Element Tearing and Interconnecting and its Parallel Solution Algorithm," *International Journal for Numerical Methods in Engineering*, Vol. **32**, pp. 1205-1227.
6. Posch, H. A., W. G. Hoover, and O. Kum (1995), "Steady-state shear flows via nonequilibrium molecular dynamics and smooth-particle applied mechanics," *Physica Review E*, Vol. **52**, No. 2, pp. 1711-1720.
7. Hoover, W. G., T. G. Pierce, C. G. Hoover, J. O. Shugart, C. M. Stein, and A. L. Edwards (1994), "Molecular Dynamics, Smoothed-Particle Applied Mechanics, and Irreversibility," *Computers Math. Applic.*, Vol. **28**, No. 10-12, pp. 155-174.
8. Hoover, W. G., and S. Hess (1998,) "Anisotropic Plasticity with Embedded-Atom Potentials," *Physica A*, in preparation. 

DYNA3D-TOPAZ3D Coupling and DYNA3D-NIKE3D Linkage

Jerry I. Lin

*Defense Technologies Engineering Division
Mechanical Engineering*

This report describes the coupling of DYNA3D and TOPAZ3D and the linkage between DYNA3D and NIKE3D. The combined DYNA3D-TOPAZ3D code provides a tool for coupled thermal-mechanical analyses, and the DYNA3D-NIKE3D link enables the multi-staged simulations for structural/continuum mechanics problems. For a coupled thermal-mechanical analysis, DYNA3D and TOPAZ3D run in parallel and exchange structure/continuum deformation and temperature as the analysis progresses. For structural/continuum mechanics problems involving different regimes of loading, deformation, or frequency characteristics, the DYNA3D-NIKE3D link is designed to run in series. It aims to fully use the explicit/implicit advantages of the individual codes at the proper stages.

Introduction

Over the years, coupled thermal-mechanical engineering problems had been solved by a “weak coupling” approach of mechanics codes and heat transfer codes. The analyst first runs a thermal analysis for the model by TOPAZ3D,¹ a 3-D, implicit heat transfer finite-element (FE) code, and writes the temperatures at selected times to a file. These temperatures are then read from the file at their corresponding times in the subsequent mechanical analysis, usually by the 3-D, explicit structural/continuum FE code DYNA3D.² The coupling is achieved through the use of temperature-dependent material properties or temperature change-induced thermal stresses. From the structural analysis standpoint, this procedure does reflect the temperature-sensitive nature of the problem, but does not quite capture the essence of thermal-mechanical interaction.

With the evolution of the weapon systems and the expanding scope of laser-related applications at Lawrence Livermore National Laboratory, the importance of detailed thermal-mechanical stress analysis has become evident. The integration of DYNA3D and TOPAZ3D is intended to accomplish this goal. When requested by a user, TOPAZ3D would be compiled as a program module in DYNA3D. For a thermal-mechanical analysis, the coupling is then achieved by the continuous exchange of deformation and temperature data between these codes on a real-time basis.

The link between DYNA3D and NIKE3D,³ an implicit, structural/continuum FE code, is arranged in a serial mode and intended to solve certain classes of structural/continuum mechanics problem. This combined explicit-implicit method is particularly effective for simulations involving initial stress, such as failure analysis of rotating fan blades, or residual stress, such as sheet metal forming process with spring-back.

Due to its explicit nature, DYNA3D would have difficulty attaining an equilibrium state for the rotation-induced initial stresses in the fan blades or sustaining a long duration simulation of spring-back phenomena, whereas the implicit NIKE3D is perfectly suited for these purposes. However, the impulsive loading, high nonlinearities and complicated contact conditions in the transient phase of these problems usually render NIKE3D ineffective and necessitate the use of DYNA3D.

The capability of reading a file generated by its opposite code, and writing a file for its opposite code is implemented in both DYNA3D and NIKE3D. This binary file contains the nodal kinematic variables and element stresses, strains, and other state variables. Series of DYNA3D and NIKE3D analyses, with essential data transmitted through this file, can be strung along to solve complicated multi-phase problems. Different element formulations are preferred in DYNA3D and NIKE3D because of their explicit/implicit natures. Change of element formulation is permitted during the transition from one code to the other to accommodate this fact.

Progress

DYNA3D-TOPAZ3D Coupling

In DYNA3D, temperature dependency can be established through the use of material type 4 (thermal-elastic-plastic), type 15 (Johnson/Cook elastic-plastic), type 21 (thermal-orthotropic-elastic) or type 23 (thermal-orthotropic-elastic with variable properties). They have either the material temperature as part of the constitutive equations, or temperature-dependent material properties. Because of different time increments used in time integration in these codes—usually a greater time step in the implicit TOPAZ3D, and a smaller one in the explicit DYNA3D—the coupling can be executed only when the simulation times in both codes are synchronized. The temperatures at the intermediate DYNA3D steps are obtained by linear interpolation.

The coupling procedure, depicted in **Fig. 1**, can be described as follows:

1. DYNA3D feeds current nodal coordinates to TOPAZ3D when simulation clocks in both codes are synchronized.
2. TOPAZ3D does a thermal analysis and returns the updated current temperature to DYNA3D at the end of this thermal step. TOPAZ3D advances its clock.
3. DYNA3D executes the mechanical analysis based on the current temperatures provided by TOPAZ3D and advances its clock incrementally until the clock catches the TOPAZ3D clock.

This process repeats itself until it reaches the designated simulation time.

A TOPAZ3D compilation flag is set in DYNA3D. Only if the flag is activated will TOPAZ3D be integrated into DYNA3D. A special arrangement is also made to have the temperatures written into the DYNA3D plot database for post-processing purposes.

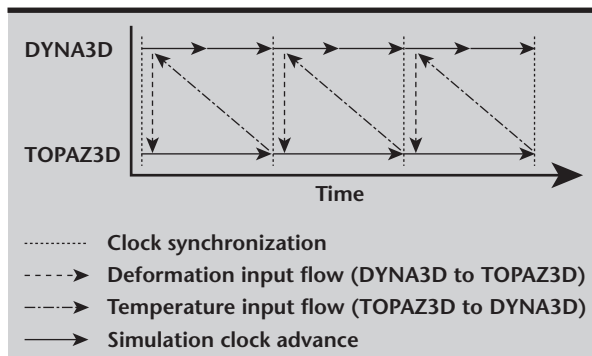


Figure 1. Illustration of DYNA3D-TOPAZ3D coupling procedure.

DYNA3D-NIKE3D Link

Due to the explicit nature of DYNA3D, the Belytschko-Lin-Tsay shell element⁴ and the uniformly under-integrated hexahedral elements (URI)⁵ are the preferred elements in DYNA3D. On the other hand, the Hughes-Liu shell element and the Selective-Reduced Integrated (SRI)⁶ hexahedral element are favored by NIKE3D because of its implicit integration approach.

To take full advantage of the codes' characteristics, different elements can be used in these codes. A transformation of the shell element stresses to the global coordinate system is performed before DYNA3D writes them into the link file. It ensures the stresses NIKE3D reads are as expected by the code. A reverse stress transformation is also done right after DYNA3D reads the link file generated by NIKE3D. For hexahedral continuum elements, NIKE3D averages the stresses at element integration points to give DYNA3D elements a uniform stress state, and imposes uniform stresses on element integration points while reading the stresses from the DYNA3D-generated link file.

The SRI hexahedral elements as well as a fully integrated shell element⁷ have been implemented into DYNA3D, whereas the URI and shell elements have been added to NIKE3D, to give both codes a complete element library. In the event that high fidelity transfer from one code to the other is necessary, users have the choice to use unified element formulations, albeit it may come with a high price on DYNA3D analysis.

Figure 2 depicts the sequence for a typical multi-phase mechanical analysis. A Pokel Cell example (**Fig. 3**) is used to demonstrate the advantages of the combined analysis. In this problem, an O-ring is being pressed into the seal groove by a piece of laser glass. Because of the O-ring's viscous elastic material behavior, the response includes a sharp rise of stress in the loading phase and a prolonged relaxation in the unloading phase. DYNA3D can handle the transient loading phase with ease, but would have difficulty bringing the stress to a relaxed steady state. The use of NIKE3D during the unloading phase results in a satisfactory solution, as shown in the stress-time plot in **Fig. 3**.

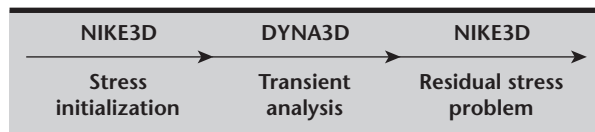


Figure 2. Illustration of DYNA3D-NIKE3D link sequence for typical multi-phase mechanical analysis.

In large scale models, especially with complicated contact conditions or a long simulation time, DYNA3D users sometimes encounter spatial instability that cannot be controlled by the existing anti-hourglass algorithms. With the multi-point integrated elements now available in DYNA3D, users have the option to deploy them at critical parts of the mesh that are particularly susceptible to hour-glass modes.

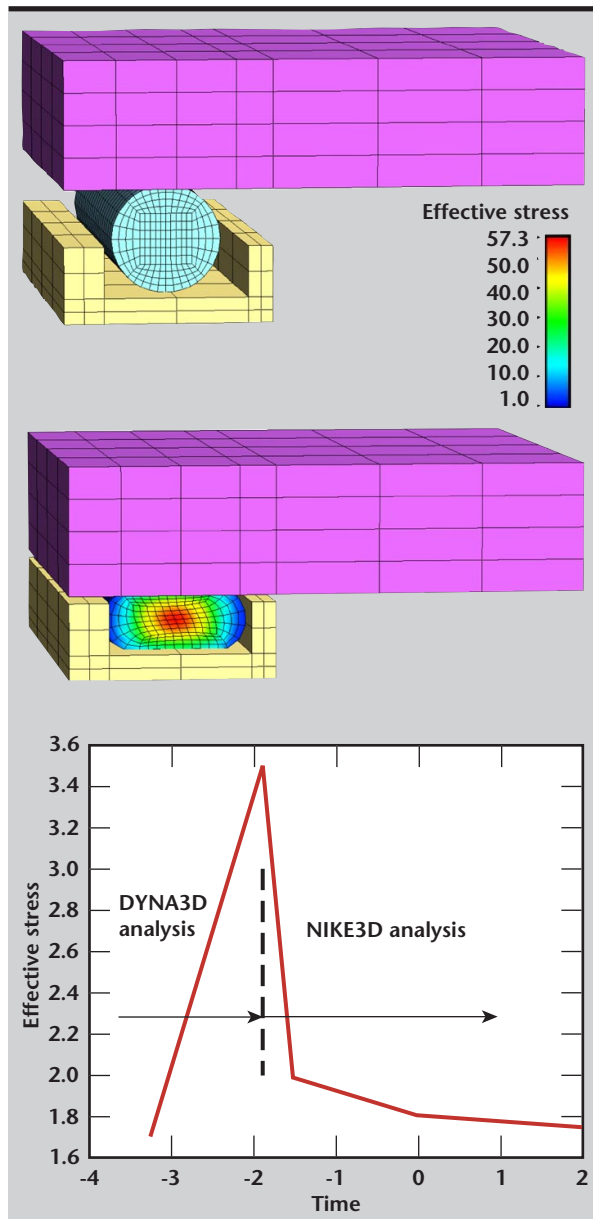


Figure 3. DYNA3D-NIKE3D example: stress-time plot, showing use of NIKE3D during the unloading phase.

Future Work

For coupled thermal-mechanical analyses, the possible temperature change due to the dissipation of element plastic strain energy still needs to be accounted for. This plastic strain energy must be computed by DYNA3D and transferred along with the deformation to TOPAZ3D.

On the DYNA3D-NIKE3D link, we are looking into the implementation of global stress interpolation schemes in DYNA3D. It would enable DYNA3D to provide non-uniform element stresses, without the high cost of multi-point integrated elements, to NIKE3D.

Acknowledgments

The DYNA3D-TOPAZ3D coupling is a joint effort by A. Shapiro and the author. The DYNA3D-NIKE3D link and the implementation of new elements are a team effort by M. Puso, E. Zywickz, and the author.

References

1. Shapiro, A. B. (1985), *TOPAZ3D—A Three-Dimensional Finite Element Heat Transfer Code*, University of California, Lawrence Livermore National Laboratory, Livermore, California UCID-20484.
2. Whirley, R. G., and B. E. Engelmann (1993), *DYNA3D: A Nonlinear, Explicit, Three-Dimensional Finite Element Code for Solid and Structural Mechanics—User Manual*, University of California, Lawrence Livermore National Laboratory, Livermore, California UCRL-MA-107254.
3. Maker, B. N. (1995), *NIKE3D: A Nonlinear, Implicit, Three-Dimensional Finite Element Code for Solid and Structural Mechanics—User's Manual*, University of California, Lawrence Livermore National Laboratory, Livermore, California UCRL-MA-105268.
4. Belytschko, T., J. I. Lin, and C. S. Tsay (1984), "Explicit Algorithms for the Nonlinear Dynamics of Shells," *Computer Methods in Applied Mechanics and Engineering*, **42**, pp. 225-251.
5. Goudreau, G. L., and J. O. Hallquist (1982), "Recent Developments in Large Scale Finite Element Lagrangian Hydrocode Technology," *Computer Methods in Applied Mechanics and Engineering*, **30**.
6. Hughes, T. J. R. (1987), *The Finite Element Method: Linear Static and Dynamic Finite Element Analysis*, Prentice-Hall, Princeton, New Jersey, pp. 232-237.
7. Bathe, K., and E. N. Dvorkin (1985), "A Four-Node Plate Bending Element Based On Mindlin/Reissner Plate Theory and a Mixed Interpolation," *International Journal for Numerical Methods in Engineering*, **21**, pp. 367-383.



Physically-Stabilized Eight-Node Hexahedral Element

Michael A. Puso

*Defense Technologies Engineering Division
Mechanical Engineering*

We have developed a novel single-point integration scheme that performs as well as the fully integrated element for many problems, but is much more efficient computationally. We used the physical stabilization method to compute the hourglass forces by a Taylor series expansion of the stresses and strains about the center of the element.

Introduction

The explicit and implicit finite-element methods have spawned two different element types to maximize their efficiencies. The bottleneck for the explicit method is the strain and constitutive evaluations. Consequently, we have used a single-point integration method, where these evaluations are made only at the center of the element. To make up for the loss of resolution from the single-point integration, more elements are used in the calculation.

On the other hand, the bottleneck for the implicit method is the inversion of a system of linear equations. Consequently, it is desirable to reduce the number of equations/elements in the analysis by using a higher-order integration rule over the spatial domain of the element, to gain resolution and stability. However, the increased use of mixed implicit/explicit analysis necessitates a new element strategy that combines the austerity of the single-point integration with the robustness of the multiple-point integration. In this work, a novel single-point integration scheme is developed that performs as well as the fully integrated element for many problems but is much more efficient computationally.

Progress

The single-point integration method requires hourglass control to eliminate zero-energy modes, to remain stable. The perturbation method currently used in explicit finite-element codes requires *ad hoc* parameters to calculate the hourglass forces and, consequently, can give poor results particularly for coarse meshes.

In this work, we use the physical stabilization method to compute the hourglass forces by a Taylor series expansion of the stresses and strains about the center of the element. This allows the element to be integrated in closed form, providing the exact hourglass forces for initially parallelepiped elements. Consequently, no artificial parameters are required to preclude hourglassing.

As many analysts know, some problems require calibration of hourglass parameters to eliminate hourglassing in a mesh while avoiding spurious stiffening of the structure. This new method should eliminate this time-consuming procedure and provide better coarse mesh accuracy, particularly for bending-dominated problems.

After contact, the hourglass control forces are typically the most expensive calculation in the explicit method. For an all brick element problem with no contact and a simple elastic material, stiffness-based hourglass forces comprise twenty percent of the total CPU time. With the new physical stabilization method, the hourglass forces will comprise about thirty percent of the total CPU time. Overall, this amounts to a ten percent increase in total CPU time for the worst case.

With problems including contact and more expensive material models, the extra time for the physical stabilization will be further amortized. Compare this to a fully integrated element, which takes between four and six times more CPU time in the element calculation than the perturbation method.

This physical stabilization method is implemented into DYNA3D and NIKE3D for general use and can be exploited in mixed explicit/implicit analysis via the DYNA3D/NIKE3D link, or the NIKE3D implicit/explicit analysis mode.

Theory

The perturbation hourglass control method can apply either elastic or damping forces to resist the hourglass modes. Although slightly more efficient, the damping-based method is entirely non-physical and is not applicable to static problems, since motion is required to resist the modes. Furthermore, with the damping method, hourglass modes will always eventually become evident in problems where boundary conditions allow them to propagate. Only the stiffness-based hourglass control methods are considered here.

Flanagan and Belytschko¹ were the first to use the orthogonal hourglass control method for 3-D nonlinear transient analysis. This method uses the so called γ stabilization vectors, which are orthogonal to the homogenous strain states, and consequently satisfy the patch test, providing a convergent formulation for hourglass control. In the first appearance of physical stabilization,² this method was applied to shells and four-node quadrilateral elements (2-D).

The first physical stabilization method applied to eight-node hexahedral elements (3-D) was by Belytschko and Bindeman.³ This method alleviated the problems of locking due to incompressibility, and avoided the parasitic shear locking in bending-dominated problems for undistorted elements. But the element required a co-rotational coordinate system, which is only well-posed for parallelepiped elements and in general is not indifferent to element node number.⁴

Furthermore, hourglass forces are not convected with the deformation in a consistent fashion. Zhu and Cescotto⁵ proposed a general method for physical stabilization of the eight-node hexahedral but required the storage of 36 hourglass stresses, as opposed to the twelve hourglass forces quantities usually needed. Also, no valid solution to parasitic shear locking was offered.

In this work we formulate a physical stabilization method that uses the convected frame in lieu of a co-rotational frame.³ This allows us to use an assumed strain field for the hourglass forces, which can avoid shear lock yet be frame-indifferent. Furthermore, only twelve hourglass forces are needed, and hourglass forces are correctly convected for material models using the so-called convected or Truesdale rate (for example hyperelasticity, F_e/F_p plasticity model).

For ordinary general hypoelastic models the hourglass forces are valid for small strain/large rotation, but should still be effective.

In the finite-element method, the internal forces for an element with domain Ω_e is given by

$$\mathbf{F}_{int} = \int_{\Omega_e} \mathbf{B}^T \boldsymbol{\sigma} dV, \quad (1)$$

where \mathbf{B} is the strain displacement matrix and $\boldsymbol{\sigma}$ is the stress. In single-point integration, only the values of the stress and strain displacement at the element center ($\boldsymbol{\sigma}_o$ and \mathbf{B}_o) are used in Eq. 1 so that the internal force is calculated at time $n+1$ by

$$\mathbf{F}_{int}^{n+1} = \int_{\Omega_e} \mathbf{B}_o^T(t_{n+1}) \boldsymbol{\sigma}_o(t_{n+1}) dV. \quad (2)$$

The additional forces used to preclude the zero-energy modes are given by the update:

$$\begin{aligned} \mathbf{F}_{hg}^{n+1} &= \sum_{i=1}^4 \Gamma_i \mathbf{f}_i^{n+1}, \\ \mathbf{f}_i^{n+1} &= \mathbf{k}_{ij} \Gamma_j^T \Delta \mathbf{u} + \mathbf{Q} \mathbf{f}_i^n \end{aligned} \quad (3)$$

where

$$\begin{aligned} \mathbf{k}_{ij} &= \alpha \delta_{ij} \mathbf{I}_{3 \times 3}, \\ \Gamma_i &= \begin{bmatrix} \gamma_i & 0 & 0 \\ 0 & \gamma_i & 0 \\ 0 & 0 & \gamma_i \end{bmatrix}, \end{aligned} \quad (4)$$

γ_i is the i^{th} 8×1 stabilization vector, $\Delta \mathbf{u}$ is the incremental displacement, \mathbf{Q} is the incremental rotation given by the spin at the element center, \mathbf{f}_i is the i^{th} 3×1 hourglass force, and α is the artificial hourglass control parameter.

In the physical stabilization method, it is recognized that the strain matrix has a constant and bilinear (or hourglass) portion, such that $\mathbf{B} = \mathbf{B}_o + \mathbf{B}_{hg}$. Furthermore, by using the following approximation:

$$\frac{\partial(\cdot)}{\partial \mathbf{x}} \approx \frac{\partial \xi}{\partial \mathbf{x}_{\xi=0}} \frac{\partial(\cdot)}{\partial \xi}, \quad (5)$$

to calculate the hourglass portion of the strain displacement matrix, certain orthogonality conditions can be exploited such that Eq. 1 can be integrated in closed form.

In this work the Truesdale rate is used as the objective rate in the constitutive law, such that the volume integration can precede the constitutive time integration in Eq. 1, and the 36 hourglass stresses per element needed (that is, stored) are condensed to just 4 3×1 hourglass forces needed in the update.

An assumed strain field is used for the contravariant strain tensor so that parasitic shear lock is avoided for bending-dominated problems. The following form is used to calculate the hourglass forces:

$$\mathbf{F}_{hg}^{n+1} = \sum_{i=1}^4 \Gamma_i \mathbf{f}_i^{n+1},$$

$$\mathbf{f}_i^{n+1} = \mathbf{k}_{ij} \Gamma_j^T \Delta \mathbf{u} + \mathbf{J}_o \mathbf{f}_i^n \quad (6)$$

where

$$\mathbf{k}_{ij} = \sum_{l=1}^6 \mathbf{J}_o \mathbf{B}_{il}^T \mathbf{J}^{-T} \mathbf{C} \mathbf{J}^{-1} \mathbf{B}_{jl} \mathbf{J}_o^T, \quad (7)$$

\mathbf{J}_o is the 3-x-3-element Jacobian at the element center, \mathbf{C} is the 6-x-6 material stiffness, \mathbf{J} is the 6-x-6 matrix that transforms the incremental strain vector onto the covariant coordinate system form by the columns in \mathbf{J}_o , and \mathbf{B}_{ij} is a 6-x-3 matrix that accounts for the individual contravariant strains.

Although Eq. 7 looks ominous, about half the \mathbf{B}_{ij} s are zero matrices. The other half are sparse, in that they include at most two ones. The remaining terms are zeros. Furthermore, some redundancies can be exploited in the implementation. The bottom line is that Eq. 7, when implemented appropriately, is not exorbitantly expensive. As mentioned, the new method takes about 50% longer than the perturbation method, resulting in at most a ten percent increase in total CPU time.

Examples

Many problems work quite well with the perturbation method hourglass control, depending on the boundary conditions and material properties involved. In problems with highly anisotropic material properties or point loads that occur due to boundary conditions or contact, the perturbation method may not eliminate all hourglassing and give poor results in coarse meshes. Furthermore, hourglass parameters that are too big cause the problem to be overly stiff.

The following plate problem illustrates the penalty sensitivity that can sometimes occur. A square plate with the following material properties:

$$\begin{aligned} E_x &= 50000 \text{ ksi}, & E_y &= 100 \text{ ksi}, & E_z &= 100 \text{ ksi} \\ G_x &= 10000 \text{ ksi}, & G_y &= 10000 \text{ ksi}, & G_z &= 10000 \text{ ksi} \\ V_{yx} &= 0.00075, & v_{zx} &= 0.3, & v_{zy} &= 0.3 \end{aligned}$$

is loaded at the center, as shown in Fig. 1. The hourglass parameter α from Eq. 3 is chosen to be some percentage of the maximum Eigenvalue in the stiffness matrix. In DYNA3D and NIKE3D this amounts to the following equation for the orthotropic material models:

$$\alpha = \kappa \cdot 0.05 \cdot E_{\max} \cdot (\mathbf{B}_o)_{ij} (\mathbf{B}_o)_{ij}, \quad (8)$$

where \mathbf{B}_o is the strain displacement matrix and $\kappa = 0.1$ by default. This value of κ proves overly stiff, and three other values for κ are tried: $\kappa = 0.00002$, 0.0002 , and 0.002 . The value $\kappa = 0.1$ ($100/50000$) = 0.0002 replaces E_{\max} with E_{\min} in Eq. 8 and uses the default 0.1 , which seems to work well with isotropic materials.

Two different loadings shown in Figs. 1 and 2 are analyzed with the five different meshes (Table 1).

Figures 3 and 4 show results for the different meshes using the different κ s, the physical stabilization method (denoted by ps) and full integration (using the incompatible modes element). For the load case in Fig. 1, from Fig. 3 it is seen that the physical stabilization method converges at about the same rate as the fully integrated element. With $\kappa = 0.0002$, the perturbation method performs well, whereas with 0.00002 it is too soft, and with 0.002 it is too stiff for the mesh densities used.

Table 1. Matrix parameters.

$n_z \times n_x \times n_y$	No. of elements
$1 \times 6 \times 6$	36
$3 \times 6 \times 6$	54
$3 \times 13 \times 13$	507
$6 \times 26 \times 26$	4056
$7 \times 38 \times 38$	10108

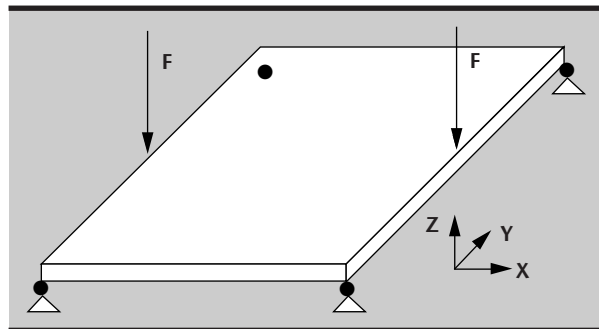


Figure 1. Loading case 1: 20-in.-x-20-in.-x-1-in. plate with 8-lb edge loads and simple supports.

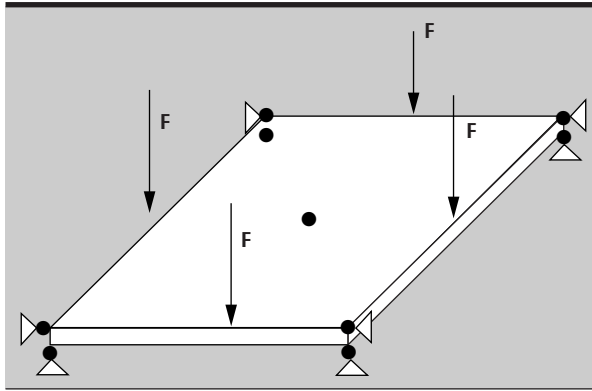


Figure 2. Loading case 2: 20-in.-x-20-in.-x-1-in. plate with 32000-lb edge loads and clamped supports.

For the load case in Fig. 2, we get some hourglassing for $\kappa = 0.00002$ and 0.0002 , as seen in Fig. 5. For $\kappa = 0.002$, we get no hourglassing, but as seen in Fig. 4, the perturbation method gave results that were too soft. The physical stabilization method gives no hourglassing (Fig. 6), and again converges at the same rate as the fully integrated element.

The conclusion to be drawn from these examples is that the perturbation method does not perform well under certain types of loadings and the results are highly sensitive to the values of the stiffness parameter, κ . The new physical stabilization method is very reliable since its hourglass forces are derived from the fully integrated element.

Figure 3. Convergence plot for loading case 1.

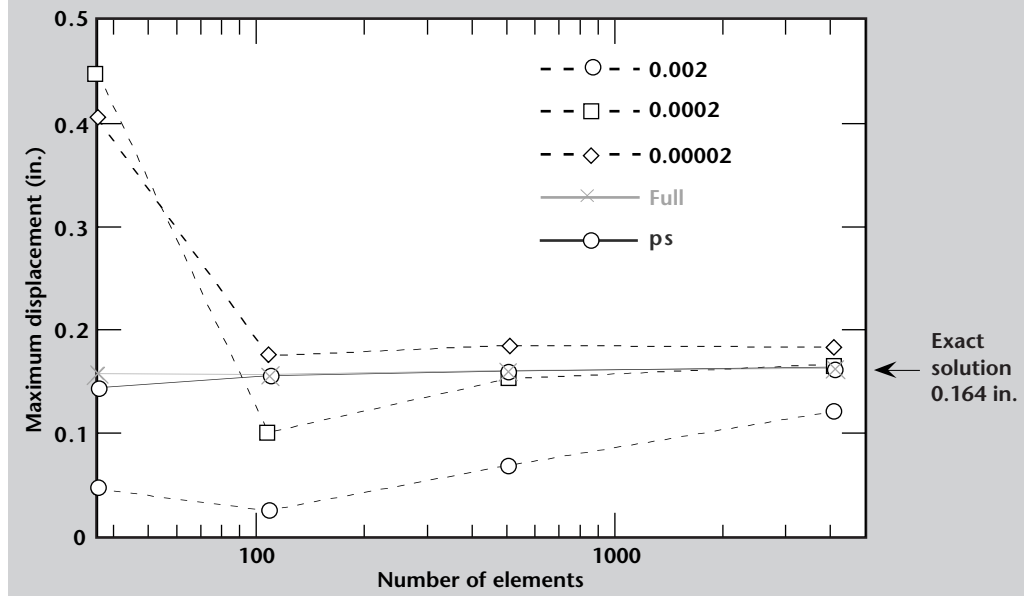
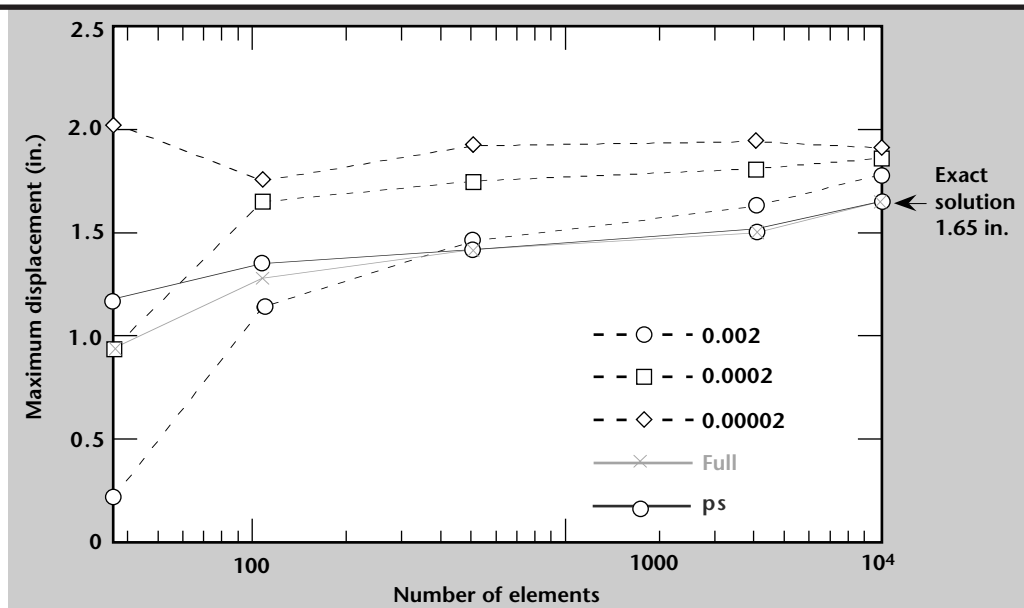


Figure 4. Convergence plot for loading case 2.



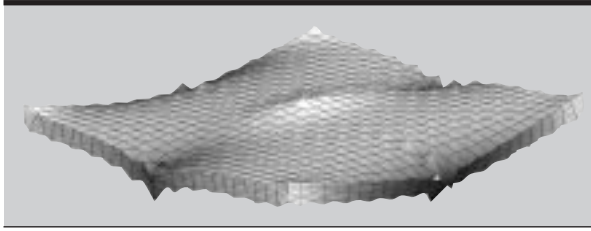


Figure 5. Loading case 2 with $\kappa = 0.00002$.

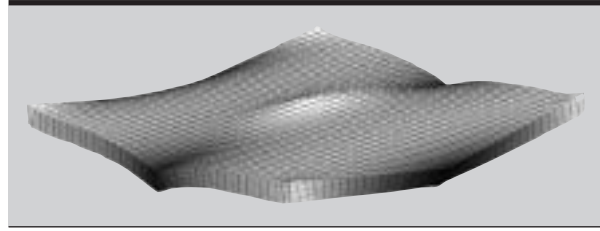



Figure 6. Loading case 2 with physical stabilization.

Future Work

The physically-stabilized element works well, particularly for elasticity. Even with plasticity, the physical stabilization method offers a consistent method, capturing plasticity in the hourglass modes. Nevertheless, with plasticity the element is either all plastic or elastic because of the single-point integration. The fully integrated element, on the other hand, can resolve the plastic front more accurately in coarse meshes. This partial plasticity could potentially be incorporated into the hourglass force calculation by monitoring the hourglass strains and modifying the hourglass stiffness appropriately.

Although the assumed strain field used in the physically-stabilized element works well for many problems, like all assumed-strain methods where some portion of the strain field is projected out, the results can sometimes be diffusive. Higher-order enhanced strain methods could be used in a physical stabilization setting to give better resolution.

References

1. Flanagan, D. T., and T. Belytschko (1981), "A Uniform Strain Hexahedron and Quadrilateral with Orthogonal Hourglass Control," *IJNME*, **17**.
2. Liu, W. K., J. S. Ong, and R. A. Uras (1985) "Finite Element Stabilization Matrices—A Unification Approach," *CMAME*, **53**.
3. Belytschko, T., and L. P. Bindeman (1993), "Assumed Strain Stabilization of the Eight-Node Hexadral Element," *CMAME*, **105**.
4. Crisfield, M. A., and G. F. Moita (1996), "A Co-Rotational Formulation for 2-D Continua Including Incompatible Modes," *IJNME*, **39**.
5. Zhu, Y. Y., and Cescotto, S. (1996), "Unified and Mixed Formulation of the Eight-Node Hexahedral Elements by Assumed Strain Method," *CMAME*, **129**. 



Cyclic Viscoplastic Constitutive Model

Phani Kumar V. V. Nukala

*New Technologies Engineering Division
Mechanical Engineering*

We have implemented a cyclic viscoplastic constitutive model that includes material memory effects into NIKE3D. The constitutive model is based on multi-component forms of kinematic and isotropic hardening variables in conjunction with von Mises yield criteria. In addition, a memory surface (non-hardening surface) is used to capture the strain-range-dependent material memory effects. This work addresses the issues involved in the complete algorithmic treatment of the rate-dependent constitutive model for any desired stress- or strain-constrained configuration subspace. That is, beam, shell, plane stress, plane strain and other stress- and strain-based kinematic constraints can be handled within a single framework. The constitutive model is capable of representing the cyclic hardening and softening behavior, transient and stabilized hysteresis behavior, and the non-fading memory effects of the material.

Introduction

The life prediction of structures and structural components subjected to complex loading histories, which include repeated loading and unloading, requires an accurate representation of the material behavior. Typically, at the very least, this includes an accurate representation of monotonic and cyclic hardening and softening behavior, transient and stabilized hysteresis behavior, and the non-fading memory effects of the material. However, the material models that are currently available in NIKE3D do not have the capability to represent the above-mentioned material behavior.

Furthermore, the implementation of many of these material models into NIKE3D is intrinsically linked to the element technology. That is, the same material model is implemented separately for elements such as bricks, shells, and beams. This inconvenience is quite apparent when the user is forced to use a certain type of element not because of the geometry and loading conditions of the problem, but because of the availability of the required material model to that certain element type.

In this work, a unified cyclic viscoplastic constitutive model along with the multi-component forms of nonlinear kinematic and isotropic hardening rules, is implemented for an accurate prediction of the complex cyclic structural response.¹⁻³

Armstrong-Frederick type rules are used to describe the nonlinear evolution of each of the multi-component kinematic hardening variables. A saturation type (exponential) rule is used to describe the evolution of each of the isotropic hardening variables. The concept of memory surface is used to describe the strain-range-dependent material memory effects that are induced by the prior strain histories.^{1,4}

In addition, the algorithmic treatment of the above constitutive model is such that it allows a single implementation for any desired stress- or strain-constrained subspace. Hence, the cyclic viscoplastic model can be used with any of the elements currently available in NIKE3D.

Progress

A cyclic viscoplastic constitutive model that includes material memory effects has been implemented into NIKE3D. In the following, a brief description of the constitutive model is presented in the standard generalized materials framework.^{1-3,5} For the sake of simplicity of notation in the constrained subspaces (such as plane stress, and beam and shell kinematics), we represent the tensorial variables in terms of their corresponding matrix and vector forms.

In the standard generalized materials framework, the cyclic viscoplastic constitutive equations are expressed as:

- additive decomposition of total strain, ε , into elastic (ε^e) and plastic (ε^p) parts:

$$\varepsilon = \varepsilon^e + \varepsilon^p \quad (1)$$

- state laws based on the form of Helmholtz energy Ψ :

$$\sigma = \frac{\partial \Psi}{\partial \varepsilon^e} = C : \varepsilon^e \quad (2)$$

$$X_i = \frac{\partial \Psi}{\partial \alpha_i} = \frac{2}{3} C_i R : \alpha_i \quad (3)$$

$$R_i = \frac{\partial \Psi}{\partial r_i} = b_i Q_i r_i \quad (4)$$

- evolution laws of internal variables (based on plastic flow potential):

$$\dot{\varepsilon}^p = \dot{\lambda} P \eta \quad (5)$$

$$\dot{\alpha}_i = \dot{\lambda} P \left(\eta - \frac{2}{3} \kappa a_i X_i \right) \quad (6)$$

$$\dot{r}_i = \frac{2}{3} \kappa \dot{\lambda} \left(1 - \frac{R_i}{Q_i} \right) \quad (7)$$

- yield function $f(\sigma, X, R)$:

$$f = \frac{1}{2} \eta^T P \eta - \frac{1}{3} \kappa^2 \leq 0, \quad (8)$$

where

$$\eta = (\sigma - X) \quad (9)$$

$$\kappa = \sigma_0 + R \quad (10)$$

$$X = \sum_i X_i$$

$$R = \sum_i R_i$$

- loading/unloading and consistency conditions (rate-independent plasticity):

$$f \leq 0; \dot{\lambda} \geq 0; \dot{\lambda} f \equiv 0; \dot{\lambda} \dot{f} = 0 \quad (11)$$

- viscoplasticity (Perzyna rule):

$$\dot{\lambda} = \left\langle \frac{f}{K} \right\rangle^n, \quad (12)$$

where C denotes the elastic constitutive matrix in the constrained subspace, α_i denotes the vector form of the tensor variable associated with the kinematic hardening, and r_i denotes a scalar variable associated with the isotropic hardening.

In addition, σ represents the Cauchy stress tensor and X_i and R_i represent the thermodynamic forces associated with α_i and r_i , respectively. The mapping, P , maps the symmetric rank-two stress tensors in the constrained-stress subspace onto symmetric rank-two strain tensors in the deviatoric subspace.

In the following, a non-hardening memory surface is introduced to model the non-fading memory effects of the material.

Let g represent the memory surface, defined as

$$g = \left(\frac{2}{3} \zeta^T R \zeta \right) - q^2 = 0, \quad (13)$$

where the reduced plastic strain, ζ , is defined as $\zeta = \varepsilon^p - \beta$. The evolution of the memory surface is defined through the following relations:

$$\dot{\beta} = \dot{\mu} \zeta \quad (14)$$

$$\dot{q} = \left(\frac{2}{3} \dot{\beta}^T R \dot{\beta} \right)^{\frac{1}{2}} = \dot{\mu} \left(\frac{2}{3} \zeta^T R \zeta \right)^{\frac{1}{2}} = \dot{\mu} \bar{g}. \quad (15)$$

The Kuhn-Tucker optimality conditions along with the consistency requirement can be stated as

$$g \leq 0; \dot{\mu} \geq 0; \dot{\mu} g \equiv 0; \dot{\mu} \dot{g} = 0. \quad (16)$$

The main difference between the rate-dependent and rate-independent cases is in the evaluation of the plastic multiplier, $\dot{\lambda}$. The other conceptual difference is that, in the case of rate-independent plasticity, $f \leq 0$, whereas in the case of viscoplasticity, $f > 0$. However, the numerical treatment for rate-independent and rate-dependent cases is similar.^{5,6}

A generalized midpoint algorithm is used to integrate the rate-constitutive equations. Furthermore, the consistent tangent operator is obtained through an exact linearization of the return mapping algorithm.⁵

Numerical Examples

The return mapping algorithm and the corresponding consistent tangent operator are implemented into NIKE3D.⁷ In the following, several

numerical examples representing the cyclic hardening and softening behavior, transient hysteresis loops, the non-fading memory effects and rate-dependent effects of the material are presented. These examples demonstrate the accuracy and robustness of the present algorithmic framework.

Uniaxial Stress Response for Aluminum Alloy AA6060: Multiple-Step Test. In the following, numerical simulation of a multiple-step test⁸ with eight steps of increasing strain amplitude is performed. This example demonstrates plastic strain-range-dependent hardening (memory) effects

on the cyclic stress response. Ten cycles are performed during each step. The material model consists of two independent kinematic hardening variables and two independent isotropic hardening variables. Memory effects include both plastic strain-range-dependent isotropic and kinematic hardening variables. The material parameters for aluminum alloy AA6060 (temper T4) are given in **Table 1**.

Figures 1a and 1b show the stress response and the hysteresis loops obtained for the multiple-step test during increasing and decreasing strain

Table 1. Material parameters for aluminum alloy AA6060.

$E = 66240 \text{ MPa}$	$\nu = 0.3$	$\sigma = 42 \text{ MPa}$	
$Q_{x1} = 28 \text{ MPa}$	$D_{M1} = 800$	$D_{01} = 4800$	$\delta_1 = 400$
$Q_{x2} = 38 \text{ MPa}$	$D_{M2} = 12$	$D_{02} = 72$	$\delta_2 = 400$
$b_1 = 25$	$Q_{M1} = 75 \text{ MPa}$	$Q_{01} = 22.5 \text{ MPa}$	$\omega_1 = 80$
$b_2 = 0.5$	$Q_{M1} = 65 \text{ MPa}$	$Q_{02} = 19.5 \text{ MPa}$	$\omega_2 = 80$

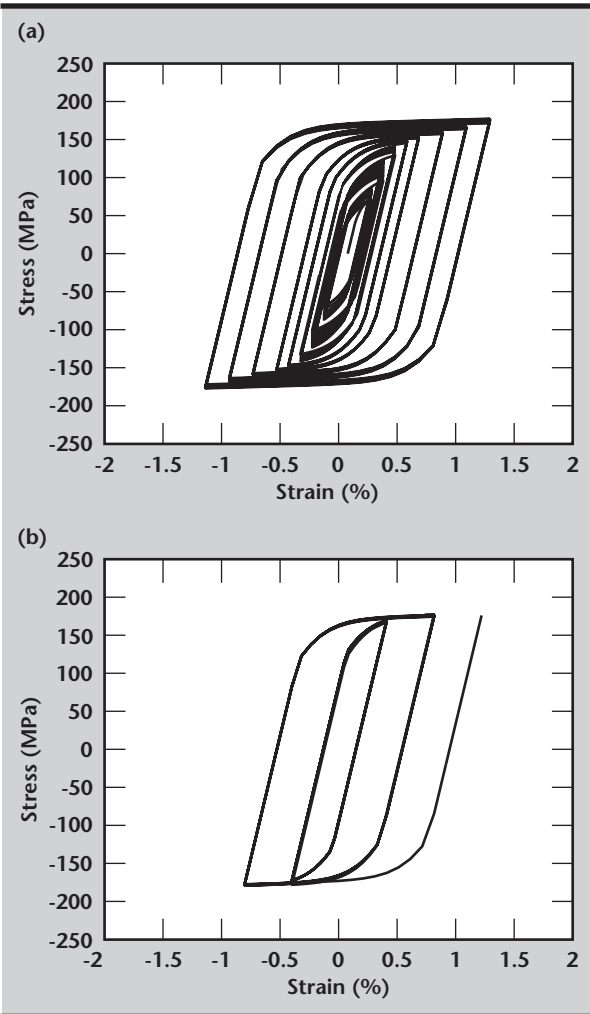


Figure 1. Symmetric multiple step test: (a) increasing strain amplitudes; (b) decreasing strain amplitudes.

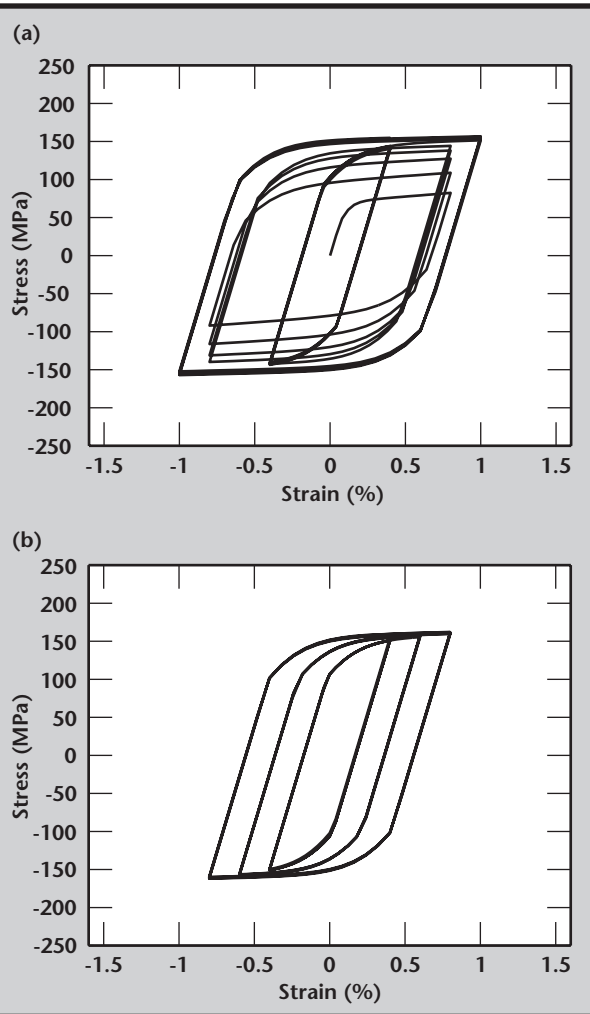


Figure 2. Variable amplitude test: (a) type 1; (b) type 2.

amplitudes, respectively. From the numerical simulation response, it should be noted that cyclic hardening occurs not only during the progressive cycles within a step but also during the increase in step (plastic strain range) size.

Uniaxial Stress Response for Aluminum Alloy AA6060: Variable Amplitude Test. This test⁸ demonstrates the influence of increasing and

decreasing strain amplitudes on the cyclic stress response. The first test is conducted in three steps with strain amplitudes 0.8, 0.4 and 1.0%. In the second test, three steps with strain amplitudes 0.4, 0.6 and 0.8% are used. Five cycles are performed during each step. The material parameters used in the numerical simulation are identical to those used in the multiple-step test. The stress response

Table 2. Material parameters for rate-dependent effects.

E	=	185000 MPa	ν	=	0.3	σ_0	=	82 MPa
K	=	151 MPa	n	=	24			
D_1	=	4200	Q_{x1}	=	38.667 MPa			
D_2	=	37.5	Q_{x2}	=	180 MPa			
b_1	=	8	Q_1	=	60 MPa			

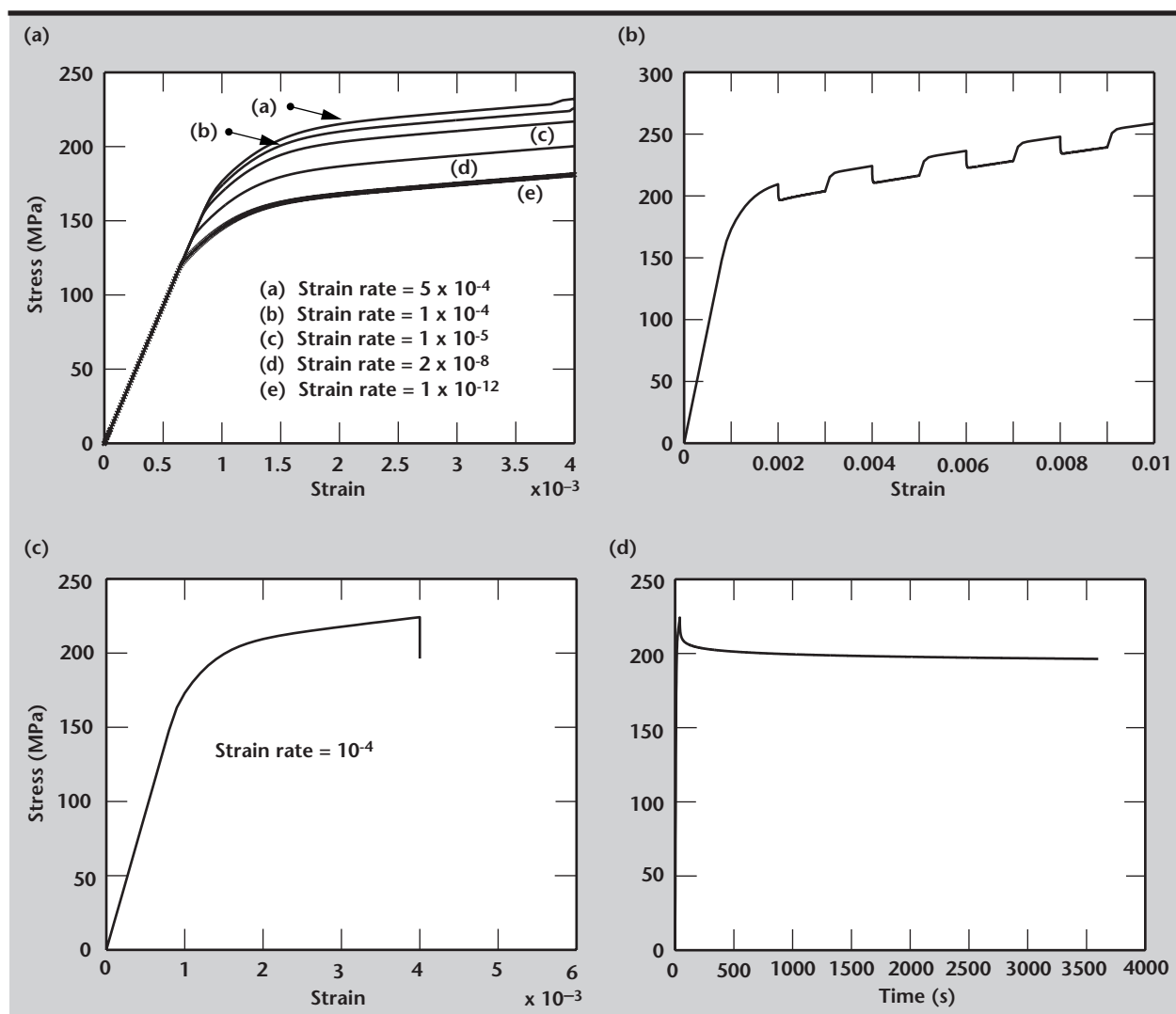


Figure 3. Uniaxial tensile stress-strain behavior: (a) effect of strain rate; (b) effect of strain rate jumps; (c) hardening-relaxation stress-strain curve; (d) hardening-relaxation stress versus time.

obtained for the first and second tests are shown in **Figs. 2a** and **2b**, respectively. For both sequences of variable strain amplitudes, the stress response obtained from the numerical simulations is in good agreement with the physical behavior of the material.


Rate-Dependent Effects. In the following, the effect of strain rate on the stress response is illustrated through three examples. The material model consists of two independent kinematic hardening variables and an isotropic hardening variable to describe the material behavior. A power law is used to describe the rate-dependent effects. The material parameters used for the problems concerning rate-dependent effects are given in **Table 2**.

Figure 3a shows the effect of strain rate on the monotonic tensile behavior of 316L stainless steel. The influence of change in rate of strain during the test on the monotonic stress-strain curve is shown in **Fig. 3b**. From **Fig. 3b**, it can be seen clearly that a change in the rate of strain during the test results in an immediate change in the stress-strain curve, and tends to rejoin the monotonic stress-strain curve corresponding to the new strain rate. **Figures 3c** and **3d** represent the numerical simulation of hardening-relaxation behavior of the material.

Future Work

Modeling of ratcheting effect, static recovery effects, and the effect of temperature on the material behavior is the scope of the future work. Formulation and a complete algorithmic treatment of the above cyclic viscoplastic constitutive model in the finite strain hyper-elastic-plastic constitutive framework are also planned.

References

1. Lemaitre, J., and J. L. Chaboche (1990), *Mechanics of Solid Materials*, Cambridge University Press, Cambridge, UK.
2. Chaboche, J. L. (1989), "Constitutive equations for cyclic plasticity and cyclic viscoplasticity," *International Journal of Plasticity*, **5**, pp. 247–302.
3. Ohno, N. (1990), "Recent topics in constitutive modeling of cyclic plasticity and viscoplasticity," *Applied Mechanics Review*, **43**, p. 283.
4. Ohno, N. (1982), "A constitutive model of cyclic plasticity with a non-hardening strain region," *Journal of Applied Mechanics*, **49**, p. 721.
5. Nukala, P. K. V. V., "A Cyclic Viscoplastic Constitutive Model," submitted to *Computer Methods in Applied Mechanics and Engineering*.
6. Simo, J. C., and S. Govindjee (1991), "Non-linear B-stability and symmetry preserving return mapping algorithms for plasticity and viscoplasticity," *International Journal of Numerical Methods in Engineering*, **31**, pp. 151–176.
7. Maker, B. N. (1995), "NIKE3D: A nonlinear implicit three-dimensional finite element code for solid and structural mechanics," Lawrence Livermore National Laboratory, Livermore, California (UCRL-MA-105268, Rev. 1).
8. Langseth, M., O. S. Hopperstad, and S. Remseth (1995), "Cyclic stress-strain behavior of alloy AA6060, Part I: Uniaxial experiments and modeling," *International Journal of Plasticity*, **11**, pp. 725–739. 

Electromagnetic Cold-Test Characterization of the Quad-Driven Stripline Kicker

Scott D. Nelson and James E. Dunlap

*Defense Sciences Engineering Division
Electronics Engineering*

The first kicker concept design for beam deflection was constructed to allow stripline plates to be driven—thus directing, or kicking, the electron beam into two subsequent beamlines. This quad-driven stripline kicker is an eight-port electromagnetic network consisting of two actively driven plates and two terminated plates. Electromagnetic measurements performed on the bi-kicker and quad-kicker were designed to determine: 1) the quality of the fabrication of the kicker, including component alignments; 2) quantification of the input feed transition regions from the input coax to the driven kicker plates; 3) identification of properties of the kicker itself without involving the effects of the electron beam; 4) coupling between a line current source and the plates of the kicker; and 5) effects on the driven current to simulate an electron beam through the body of the kicker. Included are the angular variations inside the kicker to examine modal distributions. The goal of the simulated beam was to allow curved path and changing radius studies to be performed electromagnetically. The cold-test results were then incorporated into beam models.

Introduction

The original kicker design¹⁻³ was conceived to allow for the diversion of the electron beam dynamically during a long pulse, thus acting like a beam-splitter (**Figs. 1 and 2**). Experiments performed on the kicker⁴ detail the operating parameters of the system. This report outlines the electromagnetic cold-test measurements

performed on the kicker as part of the analysis, and concepts for the kicker pulser requirements.

Due to beamline use and the motivations for the cold-test measurements, the kicker was tested in the Lawrence Livermore National Laboratory (LLNL) Electromagnetics Laboratory using a variety of vector network analyzers to sweep the frequency band, and time-domain impulse generators and scopes.

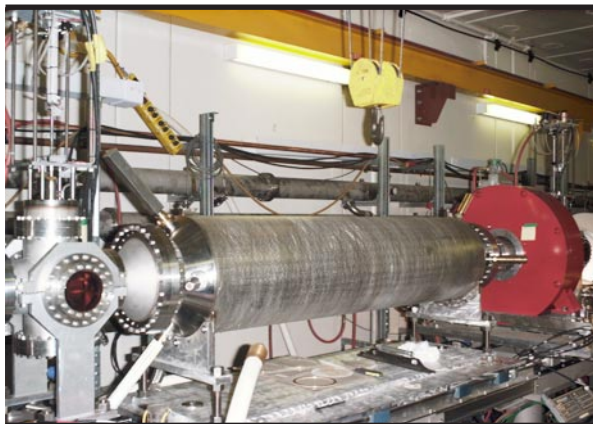


Figure 1. The quad-kicker in the Experimental Test Accelerator beamline as part of the verification experiments. Note the four ports on each end, which connect directly to the deflection plates. Two of the white pulser cables are visible in the foreground.



Figure 2. The quad-kicker, tested using frequency- and time-domain scopes to cover the band for the swept frequency tests and instantaneous impulse tests.

Progress

Kicker Port Testing

Each of the eight input ports of the kicker was tested over a frequency band from 45 to 500 MHz. Two ports connected to the input and output of each of the four plates through a tapered transition region, through a coaxial connector (Fig. 3). The pin on the plate connected directly to the center pin of the coax. The results of the measurements, shown in Fig. 4, indicate a broadband match, with the exception of resonances caused by the feed regions. The comparison in Fig. 5 illustrates the feed region effects based on experience from the bi-kicker and quad-kicker development activities. Figure 6 shows the complex input impedance of the kicker for one of the ports.

Cross-Coupling Terms

The cross-plate coupling terms of the kicker corresponded to the coupling between adjacent and opposite ends of the various plates to each other. These terms represent energy that couples from the kicker pulser-driven plate to those plates that are terminated, thus inducing fields onto plates that are not directly driven. These cross-coupling terms are appreciable (8% and 20%) even at the lower frequencies. Figure 7 shows the magnitude of the coupling between adjacent plates vs frequency. Figure 8 is a photograph of the quad-kicker plates.



Figure 3. Photograph showing four striplines of the kicker, each forming impedance-matched transmission lines. The center pin that connects to the coaxial cable is visible at the end of each plate. The configuration at the other end is identical.

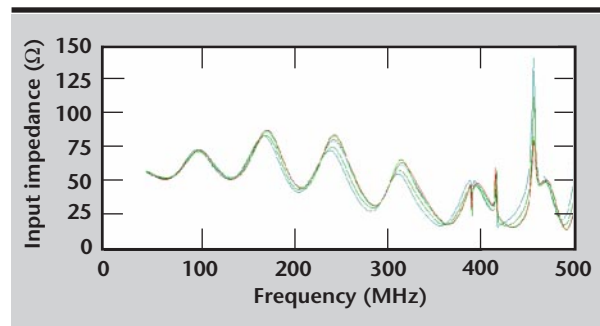
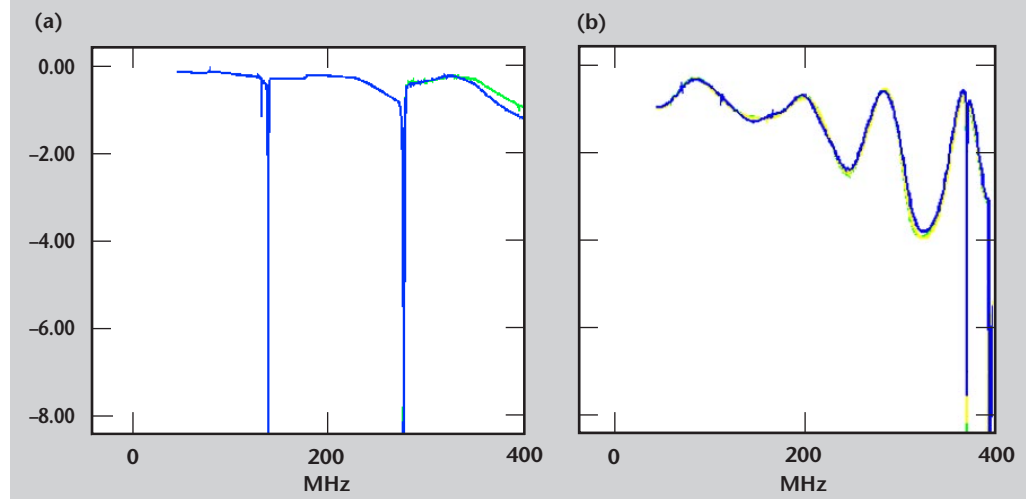


Figure 4. Input impedance of each of the ports shown vs frequency (margin of error $\pm 0.3 \Omega$). The spikes at 388.75, 414.0, and 460 MHz are higher-order mode resonances and correspond to Q_s of 310 (quadrupole mode), 61 (dipole mode), and 29 (dipole mode), respectively.

Figure 5. Kicker port testing. The input reflection coefficient vs frequency of the bi-kicker (a) was much more uniform due to the more gradual transition region after the coaxial feeds. The quad-kicker (b) had a more abrupt transition after the coax and has a larger input reflection coefficient. The spikes in the bi-kicker response curve are due to the grounded plate resonances and were eliminated in the quad-kicker.



Forward-Coupling Terms

The kicker pulsers drive one end of the plates and the other end is mated to reduce reflections on the plate structure. The loss along the plates is less than 1 dB. The transfer function from one end of the plate to the other is shown in **Fig. 9**.

Kicker Response

For identification of the transient properties of the kicker and the association between a simulated beam and the kicker ports, a ramp pulse

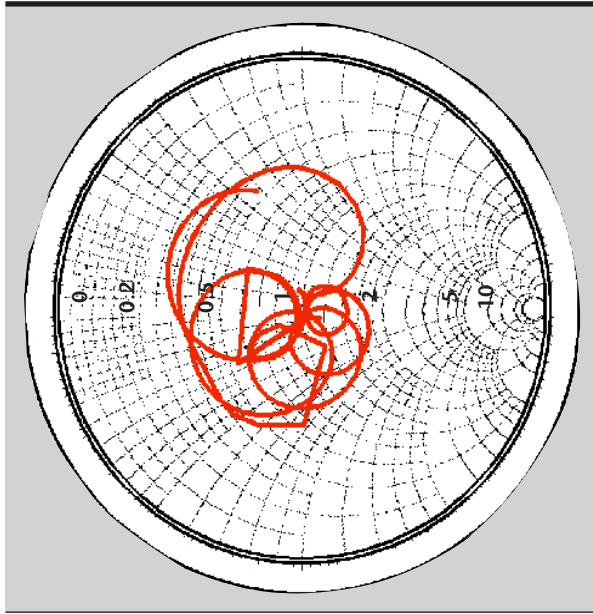


Figure 6. Complex input impedance of the kicker for one of the ports (the variance between the ports is $\pm 7 \Omega$ due to fabrication differences). The three straight lines in the curve represent under-sampling.

(0.95 V/300 ns) was used to excite the wire current. The resulting waveform that was induced on the downstream output port is shown in **Fig. 10**.

When the central wire representing an electron beam was excited through the main body of the kicker, the “pump-up” time of the kicker was observed as an equivalent time constant of 70 ns. This corresponds to the cavity fill time between the simulated beam pulse and the ports.

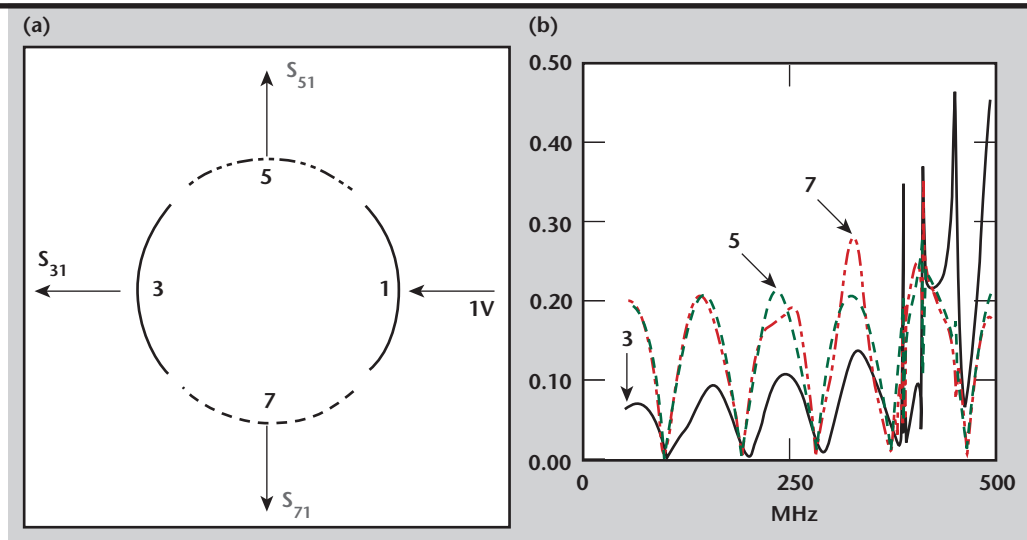
Azimuthal Variations

During the course of the measurements, the azimuthal variation caused by the offset-rotations of the current wire was measured and compared against the theoretical solution for an offset wire in an ideal kicker. A comparison between the theoretical solution (dashed line) for an electrostatic coupling case and that for the experimental cases at the peak coupling points of 68.4, 139.2, and 209.4 MHz is shown in **Fig. 11**. The angular frequency spectrum of the plots was taken to determine the relationships between the various modes (dipole, quadrupole, and sextupole) in the kicker. The modal ratios are shown in **Table 1**.

The ratios are in a range similar to that determined by integrating the simple analytic representation⁵ along the plate boundaries shown in **Eq. 1**.

$$\frac{V_s}{V_D} = \frac{4q \frac{a^3}{b^4} \int_{-\phi}^{\phi} \cos 3\theta d\theta}{4q \frac{a}{b^2} \int_{-\phi}^{\phi} \cos \theta d\theta} = \frac{1}{3} \frac{a^2}{b^2} \frac{\sin 3\phi}{\sin \phi};$$

Figure 7. Magnitude of coupling between adjacent plates vs frequency, showing significant cross-coupling at multiples of 80 MHz. The adjacent plate coupling is 20%; the cross plate coupling is 8%.



$$\frac{V_Q}{V_D} = \frac{1}{2} \frac{a \sin 2\phi}{b \sin \phi} \quad (1)$$

where ϕ is the plate half-angle (39°), but 45° was used, to be consistent with the theory, since **Eq. 1** assumes no gaps, b is the plate radius (12.87 cm), and a is the radius to the wire position (3.175 cm). Differences can be attributed to gap effects between

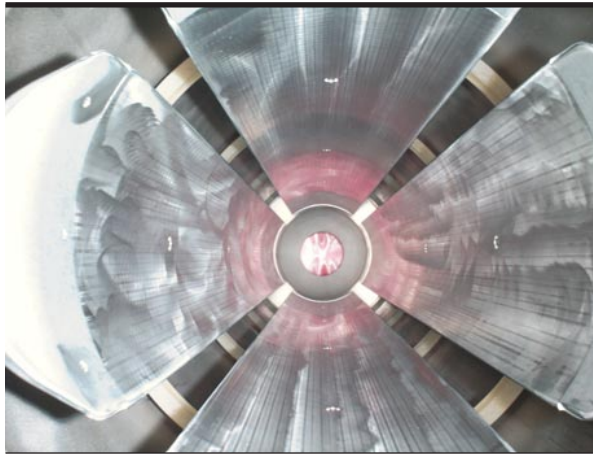


Figure 8. Identical quad-kicker plates connected to a $50\text{-}\Omega$ coaxial port. For experiments using the existing kicker pulsers, two of the plates were driven and two were terminated in matched loads. Each plate is 78° wide (12.87 cm radius) and is supported by rexolite.

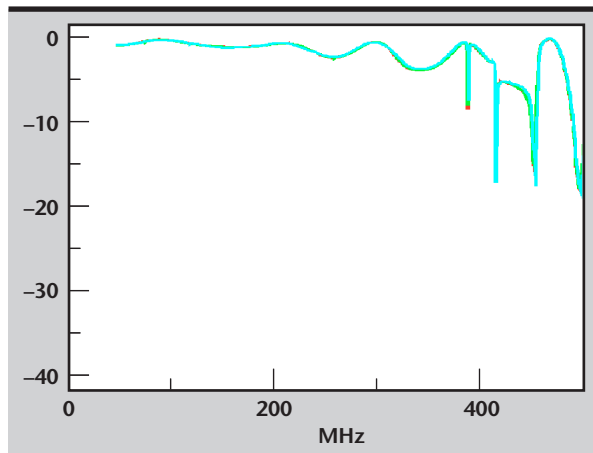


Figure 9. Transfer function vs frequency from one end of the plates to the other. In the low frequency part of the spectrum, the curves for the various plates overlap to within 0.025 dB.

plates, end effects near the feeds, and simplifications of the analytic representation.

Conclusions

Although the frequency range of interest for kicker applications is in the low hundreds of megahertz and is based on the bandwidth of the kicker pulser, there were initial concerns about

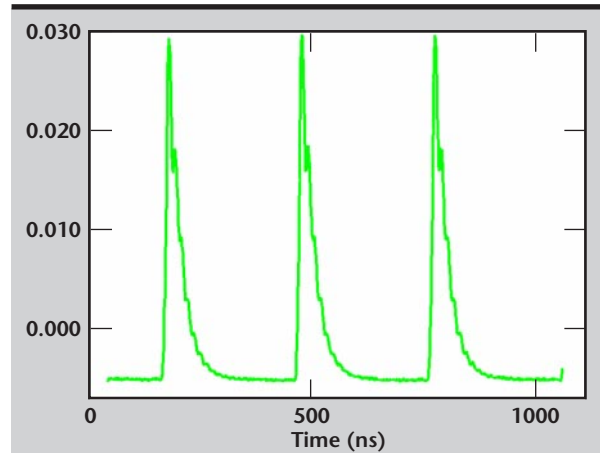


Figure 10. Effect of the 300-ns ramp pulse coupling from the wire current to one of the kicker plates monitored at a downstream port. Notice that after about 70 ns, the coupling stabilizes to -0.005 V (-0.53%). The spikes occur at the transition of each 300-ns excitation ramp waveform.

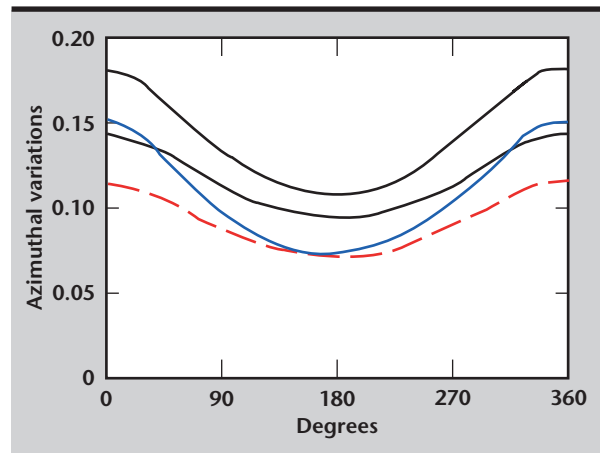


Figure 11. Comparison between theoretical coupling curve (dashed) based on electrostatic modeling of an ideal kicker structure and experimental data.

Table 1. Angular frequency spectrum.

	Static	68.4	139.2	209.4	Eq. 1
V_Q/V_D	0.136	0.134	0.140	0.169	0.174
V_S/V_D	0.0252	0.0315	0.0327	0.0351	0.0203


beam-induced effects. For this frequency range: the cross-coupling between adjacent ports is <14 dB; the input impedance for each port is between 50 and 90 Ω ; transmission along the plates experiences less than 1 dB of loss; cavity measurements show a cavity pump-up time, and a dI/dt coupling between the current wire and the cavity.

The input reflection coefficient for some higher frequencies can approach 30%; but these frequencies are expected to be outside of the normal operating range of the kicker. However, in making the modifications from the bi-kicker design to the quad-kicker design, the frequency band where these effects make a pronounced difference was lowered and is closer to the operating band. Thus, subsequent changes in the kicker design would need to be made with this limit in mind. It should be emphasized however that the elimination of the shorted plates from the bi-kicker design substantially improved the operation of the quad-kicker.⁴

Acknowledgments

Thanks to B. Poole for numerous conversations about kicker development and to J. Chen and J. Weir for their experimental activities.

References

1. Caporaso, G. J., Y. J. Chen, and B. R. Poole (1997), "Transmission Line Analysis of Beam Deflection in a BPM Stripline Kicker," *1997 Particle Accelerator Conference*, Vancouver, B.C., Canada, May, Lawrence Livermore National Laboratory, Livermore, California (UCRL-JC-126073).
2. Nelson, S. D. (1998), "Electromagnetic (Cold Test) Characterization of the Bi-Driven Kicker," Lawrence Livermore National Laboratory, Livermore, California (UCRL-ID-129997), January, <http://www-dsed.llnl.gov/documents/em/sdnkick98/>.
3. Poole, B. R., G. J. Caporaso, and Y. J. Chen (1998), "Analysis and Modeling of a Stripline Beam Kicker and Septum," *1998 Linear Induction Accelerator Conference*, Chicago, Illinois, August 24-28.
4. Chen, Y. J., G. J. Caporaso, and J. Weir (1998), "Experimental Results of the Active Deflection of a Beam from a Kicker System," *1998 Linear Induction Accelerator Conference*, Chicago, Illinois, August 24-28.
5. Chao, A. W. (1993), "Physics of Collective Beam Instabilities in High Energy Physics," John Wiley and Sons, New York, New York, p. 6. 



Photonic Doppler Velocimetry

Paul D. Sargis, Nicole E. Molau, and Daren Sweider

Defense Sciences Engineering Division

Electronics Engineering

We are developing a novel fiber-optic approach to laser Doppler velocimetry as a diagnostic for high-explosives tests. Using hardware that was originally developed for the telecommunications industry, we are able to measure surface velocities ranging from centimeters per second to kilometers per second. Laboratory measurements and field trials have shown excellent agreement with other diagnostics.

Introduction

Laser Doppler velocimetry is a powerful diagnostic for the high-explosives physics community. The frequency of the Doppler-shifted light provides a direct measure of the instantaneous velocity of a rapidly moving target illuminated by a laser. Light from a multi-mode optical fiber illuminates the target and another multi-mode fiber collects the Doppler-shifted light, allowing spatially-resolved velocimetry information to be obtained.

Currently, physicists perform surface velocity measurements using a technique called Fabry-Perot Velocimetry. This system uses free-space Fabry-Perot interferometers and streak cameras for each data channel. These components are costly, complex, require maintenance and operator set-up, require a custom-built optical table and occupy a considerable volume. The Fabry-Perot system also uses a large YAG laser whose output is doubled to 532 nm because the streak camera photocathode is insensitive in the infrared region of the spectrum. Although the Fabry-Perot velocimeter yields excellent data, overall channel count will always remain low due to its size, cost, and complexity. As new NTS high-explosives facilities become available to experimenters, it will be highly desirable to have many velocimetry data channels available without the cost, complexity, and manpower-intensive set-up required for the current diagnostic system.

Our technique uses multi-mode fiber optics, an optical PIN detector, RF electronics, and moderate sample-rate A/D converter technology. All of the components fit into a small chassis. The advantage

of using multi-mode fiber is the significant increase in optical light collection from the target, compared to that from a single-mode fiber. This advance in laser Doppler velocimetry will enable the fielding of significantly more data channels, greatly improving the spatial-temporal information obtained from this diagnostic at reduced cost, complexity, and experimental footprint.

A simplified version of this diagnostic will permit nanosecond-resolution shock arrival-time measurements by detecting the first incidence of Doppler-shifted light. Such a diagnostic will be very useful on high-fidelity flight tests in the weapons program at Lawrence Livermore National Laboratory (LLNL). Future versions of this diagnostic could be made sufficiently compact and rugged to be practical for the flight test application.

Figure 1 illustrates the basics of the photonic Doppler velocimetry system. A laser-generated optical carrier propagates through a multi-mode fiber to a probe lens. The probe illuminates the target with the optical carrier. As the target moves towards the lens, the reflected light is Doppler-shifted. The probe lens collects a portion of the Doppler-shifted light, and the light propagates back through the multi-mode fiber. The Doppler-shifted light is mixed with a fraction of the original optical carrier in a fiber-optic coupler and is detected by a "square-law" optical detector. Under the appropriate polarization and modal conditions, the square-law detector generates an electrical current proportional to the square of the optical fields. For the Doppler-shifted light, this corresponds to a beat frequency proportional to the instantaneous velocity of the target.

At high velocities, the beat frequency is too high to record directly on a transient digitizer. To overcome this limitation, we use a microwave phase discriminator to measure the frequency-dependent phase shift induced by the Doppler signal. Recording of the phase discriminator data is accomplished using a digitizer having a modest sampling rate.

Progress

In the past year, our efforts have focused on laboratory experiments and field trials.

The target for our first refereed test was a shock-driven copper foil, with the Fabry-Perot velocimeter

acting as the referee. As illustrated in **Fig. 2**, the copper foil was in close proximity to a bridge wire, which was driven by a capacitive discharge unit (CDU). Green light from a frequency-doubled YAG laser was focused onto the copper target through a probe lens. The Doppler-shifted light was reflected back through the probe lens and was simultaneously processed by both the Fabry-Perot velocimeter and the photonic Doppler velocimeter.

The raw transient digitizer data from the photonic Doppler system is plotted in **Fig. 3a**, and the raw streak camera data from the Fabry-Perot system is shown in **Fig. 3b**. The Doppler beat frequency signal in **Fig. 3a** was converted into frequency versus time,

Figure 1. Basic block diagram of the photonic Doppler velocimetry system.

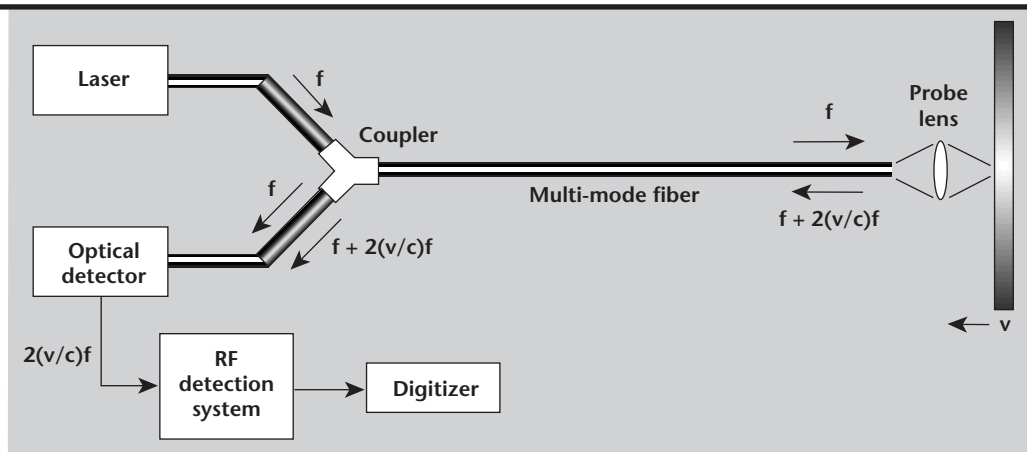


Figure 2. Block diagram of the copper foil velocity experiment.

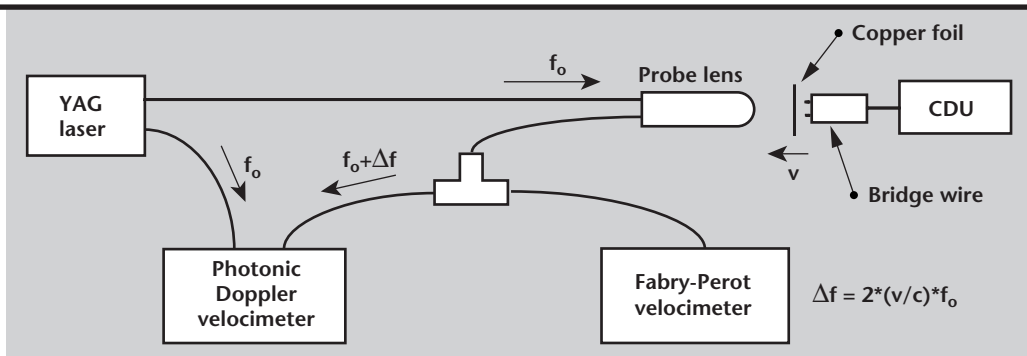
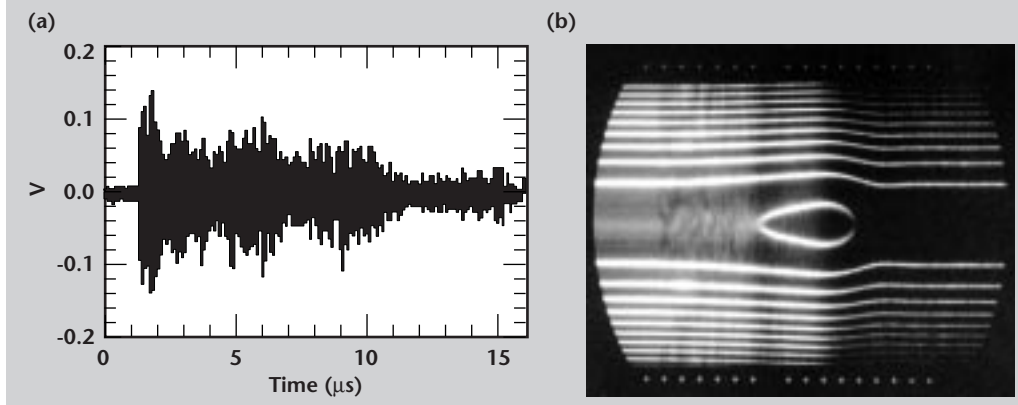


Figure 3. Raw data from the copper foil experiment: a) photonic Doppler velocimeter; b) Fabry-Perot velocimeter.



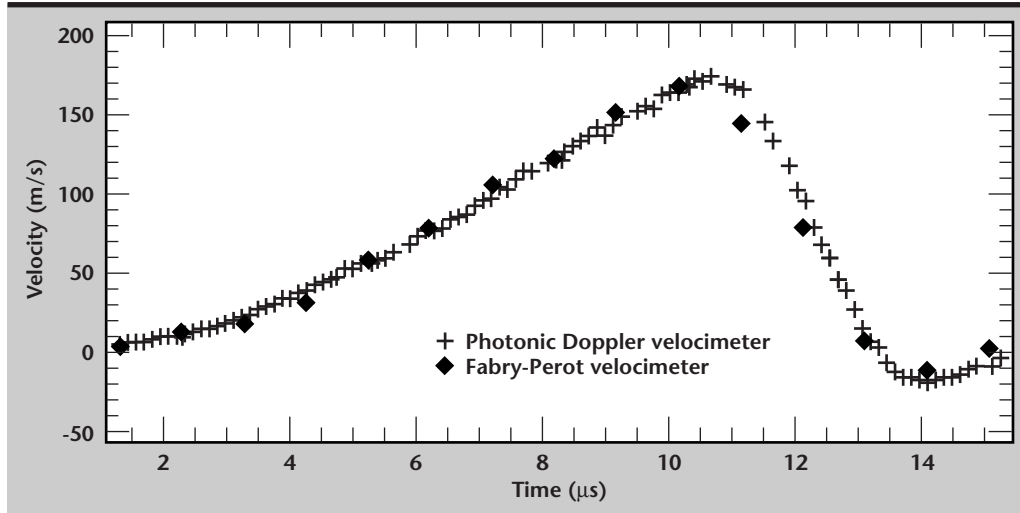


Figure 4. Processed data from the copper foil experiment.

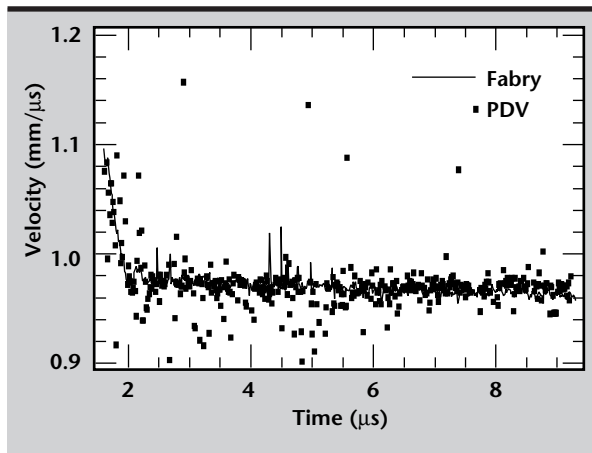


Figure 5. Processed data from the Site 300 aluminum plate experiment.


and then into velocity versus time, as shown in **Fig. 4**. Velocity values were hand-digitized from the Fabry-Perot data and then plotted on the same graph in **Fig. 4**. The negative velocity at the end of the data record is consistent with the rebounding of the copper foil after the shock event.

In a later experiment conducted at LLNL's Site 300, the copper foil target was replaced with an aluminum plate that was driven by high explosives. The remainder of the experimental set-up was the same as that illustrated in **Fig. 2**. This time, however, the Doppler beat frequency was too high to be recorded directly on a transient digitizer. We used

a microwave phase discriminator to measure the frequency-dependent phase shift of the incoming signal. The processed result is plotted with the Fabry-Perot result in **Fig. 5**.

We also conducted a series of measurements in the laboratory using a continuously moving target, which consisted of a speaker driven by an audio oscillator. This set-up provided the framework for evaluating system stability and reliability. We discovered that the signal-to-noise ratio varies with time and is adversely affected by physically moving the multi-mode fiber. The likely causes of this phenomenon include: instability of the optical state on the polarization optical detector, mode selective loss, and de-phasing of the optical signals caused by the surface reflection and optical fiber propagation.

Future Work

We plan to conduct further research into system stability and reliability issues, including making detailed measurements of the changes induced in the optical polarization state, the mode populations, and their relative phases by the moving surface and the optical elements in the system. Once we have gained a better understanding of these issues, we will design and build an optimized system. Finally, we will demonstrate the optimized system on an Asay foil experiment. 



Modeling Coupled Heat and Mass Diffusion

Arthur B. Shapiro

*New Technologies Engineering Division
Mechanical Engineering*

Philip M. Gresho

*Atmospheric Science Division
Environmental Programs*

We have developed a model that includes thermally-driven mass diffusion to predict the evaporation rate of bound water in a porous material in a vacuum. All water in the porous material is in the “sorptive” or “bound” state and the main mechanisms of moisture transfer are bound water and vapor diffusion. This differs from the state in which free water exists in the pores and moisture transfer is by capillary flow.

Introduction

Drying is the removal of water from a solid by evaporation. In the evaporation process, heat has to be supplied to the material, so that simultaneous transfer of heat and mass occurs. Several drying periods are defined:

1. First Drying Period (constant rate drying). The surface of the solid is covered with a continuous layer of free water, and evaporation takes place mainly at the surface. The rate of drying depends entirely on parameters external to the solid, such as the air velocity, temperature, and humidity. If the external conditions are constant, then the drying rate is constant. The temperature of the solid will equilibrate to the wet bulb temperature of the air.
2. First Falling Rate Period. As drying proceeds, the fraction of wet area decreases with decreasing surface moisture content. The surface will form discontinuous wet patches and the mass transfer from the surface will decrease with a slowly rising surface temperature. Free water still exists at the surface, the “dry” patches still contain bound water, and the vapor pressure at the surface is determined by the Clausius-Clapeyron equation.

3. Second Falling Rate Period. No free water exists at the surface. The surface temperature will rise rapidly, during which a receding evaporation front appears, dividing the solid into a wet region and the sorption (bound water) region. Inside the evaporation front, the material is wet (that is, the voids contain free water), and the main mechanism of moisture transfer is capillary flow. Outside the front, all water is in the sorptive or bound state and the main mechanisms of moisture transfer are bound water and vapor diffusion. Evaporation takes place at the front as well as in the whole sorption region, while vapor flows through the sorption region to the surface.

In our application all the water is in the “sorptive” or “bound” state, and the main mechanisms of moisture transfer are bound water and vapor diffusion.

Progress

The most appropriate and applicable model for mass transfer that seems to describe well the relevant physics over the entire range of pressure—from atmospheric pressure where continuum dynamics prevails, on down to hard vacuum conditions at

which free-molecule flow prevails—is a model that was first envisaged by James Clerk Maxwell about 140 years ago, during the early development of the kinetic theory of gases. It was later rediscovered several times by others. Called (in recent times) the dusty gas model¹ (DGM), it treats the porous medium (the “dust”) as a collection of fixed spheres around which “n” ideal gases flow. The DGM is most succinctly described for isothermal conditions as follows:

$$\frac{N_i}{D_i^e} + \sum_{j \neq i}^n \frac{X_j N_i - X_i N_j}{D_{ij}^e} = -\frac{1}{RT} \nabla(x_i P) - \frac{x_i D_v}{RT D_i^e} \nabla P \quad (1)$$

where N_i is the molar flux ($c_i u_i$) of component i (g-moles/cm² s), x_j is the mole fraction of component j , P is pressure (dyne/cm²), T is temperature (K), R is the gas constant ($\sim 8.3 \times 10^7$ gm cm²/g-mole s² K), and the diffusivities are as follows:

1. $D_i^e = K_o v_i$ is the effective Knudsen (free-molecule) diffusivity, K_o is an effective diffusion length ($K_o = 2a/3$ for a tube of radius a), in cm, and

$$v_i \equiv \sqrt{8RT / \pi M_i} \quad (2)$$

is the mean molecular speed (M_i is the molecular weight);

2. $D_{ij}^e = K_1 D_{ij}$ is the effective ordinary (bulk) binary diffusivity associated with continuum (Stefan-Maxwell) diffusion, where K_1 is a dimensionless constant ($K_1 \leq 1$) and D_{ij} is the (known) binary molecular diffusivity;
3. $D_v = B_o P / \mu$ is the viscous/Darcy diffusivity, where μ is the gas viscosity (gm/cm s) and B_o is the effective “area” of the medium (cm²; $B_o = a^2/8$ for a tube of radius a —Poiseuille flow).

For a porous medium, the DGM is a three-parameter model, in which the three parameters that “characterize” the porous medium (K_o , K_1 , B_o) are best determined experimentally. Note that the DGM successfully combines three physical phenomena in one model: 1) free-molecule flow (Knudsen flow/diffusion) that prevails at very low pressure (where $D_{ij} \rightarrow \infty$ and $D_v \rightarrow 0$); 2) ordinary (Stefan-Maxwell) diffusion that is important at higher pressures ($D_i^e / D_{ij}^e \rightarrow \infty$); and 3) viscous flow, which carries all species at the same rate (non-separative) and is most simply “described” by the first term in the left-hand side and the last term in the right-hand

side of **Eq. 1**, via $N_i^v \equiv -x_i D_v \nabla P / RT$, which basically describes Poiseuille flow.

In addition to the transport of water in the porous media defined by **Eq. 1**, an expression is needed for the evaporation rate of liquid water to gas in a vacuum.² Kinetic theory applies to systems in vacuum. Equilibrium requires that the rate of evaporation equals the rate of condensation. Therefore, we can determine the evaporation rate by equating it to the mass of molecules striking the surface.

From kinetic theory, the number of molecules of a gas that strike a surface is

$$\nu = \frac{1}{4} n v_a \quad (\text{molecules/cm}^2 \text{ s}),$$

where the average gas velocity is given by **Eq. 2**, and the number of molecules per volume is determined by the ideal gas law

$$n = \frac{N_A P_{mm}}{RT} \quad (\text{molecules/cm}^3),$$

where N_A is Avogadro’s number (6.0228×10^{23} molecules/gmole), R is the universal gas constant (6.236×10^4 cm³ mm/g gmole K), P_{mm} is the water vapor pressure in mm of Hg, and T is the temperature in K.

The mass of gas striking (or leaving) a surface per unit area per unit time is then

$$G = m\nu = m \left(\frac{1}{4} n v_i \right) = \frac{M}{N_A} \left[\frac{1}{4} \left(\frac{N_A P_{mm}}{RT} \right) \left(\frac{8RT}{\pi M} \right)^{1/2} \right] = \left(\frac{P_{mm}^2 M}{2\pi RT} \right)^{1/2}.$$

Using the molecular weight of water as $M = 18.02$ g/gmole, the expression for the mass of water vapor leaving a surface, G , can then be evaluated to be

$$G = 0.247 \frac{P_{mm}}{T^{1/2}} \quad (\text{g/cm}^2 \text{ s}).$$

Over a small temperature range, the vapor pressure of water may be represented by the Clausius-Clapeyron equation

$$P_{mm} = \exp \left(A - \frac{B}{T} \right),$$

where A and B are constants determined from experimental data such as shown in **Table 1**.

Using the end points in **Table 1**, A and B are determined to be $A = 17.765$ and $B = 5314.8$. Then, the final expression to calculate the evaporation rate is

Table 1. Pressure of aqueous vapor over water.³

T (K)	P (in. of Hg)
288.6	0.5218
294.1	0.7392
299.7	1.0321

$$G = 6.27 \frac{\exp\left(17.765 - \frac{5314.8}{T}\right)}{T^{1/2}} (\text{g/cm}^2 \text{ s}). \quad (3)$$

Equation 3 applies to a completely wet liquid surface. This expression must be multiplied by the fraction of surface area that is wet to give the evaporation rate for a partially wetted surface.

Future Work

Experiments are planned that will determine the three parameters of the DGM for one or more particular cases of current interest. Also, the restriction to isothermal flow will be removed. This is most easily introduced at the low pressure end (vacuum

conditions, where it is most important) by adding the following term to the right-hand side of **Eq. 1**:

$$+ \frac{x_i P}{2RT^2} \nabla T,$$

which accounts for thermal transpiration (bulk flow owing to temperature gradients) and, interestingly, is perhaps somewhat counter-intuitive in that thermally-induced flow is *up* the temperature gradient.

Our ultimate goal is to include these developments in the TOPAZ heat transfer code to extend the code's capability into the arena of low-speed flow and heat transfer of ideal gaseous mixtures in porous media, especially at low pressure.

References

1. Mason, E., and A. Malinauskas (1983), *Gas Transport in Porous Media: The Dusty Gas Model*, Elsevier, Amsterdam.
2. Dushman, S. (1966), *Of Scientific Foundations of Vacuum Techniques*, 4th ed., John Wiley and Sons, New York, New York.
3. Hougen, O. (1959), *Chemical Process Principles*, 2nd ed., John Wiley and Sons, New York, New York, p. 82.

Analysis and Modeling of a Stripline Beam Kicker and Septum

Brian R. Poole, Lisa Wang, and Yu Ju (Judy) Chen

*Defense Sciences Engineering Division
Electronics Engineering*

George J. Caporaso

Laser Programs

A fast stripline beam kicker and septum are used to dynamically switch a high-current electron beam between two beamlines. The transport of the beam through these structures is determined by the quality of the applied electromagnetic fields as well as temporal effects due to the wakefields produced by the beam. In addition, nonlinear forces in the structure will lead to emittance growth. The effect of these issues is investigated analytically and by using particle transport codes. Due to the distributed nature of the beam-induced effects, multiple macro-particles (slices) are used in the particle transport code, where each slice consists of an ensemble of particles with an initial distribution in phase space. Changes in the multipole moments of an individual slice establish electromagnetic wakes in the structure, and are allowed to interact with subsequent beam macro-particles to determine the variation of the steering, focusing, and emittance growth during the beam pulse.

Introduction

The stripline kicker is designed to spatially separate a high-current electron beam for transport into two separate beamlines. However, to provide a significant angular kick to the beam, a magnetic dipole septum is required. This system is shown schematically in **Fig. 1**.

The operation of the system is as follows: a high-voltage pulse is applied to the downstream ports of the kicker, and the beam is spatially separated (kicked) by a combination of the transverse electric and magnetic dipole forces associated with the transverse electromagnetic (TEM) waves propagating on the strip transmission lines.

The beam is then directed into a septum magnet with opposite polarity dipole fields on either side of the plane separating the two downstream beamlines. All the upstream ports and the two downstream ports in the non-kick plane are terminated in a matched load impedance for the dipole transmission mode on the structure. It should be noted that steering in both planes can be accomplished by also driving the other pair of plates.

Kicker TEM Fields and Beam Deflection

To steer the beam in x , opposite polarity high-voltage pulses are applied to the downstream ports in the $y = 0$ plane. The potential within the kicker plates ($r < b$) is given by

$$V = \frac{4V_p}{\pi} \times \sum_{m=\text{odd}} \left(\frac{1}{m} \right) \sin \left(\frac{m\phi_0}{2} \right) \cos(m\phi) \left(\frac{r}{b} \right)^m, \quad (1)$$

where b is the interior radius of the kicker plates, and ϕ_0 is the angle subtended by the kicker plates.

The voltage applied to the plate is V_p , giving a total steering voltage of $2V_p$. The solution is determined by solving for the potential in the region $r < b$, and using the boundary conditions that 1) the potential at $r = b$ is given by the appropriate applied plate voltages, and 2) the potential in the gaps between the plates is zero. The TEM fields can be easily derived from this scalar potential.

The $m = 1$ term in Eq. 1 represents a transverse dipole force which provides the beam steering, while the higher order terms will contribute to emittance growth in the beam. The beam deflection due to the combined electric and magnetic dipole forces is given by

$$\Delta x = \frac{\pi b V_p}{I_c Z_k \sin(\phi_0/2)}, \quad (2)$$

where the critical current, I_c , is defined by

$$I_c = \frac{\pi}{16} \frac{\gamma \beta^2 I_0}{\sin^2\left(\frac{\phi_0}{2}\right)} \frac{Z_0 \left(\frac{b}{L}\right)^2}{Z_k}, \quad (3)$$

and $I_0 = 17$ kA, $Z_0 = 377 \Omega$, L is the length of the kicker, b is the inner radius of the kicker plates, Z_k is the kicker impedance, and γ is the usual relativistic factor.

Progress

Dipole Wake Impedance and Beam-Induced Steering

In our application, the beam current is sufficiently large to induce substantial voltages and currents on the strip transmission lines. These voltages and currents are introduced on the transmission lines as the beam traverses the upstream and downstream gaps, and from changes in the dipole return current as the beam is deflected. A detailed model has been described previously.^{1,2}

The $m = 1$ transverse dipole wake impedance for this structure³ is given by

$$Z_{\perp}(\omega) = \frac{8cZ_k}{\pi^2 b^2} \sin^2\left(\frac{\phi_0}{2}\right) \left(\frac{1}{\omega}\right) \times \left[\sin^2\left(\frac{\omega L}{c}\right) + j \sin\left(\frac{\omega L}{c}\right) \cos\left(\frac{\omega L}{c}\right) \right]. \quad (4)$$

The imaginary part of the dipole impedance, $Z_{\perp 0} = \text{Im}[Z_{\perp}(\omega = 0)]$, is a measure of the asymptotic beam deflection due to the beam-induced fields. It has been shown that the asymptotic beam deflection for an initially offset beam with current I_B injected into the kicker has the form¹

$$x_{\infty} = x_0 \cosh\left(\sqrt{\frac{2I_B}{I_c}}\right), \quad (5)$$

where x_0 is the injection offset of the beam. It is easily shown for sufficiently small beam currents that

$$x_{\infty} \approx x_0 \left[1 + \left(\frac{2\pi L}{\gamma \beta^2 I_0 Z_0} \right) I_B Z_{\perp 0} \right]. \quad (6)$$

To examine the relevant physics issues, a kicker has been designed and installed on Lawrence Livermore National Laboratory's Experimental Test Accelerator (ETA-II). The ETA-II kicker has the following set of parameters: $b = 12.87$ cm, $\phi_0 = 78^\circ$, $Z_k = 50 \Omega$, $L = 164$ cm, and $I_c = 3.9$ kA. The outer enclosure has a radius of 19 cm. To verify the validity of the transmission line model, the structure was modeled using LLNL's TIGER 3-D time-domain electromagnetic code to determine the dipole impedance spectrum.

Figure 2 shows a comparison of the dipole impedance as calculated from Eq. 4 with numerical results from the TIGER code for the ETA-II kicker. As can be seen, there is good agreement between the transmission line model and the 3-D code results. The differences can be attributed to end cavity effects associated with the feeds to the external ports and effects due to higher order modes in the structure.

The effect of the wake impedance on the deflection of the beam can be quite dramatic. For example, for a 6-MeV, 2-kA beam initially offset by 2 cm going into the kicker, the tail of the emerging beam will be offset by 3.1 cm at the exit of the structure. These effects have been observed experimentally⁴ and are consistent with theory.

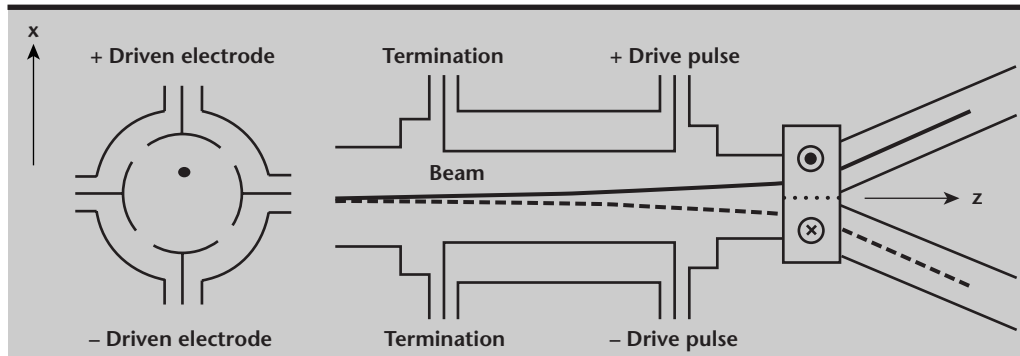


Figure 1. Kicker and septum configuration for dynamic beam-steering in one plane.

Nonlinear Forces and Emittance Growth

From **Eq. 1** it is seen that for a dipole excitation of the kicker, all higher order odd multipoles will be excited in the structure. Although the higher order multipoles reduce in strength as $(r/b)^m$, it is possible under certain conditions that the beam will experience these fields, especially the $m = 3$ sextupole component.

For example, with ETA-II parameters the space-charge fields due to the beam may require that the beam entering the kicker have a large radius to enable the downstream beam to be at or near a waist when entering the dipole septum. This is important to minimize any emittance growth due to the nonlinear fields associated with the septum magnet.

To estimate the effect of the higher order multipoles due to the kicker on the beam emittance, a simple particle transport code was developed. The code includes the external fields in the kicker region as defined by **Eq. 1**, and is being expanded to include the beam-induced effects and space-charge effects self-consistently.

Presently, the particles respond only to the external fields. However, we can estimate the emittance growth in the structure by using the external fields only. As an example, using the ETA-II kicker previously described, a 6-MeV beam is injected into the kicker with an unnormalized edge emittance of 13 cm-mrad and a convergence angle of 0.03 rad. The injected beam radius is 4 cm, which allows the beam to experience the higher order multipoles. **Figure 3** shows a configuration-space image of the emerging beam from the kicker showing a centroid location of 2.7 cm, consistent with **Eq. 2**. The triangular image has been observed experimentally.⁴

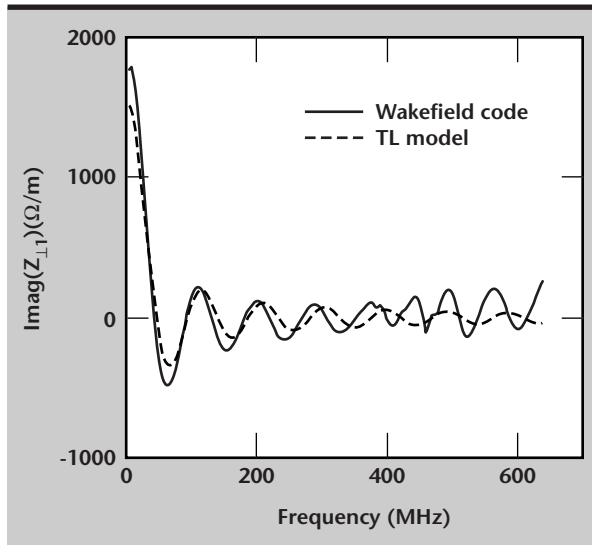


Figure 2. Dipole wake impedance.

Despite the strong deformation of the beam image, the emittance growth is predicted to be about 53% for this beam. However, transport calculations have also shown that it is possible to transport a smaller radius high-current beam, ~2 kA, through the kicker giving an estimated emittance growth on the order of 2%.

Magnetic Dipole Septum

The septum magnet provides an additional angular kick to the beam as it emerges from the kicker. The kick is in opposite directions on either side of $x = 0$. The septum is shown schematically in **Fig. 4**.

The dipole magnetic field required to produce a beam exit angle of $\sim 15^\circ$ is determined from

$$B\ell = \frac{mc}{e} \sqrt{\left(\frac{E_b}{mc^2}\right)^2 + 2\left(\frac{E_b}{mc^2}\right)} \times [\sin(\theta_i + \Delta\theta) - \sin(\theta_i)], \quad (7)$$

where ℓ is the axial length of the magnet, θ_i is the incident beam angle, $\theta_i + \Delta\theta$ is the desired exit beam angle, and E_b is the beam energy.

A preliminary design for a dipole septum magnet to be used with the ETA-II kicker is being developed. The parameters for the design are an axial length of 20 cm, and a magnetic field of about 276 G for a beam energy of 6.3 MeV. The dimensions of the aperture are about $h=6$ cm high and $w=31$ cm wide. Careful optimization of the design is required to minimize possible emittance growth in the transition region where the field changes sign.

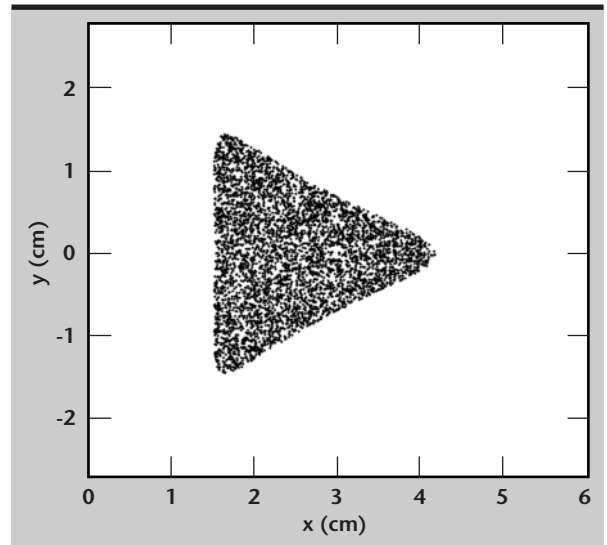


Figure 3. Configuration-space image of beam emerging from kicker experiencing a large sextupole field.

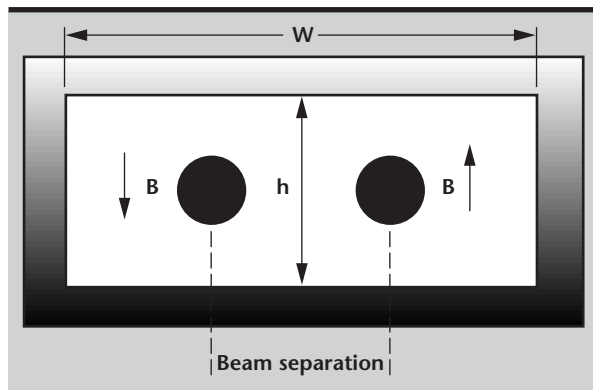


Figure 4. Magnetic dipole septum magnet.

Magnetic modules are being developed for particle transport codes to estimate the emittance growth through the septum magnet. With careful design, including shims, preliminary estimates show an emittance growth on the order of 4% through the septum magnet.

Conclusions

Self-consistent models are being developed for modeling the transport of high-current, space-charge-dominated beams through fast beam kickers and dipole septum magnets. The effect of beam-induced forces due to the wakefields of the beam are included in the analysis.

In addition, emittance growth due to nonlinear forces associated with higher order multipoles in both the kicker and septum have been estimated. Preliminary estimates of beam-induced steering are consistent with the experimental program.⁴ The effect of space charge, image forces, and fringe fields in the structures have yet to be included.

Acknowledgments

Discussions on the electromagnetic characterization of the kicker with S. Nelson are greatly appreciated. Thanks also go to D. Steich for running the 3-D electromagnetic simulations of the kicker.

References

1. Caporaso, G. J., Y. J. Chen, and B. R. Poole (1997), "Transmission Line Analysis of Beam Deflection in a BPM Stripline Kicker," *1997 Particle Accelerator Conference*, Vancouver, B.C., Canada, May 12–16, Lawrence Livermore National Laboratory, California (UCRL-JC-126073).
2. Poole, B. R., G. J. Caporaso, and W. C. Ng (1997), "Wake Properties of a Stripline Beam Kicker," *1997 Particle Accelerator Conference*, Vancouver, B.C., Canada, May 12–16, Lawrence Livermore National Laboratory, California (UCRL-JC-126075).
3. Ng, K.-Y. (1988), "Impedances of Stripline Beam-Position Monitors," *Particle Accelerators* **23**, pp. 93–102.
4. Chen, Y. J., G. J. Caporaso, and J. Weir (1998), "Experimental Results on the Active Deflection of a Beam from a Kicker System," *XIX International Linac Conference (Linac98)*, Chicago, Illinois, August 23–28. 